Microfluidic Analysis in Patient Biopsies: toward Precision Medicine for Glioblastoma Multiforme

Thesis by

Jungwoo Kim

In Partial Fulfillment of the Requirements

for the Degree of

Doctor of Philosophy

Caltech

CALIFORNIA INSTITUTE OF TECHNOLOGY

Pasadena, California

2018

(Defended August 14, 2017)

To my family,

Wangseok Kim, Kyeongok Kim,

Kwangho Oh, Aeryun Kim,

and

Jihyun Oh

"See a lot; do what you believe is right."

Bill Clinton

in South Korea, 2005

Acknowledgements

Above all, I would like to thank my advisor, Professor Jim Heath, for his great support and all the wonderful research opportunities. His ideas and passion guided me to reach where I had never imagined before. My experience in Jim's lab will be the solid ground on which I build my future as a scientist. I would like to thank my thesis committee, Professor David Tirrell, Professor Tom Miller, and Professor Mikhail Shapiro, for their input in my scientific training. I thank my amazing collaborators at UCLA, Dr. Tim Cloughesy, Dr. Ben Ellingson, Dr. Robert Harris, Professor David Nathanson, Wilson Mai, Lisa Ta, Professor Arion F. Chatziioannou, and Dr. Alex Dooraghi. I also appreciate Professor Rustem Ismagilov, Dr. Liang Ma, Dr. Songzi Kou, and Dr. Mikhail Karymov for my early research experiences at Caltech.

I thank all the Heath lab family members for being good friends and having fun scientific training, work, and discussions. I have learned a lot from you and also enjoyed working together—Dr. Young Shik Shin (a great mentor), Dr. Kiwook Hwang, Dazy Johnson, Dr. David Bunck, Dr. Alphonsus Ng, Dr. Alex Xu (3 rift masters in D3), JingXin Liang (#1 photographer), Dr. Songming Peng (a Jurkat cell and drone expert), Yapeng Su (you know-), Amy McCarthy, Professor Arundhati Nag, Dr. Samir Das, Dr. Fan Liu, Alice Hsu, Dr. Sharareh Gholamin, William Chour, Dr. Katrine Museth, Kevin Kan, Nicole LaBerge, Professor Min Xue, Professor Wei Wei, Professor Jun Wang, Prof. Nataly Kravchenko-Balasha, Dr. Alexander Sutherland, Dr. Ryan Henning, Dr. Joseph Varghese, and all other members. Let's keep in touch and meet somewhere around the world!

Abstract

Although every individual has a unique biology, most medicine still relies on the one-size-fits-all approach, which often fails in the treatment of heterogeneous diseases like cancer. An emerging approach to disease treatment is precision medicine, in which a specific treatment is tailored for individual patients using their biological information, including their genome, phenome, and proteome. Two clinical actions are important for implementing precision medicine in cancer therapies: choosing the correct drugs via patient stratification and choosing a suitable drug dosage and duration via drug response monitoring.

After selecting the potential drug candidate, it is crucial to monitor tumor response to drug therapy because cancer is a dynamic disease that can develop drug resistance. Although non-invasive tumor imaging techniques such as magnetic resonance imaging, computed tomography, and positron emission tomography can assess physical size and metabolic activity of tumors, these techniques have poor time resolution and cannot capture the dynamic changes of bio-molecules implicated with drug resistance. Thus, to effectively monitor drug response, supplemental diagnostic or prognostic markers must be routinely measured from patient biopsies. Unfortunately, routine monitoring of multiple biomarkers from patient biopsies is impractical, as conventional analytical assays require large sample amounts (up to 100-1000 mg of tissue or 10 mL of blood).

In response to this challenge, this thesis describes the development of various microfluidic technologies that can perform multiplexed measurements (up to 20-plex) using minute amounts of sample (10^4-10^5 cells or 30µL of blood) in a miniaturized

analytical platform (maximum 75 × 26 × 1 mm footprint). We applied these technologies for drug screening and drug response monitoring in glioblastoma multiforme, a highly lethal brain tumor, assaying two different types of patient biopsies: cancer cells and blood.

First, we developed an integrated microfluidics-chip/beta particle imaging system that can screen for effective therapies using small amounts of patient-derived cell lines. Since glioblastoma cells have abnormally high glycolytic activity, this was used as a read-out for drug response. Single cells were isolated in micro-traps, and their glycolytic activity was quantitated using a radioactive probe. This platform can assess potential drug targets directly from patient biopsies without administering drugs to the patient.

Second, we developed an *in vitro* diagnostic test that can monitor tumor drug resistance by measuring up to 14 proteins in finger-prick volumes of blood. This test relies on microfluidics and microarray patterning of antibodies to carry out multiplexed sandwich-type immunofluorescence assays. Using this technology and conventional tumor imaging techniques, we linked proteomic signatures to tumor growth, establishing diagnostic and prognostic models in two clinical treatment cases of bevacizumab and buparlisib. Moreover, we adopted the multiplexed proteomic measurement platform to rapidly screen out small peptide binding agents that target an oncogenic protein in glioblastoma.

The microfluidic tools developed here are sample-efficient and highly informative, and we propose that these techniques could enable routine evaluation of drug response in a precision medicine workflow.

Published content and contribution

<u>Publications / manuscripts in the order of thesis chapters (* equal contribution)</u>

1. Shin, Y. S.*; <u>**Kim, J.***</u>; Johnson, D.; Dooraghi, A. A.; Mai, W. X.; Ta, L.; Chatziioannou, A. F.; Phelps, M. E.; Nathanson, D. A.; Heath, J. R. *Technology* **2015**, *3* (4), 172.

> - DOI: 10.1142/S2339547815200058

> - J.K. developed microfluidic devices, designed and performed tests.

2. <u>**Kim, J.**</u>; Johnson, D.; Shin, Y. S.; Vermesh, U.; Vermesh, O.; Harris, R.; Sutherland, A. M.; To, S.; Ellingson, B.; Cloughesy, T.; Heath, J. R. *in preparation*

> - Manuscript titled, "Serum proteomic measurement for monitoring glioblastoma patient responses to an anti-angiogenic drug treatment."

> - J.K. conceived the ideas, developed microfluidic technologies, and performed patient sample measurement & data analysis.

3. Wen, P. Y.; <u>**Kim, J.**</u>; Wei, W.; Johnson, D.; Heath, J. R. et al. *in preparation*

> - Manuscript titled, "Phase II study of BKM120 (Buparlisib) for subjects with recurrent glioblastoma"

> - J.K. conceived the ideas, developed microfluidic technologies, and performed patient sample measurement & data analysis.

4. McCarthy, A. M.*; <u>**Kim, J. ***</u>; Museth, A. K.; Hening, R. K.; Heath, J. E.; Winson, E.; Oh, J. J.; Heath, J. R. *submitted*

- Manuscript titled, "An allosteric inhibitor of KRas identified using a barcoded rapid assay microchip platform."

- J.K. conceived the ideas, developed microfluidic technologies, and performed measurement & data analysis.

Table of contents

List of figures and tables

Chapter 5

Abbreviations and acronyms

Akt (protein kinase B)

ATP (adenosine triphosphate)

BRAF (v-Raf murine sarcoma viral oncogene homolog B)

BRCA1/2 (breast cancer 1/2, early onset)

DEAL (DNA-encoded antibody library)

DNA (deoxyribonucleic acid)

EGFR (epidermal growth factor receptor)

FDA (United States Food and Drug Administration)

GBM (glioblastoma multiforme)

IDH1 (isocitrate dehydrogenase 1)

KRAS (Kirsten rat sarcoma protein)

MFI (mean fluorescence intensity)

mTOR (mechanistic target of rapamycin)

OBOC (one bead one compound)

PCC (protein catalyzed capture agent)

PI3K (phosphoinositide 3-kinase)

PI3KCA (phosphoinositide-3-kinase, catalytic, alpha polypeptide)

PTEN (phosphatase and tensin homolog)

RAS (rat sarcoma protein)

RNA (ribonucleic acid)

RTK (receptor tyrosine kinase)

VEGF (vascular endothelial growth factor)

Chapter 1

Introduction

1.1 The concept of precision medicine

Physicians have traditionally relied on average results from clinical trials to determine therapeutic strategies, and they often find patients who do not respond or benefit from the treatment.[1] The non-responders are subsequently prescribed the next candidate treatment *ad nauseam,* until no options remain. Such trial-and-error medicine is not only a financial burden on the healthcare system, but also presents a health risk for patients who experience adverse side effects and/or patients with time-sensitive diseases such as cancer. We are now entering the era of precision medicine, also known as personalized medicine,[1] in which physicians cater a treatment regimen to a patient's response and genetic predisposition, giving 'the right drug for the right patient at the right dose and time.'[2] In this new clinical paradigm, physicians design therapeutic strategies based on patients' unique drug targets, diverse genetic backgrounds, and environmental factors—such individual variability often determines the efficacy of medical treatments.[1–5] The increasing importance of precision medicine has promoted the Obama administration to launch the Precision Medicine Initiative in 2015 with the budget of $55 million, aiming "to enable a new era of medicine through research, technology, and policies that empower patients, researchers, and

providers to work together toward development of individualized care." This government-led research effort focuses on constructing treatment pipelines for cancer in the short-term and expanding these strategies to encompass other diseases in the future.[6]

1.2 Analyzing patient biopsies for precision medicine in targeted cancer therapy

A patient's biological information is critical for the implementation of precision medicine, especially in targeted cancer therapy. Targeted cancer therapy is the use of drugs such as small molecular weight chemical compound or biologics (e.g. antibody or recombinant proteins) to modulate molecular targets (e.g. proteins, peptides, or nuclei acids), altering specific functional activities associated with tumor proliferation.[4,5] To design effective targeted therapy, clinicians can extract two types biological information from tumor biopsies: (1) a patient's genotype and phenotype, which is useful for identifying drug targets, and (2) a patient's characteristic drug response, which is important for determining effective drug dosage and timing. These two types of biological information are further described below in the context of precision medicine.

First, a patient's genotype and phenotype can be quantitatively measured from tumor biopsies so that clinicians can stratify patients into subpopulations and determine their inter-patient variabilities from large cohorts. The relevant genotype of a patient, such as the presence of oncogenes and genetic mutations, can be determined by DNA sequencing technologies such as Next Generation Sequencing, which is significantly decreasing in cost and improving in efficiency.[5] Some examples of important cancer genes include EGFR or

IDH1 mutation in glioblastoma,[7,8] BRAF mutation in melanoma,[9] KRAS mutation in pancreatic and colorectal cancer,[10] and BRCA1/2 mutation in breast and ovarian cancer.[11,12] The phenotype of a patient are the traits linked to functional molecular profiles in the downstream of genes,[3,13] which includes gene expressions, protein abundance, and metabolic activities. For instance, cancer cells typically have altered profiles of tumor suppressor/oncogenic gene expressions, signaling transduction pathways, and/or glycolysis/glutaminolysis activities.[14,15] The information collected from the genotype and phenotype enable clinicians to identify potential drug targets for precision medicine.

Second, a patient's response to drug intervention can broadly alter the tumor phenotype, ranging from proliferation rate to signaling circuitry. Recently, several studies demonstrated *in vitro* assays for drug response, using it to guide precision medicine in a research setting.[16–18] In one assay, cancer cells from tumor biopsy were simultaneously cultured in a petri-dish and a xenograft mouse. The *in vitro* cell cultures were used to rapidly screen drugs determined by the genotype of the cells. Subsequently, the mouse models were used to validate potential drug candidates, measuring changes in tumor size and other phenotypes. Based on these results, potential combination therapies can be further tested using the same workflow.[18] In the clinical settings, tumor proliferation are assessed by well-established, non-invasive imaging techniques such as magnetic resonance imaging (MRI), computed tomography (CT), and positron emission tomography (PET). Physicians can monitor drug responses by measuring physical sizes or metabolic activities of the tumor.[19] However, due to logistical challenges of sampling tumor biopsies, it is difficult to conduct detailed longitudinal studies of the tumor phenotype. Without knowing the molecular drug response of the tumor, clinicians are hard-pressed to prevent the

development of drug resistance in targeted therapy. A potential solution is the use of blood plasma, which can be collected regularly from patients. Accordingly, many researchers have been investigating the use of plasma biomarkers to track the drug response of tumors.[20]

As mentioned above, the most straightforward way to extract a patient's biological information is studying the patient's biopsies such as cancer cells and blood plasma. However, due the large sample requirement of current analytical techniques, it is difficult to run multiple assays in parallel, limiting the amount of information that can be extracted. These challenges can potentially be resolved through the use of microfluidic tools, which enable rapid, high-throughput analysis of biological samples in small volumes. Moreover, this liquid-handling technology can be easily adapted to any sample type and is compatibility with conventional analytical methods such as microscopy, mass spectrometry, immunoassays, and polymer chain reaction (PCR), with improved limit of detection in quantitating DNAs, RNAs, and proteins. In the current state-of-the-art, these tools can isolate rare living cells from patient biopsies, characterize them for mechanical and biological phenotypes, and manipulate them for culture and drug response studies.[20–23] Therefore, microfluidics holds great promise for deep analysis of patient biopsies to guide precision medicine in the clinic. Harvested cancer cells can be profiled for genes, transcripts, proteins, and metabolites at the single-cell level. Circulating DNAs, RNAs, proteins, and tumor cells in plasma can be isolated and studied for their diagnostic and prognostic capacities in the context of cancer.

1.3 Single cell cancer metabolic measurement for studying the drug responses of cancer cells

Intratumoral heterogeneity is an emerging hallmark of cancer and is a critical challenge for targeted cancer therapies.[24–26] Individual cells within a tumor can have highly heterogeneous genotypes and phenotypes, which decreases the effectiveness of targeted therapies in cancer patients.[27,28] Intratumoral heterogeneity originates from two major characteristics: 1) mutational polyclonality, and 2) diverse cell signaling and metabolic networks (despite identical genetic backgrounds). Recently, these features of heterogeneity have been investigated using single-cell analysis tools,[29] which enable genomic, transcriptomic, proteomic, and metabolic studies that characterize cellular heterogeneity in a tumor.[30–35] For example, in a recent single cell transcriptomic study, researchers discovered that a subpopulation of drug-resistant cells exist in various abundances among patient-derived melanoma cell lines.[36]

Abnormal metabolic activity is another widely accepted hallmark of cancer.[14] Beyond the function of generating energy, the tumor metabolome is closely related to the genotypes and molecular phenotypes of the cancer cells. For example, an established cancer-related metabolic abnormality, known as the Warburg effect, is characterized by an accelerated rate of aerobic glycolytic activity in cancer cells (i.e. increase consumption of glucose), and it is associated with oncogenic activation and loss of tumor suppressors. Other metabolic signatures, such as upregulated consumption of glutamine, have been recently implicated in tumor proliferation. The increased consumption and metabolism of glucose and glutamine enables cancer cells to produce the cellular intermediates and building

blocks required for proliferation.[14,15,37] Thus, cancer can be viewed as a metabolic disease caused by the summation of gene mutations, dysfunctional genetic regulation and expression, and the consequent aberrant protein signaling and metabolism. Furthermore, the metabolic profiles of cancer can be used to monitor drug response to targeted therapy treatment. For example, PET and magnetic resonance spectroscopy (MRS) are often used in the clinic to non-invasively measure the average metabolic activities of tumors, which can help determine the therapeutic efficacy of a drug.[38,39]

Measuring the metabolic activities of tumors at the single-cell level can enable the study of cellular heterogeneity and abnormal metabolism (both hallmarks of cancer) and may provide deep insights for drug responses as well as identifying potential drug targets. Although the average metabolic activities of treated tumors can be used to assess drug efficacy, it is equally important to analyze metabolism at the single-cell level, finding cells that are potentially drug resistant with outlying metabolic activities. The genotypes and phenotypes of these outliers should investigated to understand the molecular basis of their differential metabolism and other associated features, including proliferation and protein signaling. By targeting the specific features of these outliers, clinicians can potentially suppress the development of drug resistance in cancer. Thus, single-cell metabolic analysis may become an important new approach to assess the overall drug response of a tumor.

Currently, there are two class of approaches that can measure single-cell metabolic activities: 1) destructive methods, such as mass spectrometry and cytometry (MS and CyTOF), and 2) non-destructive methods, such as PET. In the first approach, cellular components are typically digested, ionized, and detected by their molecular weight and unique fragmentation signature. Matrix-assisted laser desorption/ionization (MALDI) and

electrospray ionization (ESI) are major ionization methods, and the time-of-flight (TOF) is a widely used mass analyzer. Liquid chromatography (LC) is often included in the front end of mass spectrometry (LC-MS), so that molecules can be first separated based on their physicochemical properties. Metabolic activities in various samples have been analyzed, ranging from dissociated/cultured cell suspensions to tissue slices. As demonstrated in CyTOF, target molecules can be chemically modified or labeled with metal-tagged antibodies for increased quantitation capacity. Recently, the sensitivity of MS has been improved to obtain comprehensive single cell metabolome profiles.[40,41] In the second approach, metabolite analogs are introduced in the cell via cellular uptake. These metabolite analogs are structurally similar to target natural metabolites, but contain chemical moieties that produce photons for detection and quantitation by PET. Examples of glucose analogs include ^{18}F-flurorodeoxyglucose (^{18}F-FDG) and 2-(N-(7-nitrobenz-2-oxa-1,3-diazol-4-yl)amino)-2-deoxyglucose (2-NBDG). In the case of ^{18}F-FDG, beta-decay of ^{18}F produces a positron, which, upon meeting an electron, will annihilate and produce two gamma ray photons. While this approach largely relies on the availability of the analog molecules, this method is not disruptive, and thus has more flexibility in integrating with other molecular analysis techniques such as DNA sequencing and immunofluorescence protein assays for further characterization of single cells.[35,42–44]

1.4 Plasma proteomics for monitoring the drug responses of patient tumors

Blood plasma is the reservoir of biological signals secreted from the entire body, and these signals are often employed for monitoring patient therapeutic responses. Plasma is straightforward to collect from patients, and contains quantifiable biological information that presumably reflects biological responses to perturbations. Thus, it can potentially be used for the molecular characterization of drug response in cancer patients, especially when combined with a non-invasive imaging technique to assess tumor growth. There is an increasing number of reports that demonstrate the importance of plasma DNA, RNA, proteins, and circulating tumor cells in tumor progression. Among these potential markers, proteins are the read-out which can be readily interpreted as biological functions in the cell.[45–48] This feature is particularly useful for targeted therapy since it is straightforward to determine a potential drug target for a given protein biomarker. However, to date, there are only two accepted single-protein markers that can be used for monitoring drug response in tumors: cancer antigen (CA125) for ovarian cancer and prostate-specific antigen (PSA) for prostate cancer. To overcome the limited diagnostic power of single-protein markers, proteomic classifiers of cancers, composed of multi-protein panels, have been developed with improved cancer diagnostic capacity.[49]

Mass spectrometry and immunoassays are the major analytical modalities for plasma proteins. As described in the previous section, MS analysis of plasma proteins are typically performed using LC-MS, in which peptide fragments from digested proteins are separated by liquid chromatography, ionized by electro spray, and analyzed by a mass analyzer.

Peptides of similar masses can be further distinguished via tandem MS (MS/MS), which identifies peptides based on their unique MS/MS fragmentation signature. Depending on the purpose of study and the dynamic range of measurement, non-targeted or targeted proteome profiling can be performed. Non-targeted mass spectrometry focuses on discovering novel protein markers.[45–47] Immunoassay is an antibody based method for the targeted proteomics. This method relies on the high specificity and affinity of antibodies binding to antigens. Immunoassay is compatible with a variety of platforms including paper-based lateral flow devices, well plate, flow cytometry, microarray, etc., and this versatility makes it a very popular technique. Immunoassays can be classified as homogeneous, in which the antibody-antigen interaction occurring in solution, or heterogeneous, in which the interaction occurring on a surface. Quantitation mode could be either competitive or non-competitive, which requires labeled exogenous antigens or labeled detection antibody, respectively. Labels are typically fluorophores or enzymes, which transduces/amplifies antibody-antigen binding events into color, fluorescence, or luminescence readouts.[21–23]

1.5 Thesis overview: developing microfluidic platforms for precision medicine in glioblastoma multiforme

Glioblastoma multiforme (GBM) is a highly lethal, difficult to resect, malignant brain tumor with a survival time of 12-15 months. To selectively eradicate cancer cells, current treatments mostly rely on radiotherapy and drug intervention, although drug delivery is impeded by the brain blood barrier (BBB). Additionally, the somatic mutation landscape

of GBM is highly diverse and heterogeneous, with subpopulations that elude targeted therapies by rapid clonal evolution of drug resistant cells.[50,51]

GBM is perhaps the disease where precision medicine is needed the most, and it starts with the analysis of tumor biopsies. Since this cancer is highly variable, patients' genotype and phenotype should be used to stratify patients according to known databases and identify 'personalized' drug targets. To narrow down the drugs of interest, drug response should be tested *in vitro* using cells harvested from the tumor. Ideally, phenotypic changes or proliferation of these cells should be measured after mono- or combination treatment of drug candidates at several doses. While the patient receives a selected targeted therapy, the tumor response is monitored via non-invasive imaging and molecular measurement of blood plasma. The major technical challenge of precision medicine is the extraction of useful, multidimensional biological information from limited amounts of tumor and plasma biopsies.

To address this challenge, this thesis describes the development of technologies for analyzing patient biopsies. These technologies rely on microfluidic platforms to miniaturize analytical systems, enabling the manipulation and multiplexed analysis of small amounts of sample. Specifically, we developed two distinct technologies that can measure drug response in GBM. The first method enables metabolic analysis of patient-derived cancer cell lines at the single-cell level (chapter 2), while the second method enables multiplexed proteomic measurements in patient plasma (chapter 3 and 4). These microfluidic methods are designed to be very sample efficient and easily deployable in the clinic.

In chapter 2, we report an integrated microfluidic chip and beta particle imaging system, known as the Betabox. We showed its capability to measure the glycolytic activity of single cells of a human derived GBM cell line, using ^{18}F-fluorodeoxylglucose (^{18}F-FDG) as a glucose analog probe. The microfluidic chip was designed, optimized, and validated for single cell resolution. We then measured the short-term kinetic responses of single GBM cells under EGFR inhibition, targeting a receptor tyrosine kinase signaling pathway. This assay can be performed in less than 3 hours and requires small amount of cells (as low as 10,000 cells per chip). Since Betabox is a non-disruptive technique, it can be combined with other analysis techniques including optical imaging of cell sizes and immunofluorescence staining. Furthermore, we showed that Betabox can identify GBM cells that do not respond to targeted therapy, which suggested its utility as a rapid drug screening platform. Chapter 2 has been taken in part from *Technology*, 2015, 3 (4), 172-8.[42]

In chapters 3 and 4, we introduce a microfluidic method that can profile the plasma proteome to monitor the response of GBM patients to bevacizumab and buparlisib targeted therapy treatment, respectively. In chapter 3, we performed a longitudinal study, analyzing patient proteome profiles during bevacizumab treatment, an anti-angiogenic therapy of inhibiting vascular endothelial growth factor (VEGF) signaling pathways. From initial measurements of 35 proteins from 62 patient samples, we developed a proteome classifier composed of 14 predictive protein makers. In order to validate these markers, we analyzed a larger pool of 516 serum samples from 105 GBM patients. Measured plasma protein levels from 128 samples were also correlated with patient tumor volumes in mm^3 using analysis of functional neuroimages (AFNI). A mathematical model was developed to

describe the relationship between tumor responses and the 14 protein levels. In chapter 4, we measured 9 plasma proteins to monitor recurrent GBM patient responses to buparlisib, a phosphoinositide 3-kinase (PI3K) inhibitor. Monthly collected 153 plasma samples were used in this study. Proteomic classifier was developed and evaluated for its diagnostic and predictive capacity of early drug response. Both chapters have been taken in part from manuscripts in preparation.

In chapter 5, we extend the microchip technology developed for chapters 3 and 4 to screen protein catalyzed capture agents (PCCs). PCCs are triazole-closed macrocyclic peptides that serve as synthetic antibody surrogates. PCCs can be engineered to target any epitopes, including ones that are not easily addressable by antibodies. Also, due to the cyclic backbone, PCCs have superior physicochemical and biological stability compared to other biologics. A library of one bead one compound (OBOC) is screened against a synthetic epitope fragments of target protein, which typically results in 10-20 hits from 2 million sequences of the library.[52] However, a huge technological bottleneck exists in validating the hits using the full protein target. Conventional enzyme-linked immunosorbent assay (ELISA) in the 96 micro-well format takes 10-36 hours to measure the binding affinity of one single hit (or a month to characterize all 20 hits). To streamline this process, we developed a PCC screening platform using microfluidic technologies developed in chapters 3 and 4. Within 12 hours, this platform can simultaneously validate 14 PCCs that target the allosteric regulating sites of KRas, a protein whose mutation is implicated in GBM.[53] This chapter has been taken in part from a manuscript in preparation.

1.6 References

(1)   Schork, N. J. *Nature* **2015**, *520* (7549), 609.

(2)   Sadée, W.; Dai, Z. *Hum. Mol. Genet.* **2005**, *14* (SUPPL. 2), 207.

(3)   Hood, L.; Friend, S. H. *Nat. Rev. Clin. Oncol.* **2011**, *8* (3), 184.

(4)   Chin, L.; Andersen, J. N.; Futreal, P. A. *Nat. Med.* **2011**, *17* (3), 297.

(5)   Sameek, R.; Chinnaiyan, A. M. *Annu. Rev. Genomics Hum. Genet.* **2014**, *15* (1), 395.

(6)   National Institutes of Health (NIH). http://allofus.nih.gov/.

(7)   Brennan, C. W.; Verhaak, R. G. W.; McKenna, A.; Campos, B.; Noushmehr, H.; Salama, S. R.; Zheng, S.; Chakravarty, D.; Sanborn, J. Z.; Berman, S. H.; Beroukhim, R.; Bernard, B.; Wu, C. J.; Genovese, G.; Shmulevich, I.; Barnholtz-Sloan, J.; Zou, L.; Vegesna, R.; Shukla, S. A.; Ciriello, G.; Yung, W. K.; Zhang, W.; Sougnez, C.; Mikkelsen, T.; Aldape, K.; Bigner, D. D.; Van Meir, E. G.; Prados, M.; Sloan, A.; Black, K. L.; Eschbacher, J.; Finocchiaro, G.; Friedman, W.; Andrews, D. W.; Guha, A.; Iacocca, M.; O'Neill, B. P.; Foltz, G.; Myers, J.; Weisenberger, D. J.; Penny, R.; Kucherlapati, R.; Perou, C. M.; Hayes, D. N.; Gibbs, R.; Marra, M.; Mills, G. B.; Lander, E.; Spellman, P.; Wilson, R.; Sander, C.; Weinstein, J.; Meyerson, M.; Gabriel, S.; Laird, P. W.; Haussler, D.; Getz, G.; Chin, L.; Benz, C.; Barrett, W.; Ostrom, Q.; Wolinsky, Y.; Bose, B.; Boulos, P. T.; Boulos, M.; Brown, J.; Czerinski, C.; Eppley, M.; Kempista, T.; Kitko, T.; Koyfman, Y.; Rabeno, B.; Rastogi, P.; Sugarman, M.; Swanson, P.; Yalamanchii, K.; Otey, I. P.; Liu, Y. S.; Xiao, Y.; Auman, J. T.; Chen, P. C.; Hadjipanayis, A.; Lee, E.; Lee, S.; Park, P. J.; Seidman, J.; Yang, L.; Kalkanis, S.; Poisson, L. M.; Raghunathan, A.;

Scarpace, L.; Bressler, R.; Eakin, A.; Iype, L.; Kreisberg, R. B.; Leinonen, K.; Reynolds, S.; Rovira, H.; Thorsson, V.; Annala, M. J.; Paulauskis, J.; Curley, E.; Hatfield, M.; Mallery, D.; Morris, S.; Shelton, T.; Shelton, C.; Sherman, M.; Yena, P.; Cuppini, L.; DiMeco, F.; Eoli, M.; Maderna, E.; Pollo, B.; Saini, M.; Balu, S.; Hoadley, K. A.; Li, L.; Miller, C. R.; Shi, Y.; Topal, M. D.; Wu, J.; Dunn, G.; Giannini, C.; Aksoy, B. A.; Antipin, Y.; Borsu, L.; Cerami, E.; Gao, J.; Gross, B.; Jacobsen, A.; Ladanyi, M.; Lash, A.; Liang, Y.; Reva, B.; Schultz, N.; Shen, R.; Socci, N. D.; Viale, A.; Ferguson, M. L.; Chen, Q. R.; Demchok, J. A.; Dillon, L. A. L.; Mills Shaw, K. R.; Sheth, M.; Tarnuzzer, R.; Wang, Z.; Yang, L.; Davidsen, T.; Guyer, M. S.; Ozenberger, B. A.; Sofia, H. J.; Bergsten, J.; Eckman, J.; Harr, J.; Smith, C.; Tucker, K.; Winemiller, C.; Zach, L. A.; Ljubimova, J. Y.; Eley, G.; Ayala, B.; Jensen, M. A.; Kahn, A.; Pihl, T. D.; Pot, D. A.; Wan, Y.; Hansen, N.; Hothi, P.; Lin, B.; Shah, N.; Yoon, J. G.; Lau, C.; Berens, M.; Ardlie, K.; Carter, S. L.; Cherniack, A. D.; Noble, M.; Cho, J.; Cibulskis, K.; DiCara, D.; Frazer, S.; Gabriel, S. B.; Gehlenborg, N.; Gentry, J.; Heiman, D.; Kim, J.; Jing, R.; Lander, E. S.; Lawrence, M.; Lin, P.; Mallard, W.; Onofrio, R. C.; Saksena, G.; Schumacher, S.; Stojanov, P.; Tabak, B.; Voet, D.; Zhang, H.; Dees, N. N.; Ding, L.; Fulton, L. L.; Fulton, R. S.; Kanchi, K. L.; Mardis, E. R.; Wilson, R. K.; Baylin, S. B.; Harshyne, L.; Cohen, M. L.; Devine, K.; Sloan, A. E.; Van Den Berg, S. R.; Berger, M. S.; Carlin, D.; Craft, B.; Ellrott, K.; Goldman, M.; Goldstein, T.; Grifford, M.; Ma, S.; Ng, S.; Stuart, J.; Swatloski, T.; Waltman, P.; Zhu, J.; Foss, R.; Frentzen, B.; McTiernan, R.; Yachnis, A.; Mao, Y.; Akbani, R.; Bogler, O.; Fuller, G. N.; Liu, W.; Liu, Y.; Lu, Y.; Protopopov, A.; Ren, X.; Sun, Y.; Yung, W. K. A.; Zhang, J.;

Chen, K.; Weinstein, J. N.; Bootwalla, M. S.; Lai, P. H.; Triche, T. J.; Van Den Berg, D. J.; Gutmann, D. H.; Lehman, N. L.; Brat, D.; Olson, J. J.; Mastrogianakis, G. M.; Devi, N. S.; Zhang, Z.; Lipp, E.; McLendon, R. *Cell* **2013**, *155* (2), 462.

(8)   Parsons, D. W.; Parsons, D. W.; Jones, S.; Zhang, X.; Lin, J. C.; Leary, R. J.; Angenendt, P.; Mankoo, P.; Carter, H.; Siu, I.; Gallia, G. L.; Olivi, A.; Mclendon, R.; Rasheed, B. A.; Keir, S.; Nikolskaya, T.; Nikolsky, Y.; Busam, D. A.; Tekleab, H.; Jr, L. A. D.; Hartigan, J.; Smith, D. R.; Strausberg, R. L.; Kazue, S.; Marie, N.; Mieko, S.; Shinjo, O.; Yan, H.; Riggins, G. J.; Bigner, D. D.; Velculescu, V. E.; Kinzler, K. W. *Science* **2008**, *321* (5897), 1807.

(9)   Ascierto, P. A.; Kirkwood, J. M.; Grob, J.-J.; Simeone, E.; Grimaldi, A. M.; Maio, M.; Palmieri, G.; Testori, A.; Marincola, F. M.; Mozzillo, N. *J. Transl. Med.* **2012**, *10* (1), 85.

(10)   Prior, I. A.; Lewis, P. D.; Mattos, C. *Cancer Res.* **2012**, *72* (10), 2457.

(11)   Ford, D.; Easton, D. F.; Stratton, M.; Narod, S.; Goldgar, D.; Devilee, P.; Bishop, D. T.; Weber, B.; Lenoir, G.; Chang-Claude, J.; Sobol, H.; Teare, M. D.; Struewing, J.; Arason, A.; Scherneck, S.; Peto, J.; Rebbeck, T. R.; Tonin, P.; Neuhausen, S.; Barkardottir, R.; Eyfjord, J.; Lynch, H.; Ponder, B. A. J.; Gayther, S. A.; Birch, J. M.; Lindblom, A.; Stoppa-Lyonnet, D.; Bignon, Y.; Borg, A.; Hamann, U.; Haites, N.; Scott, R. J.; Maugard, C. M.; Vasen, H.; Seitz, S.; Cannon-Albright, L. A.; Schofield, A.; Zelada-Hedman, M. *Am. J. Hum. Genet.* **1998**, *62* (3), 676.

(12)   M. C. King; Marks, J.; Mandell, J. *Science* **2003**, *302* (5645), 643.

(13)   Yi, S.; Lin, S.; Li, Y.; Zhao, W.; Mills, G. B.; Sahni, N. *Nat. Rev. Genet.* **2017**, *18* (7), 395.

(14)   Hanahan, D.; Weinberg, R. A. *Cell* **2011**, *144* (5), 646.

(15)   Pavlova, N. N.; Thompson, C. B. *Cell Metab.* **2016**, *23* (1), 27.

(16)   Garralda, E.; Paz, K.; López-Casas, P. P.; Jones, S.; Katz, A.; Kann, L. M.; López-Rios, F.; Sarno, F.; Al-Shahrour, F.; Vasquez, D.; Bruckheimer, E.; Angiuoli, S. V.; Calles, A.; Diaz, L. A.; Velculescu, V. E.; Valencia, A.; Sidransky, D.; Hidalgo, M. *Clin. Cancer Res.* **2014**, *20* (9), 2476.

(17)   Girotti, M. R.; Gremel, G.; Lee, R.; Galvani, E.; Rothwell, D.; Viros, A.; Mandal, A. K.; Lim, K. H. J.; Saturno, G.; Furney, S. J.; Baenke, F.; Pedersen, M.; Rogan, J.; Swan, J.; Smith, M.; Fusi, A.; Oudit, D.; Dhomen, N.; Brady, G.; Lorigan, P.; Dive, C.; Marais, R. *Cancer Discov.* **2016**, *6* (3), 286.

(18)   Pauli, C.; Hopkins, B. D.; Prandi, D.; Shaw, R.; Fedrizzi, T.; Sboner, A.; Sailer, V.; Augello, M.; Puca, L.; Rosati, R.; Mcnary, T. J.; Churakova, Y.; Cheung, C.; Triscott, J.; Pisapia, D.; Rao, R.; Mosquera, J. M.; Robinson, B.; Faltas, B. M.; Emerling, B. E.; Gadi, V. K.; Bernard, B.; Elemento, O.; Beltran, H.; Demichelis, F.; Kemp, C. J.; Grandori, C.; Cantley, L. C.; Rubin, M. A. *Cancer Discov.* **2017**, *7* (5), 462.

(19)   Willmann, J. K.; van Bruggen, N.; Dinkelborg, L. M.; Gambhir, S. S. *Nat. Rev. Drug Discov.* **2008**, *7* (7), 591.

(20)   Siravegna, G.; Marsoni, S.; Siena, S.; Bardelli, A. *Nat. Rev. Clin. Oncol.* **2017**.

(21)   Song, P.; Hu, R.; Tng, D. J. H.; Yong, K.-T. *RSC Adv.* **2014**, *4* (22), 11499.

(22)   Liu, Z.; Han, X.; Qin, L. *Adv. Healthc. Mater.* **2016**, *5* (8), 871.

(23)   Ng, A. H. C.; Uddayasankar, U.; Wheeler, A. R. *Anal. Bioanal. Chem.* **2010**, *397* (3), 991.

(24)   Polyak, K. *Nat. Med.* **2014**, *20* (4), 344.

(25)   Bedard, P. L.; Hansen, A. R.; Ratain, M. J.; Siu, L. L. *Nature* **2013**, *501* (7467), 355.

(26)   Meacham, C. E.; Morrison, S. J. *Nature* **2013**, *501* (7467), 328.

(27)   Vogelstein, B.; Papadopoulos, N.; Velculescu, V. E.; Zhou, S.; Diaz, L. A.; Kinzler, K. W. *Science* **2013**, *339* (6127), 1546.

(28)   Garraway, L. A.; Jänne, P. A. *Cancer Discov.* **2012**, *2* (3), 214.

(29)   Heath, J. R.; Ribas, A.; Mischel, P. S. *Nat. Rev. Drug Discov.* **2015**, *15* (3), 204.

(30)   Navin, N.; Kendall, J.; Troge, J.; Andrews, P.; Rodgers, L.; McIndoo, J.; Cook, K.; Stepansky, A.; Levy, D.; Esposito, D.; Muthuswamy, L.; Krasnitz, A.; McCombie, W. R.; Hicks, J.; Wigler, M. *Nature* **2011**, *472* (7341), 90.

(31)   Wu, A. R.; Neff, N. F.; Kalisky, T.; Dalerba, P.; Treutlein, B.; Rothenberg, M. E.; Mburu, F. M.; Mantalas, G. L.; Sim, S.; Clarke, M. F.; Quake, S. R. *Nat. Methods* **2013**, *11* (1), 41.

(32)   Quadri, S. M. S. *West. Blotting Methods Protoc.* **2015**, *11* (7), 455.

(33)   Love, J. C.; Ronan, J. L.; Grotenbreg, G. M.; van der Veen, A. G.; Ploegh, H. L. *Nat. Biotechnol.* **2006**, *24* (6), 703.

(34)   Bendall, S. C.; Simonds, E. F.; Qiu, P.; Amir, E. D.; Krutzik, P. O.; Finck, R.; Bruggner, R. V; Melamed, R.; Trejo, A.; Ornatsky, O. I.; Balderas, R. S.; Plevritis, S. K.; Sachs, K.; Pe, D.; Tanner, S. D.; Nolan, G. P. *Science* **2011**, *332* (6030), 687.

(35)   Xue, M.; Wei, W.; Su, Y.; Kim, J.; Shin, Y. S.; Mai, W. X.; Nathanson, D. A.; Heath, J. R. *J. Am. Chem. Soc.* **2015**, *137* (12), 4066.

(36)   Tirosh, I.; Izar, B.; Prakadan, S. M.; Wadsworth, M. H.; Treacy, D.; Trombetta, J. J.; Rotem, A.; Rodman, C.; Lian, C.; Murphy, G.; Fallahi-Sichani, M.; Dutton-

Regester, K.; Lin, J.-R.; Cohen, O.; Shah, P.; Lu, D.; Genshaft, A. S.; Hughes, T. K.; Ziegler, C. G. K.; Kazer, S. W.; Gaillard, A.; Kolb, K. E.; Villani, A.-C.; Johannessen, C. M.; Andreev, A. Y.; Van Allen, E. M.; Bertagnolli, M.; Sorger, P. K.; Sullivan, R. J.; Flaherty, K. T.; Frederick, D. T.; Jane-Valbuena, J.; Yoon, C. H.; Rozenblatt-Rosen, O.; Shalek, A. K.; Regev, A.; Garraway, L. A. *Science* **2016**, *352* (6282), 189.

(37)   Deberardinis, R. J.; Thompson, C. B. *Cell* **2012**, *148* (6), 1132.

(38)   Gatenby, R. A.; Gillies, R. J. *Nat. Rev. Cancer* **2004**, *4* (11), 891.

(39)   Wishart, D. S. *Nat. Rev. Drug Discov.* **2016**, *15* (7), 473.

(40)   Comi, T. J.; Do, T. D.; Rubakhin, S. S.; Sweedler, J. V. *J. Am. Chem. Soc.* **2017**, *139* (11), 3920.

(41)   Spitzer, M. H.; Nolan, G. P. *Cell* **2016**, *165* (4), 780.

(42)   Shin, Y. S.; Kim, J.; Johnson, D.; Dooraghi, A. A.; Mai, W. X.; Ta, L.; Chatziioannou, A. F.; Phelps, M. E.; Nathanson, D. A.; Heath, J. R. *Technology* **2015**, *3* (4), 172.

(43)   Zhang, Y.; Tang, Y.; Sun, S.; Wang, Z.; Wu, W.; Zhao, X.; Czajkowsky, D. M.; Li, Y.; Tian, J.; Xu, L.; Wei, W.; Deng, Y.; Shi, Q. *Anal. Chem.* **2015**, *87* (19), 9761.

(44)   Tang, Y.; Wang, Z.; Li, Z.; Kim, J.; Deng, Y.; Li, Y.; Heath, J. R.; Wei, W.; Tang, Y.; Wang, Z.; Li, Z.; Kim, J.; Deng, Y.; Li, Y.; Heath, J. R.; Wei, W. *Proc. Natl. Acad. Sci.* **2017**, *114* (10), 2544.

(45)   Altelaar, A. F. M.; Munoz, J.; Heck, A. J. R. *Nat. Rev. Genet.* **2012**, *14* (1), 35.

(46)   Whiteaker, J. R.; Lin, C.; Kennedy, J.; Hou, L.; Trute, M.; Sokal, I.; Yan, P.; Schoenherr, R. M.; Zhao, L.; Voytovich, U. J.; Kelly-Spratt, K. S.; Krasnoselsky,

A.; Gafken, P. R.; Hogan, J. M.; Jones, L. A.; Wang, P.; Amon, L.; Chodosh, L. A.; Nelson, P. S.; McIntosh, M. W.; Kemp, C. J.; Paulovich, A. G. *Nat. Biotechnol.* **2011**, *29* (7), 625.

(47) Geyer, P. E.; Kulak, N. A.; Pichler, G.; Holdt, L. M.; Teupser, D.; Mann, M. *Cell Syst.* **2016**, *2* (3), 185.

(48) Westphal, M.; Lamszus, K. *Nat. Rev. Neurol.* **2015**, *11* (10), 556.

(49) Borrebaeck, C. A. K. *Nat. Rev. Cancer* **2017**, *17* (3), 199.

(50) Cloughesy, T. F.; Cavenee, W. K.; Mischel, P. S. *Annu. Rev. Pathol. Mech. Dis.* **2014**, *9* (1), 1.

(51) Prados, M. D.; Byron, S. A.; Tran, N. L.; Phillips, J. J.; Molinaro, A. M.; Ligon, K. L.; Wen, P. Y.; Kuhn, J. G.; Mellinghoff, I. K.; De Groot, J. F.; Colman, H.; Cloughesy, T. F.; Chang, S. M.; Ryken, T. C.; Tembe, W. D.; Kiefer, J. A.; Berens, M. E.; Craig, D. W.; Carpten, J. D.; Trent, J. M. *Neuro. Oncol.* **2015**, *17* (8), 1051.

(52) Das, S.; Nag, A.; Liang, J.; Bunck, D. N.; Umeda, A.; Farrow, B.; Coppock, M. B.; Sarkes, D. A.; Finch, A. S.; Agnew, H. D.; Pitram, S.; Lai, B.; Yu, M. B.; Museth, A. K.; Deyle, K. M.; Lepe, B.; Rodriguez-Rivera, F. P.; McCarthy, A.; Alvarez-Villalonga, B.; Chen, A.; Heath, J.; Stratis-Cullum, D. N.; Heath, J. R. *Angew. Chemie - Int. Ed.* **2015**, *54* (45), 13219.

(53) Wakimoto, H.; Tanaka, S.; Curry, W. T.; Loebel, F.; Zhao, D.; Tateishi, K.; Chen, J.; Klofas, L. K.; Lelic, N.; Kim, J. C.; Dias-Santagata, D.; Ellisen, L. W.; Borger, D. R.; Fendt, S. M.; Vander Heiden, M. G.; Batchelor, T. T.; John Iafrate, A.; Cahill, D. P.; Chi, A. S. *Clin. Cancer Res.* **2014**, *20* (11), 2898.

Chapter 2

Quantitative assessments of glycolysis from single cells

2.1 Introduction

Recent advances in single cell proteomics, genomics, and transcriptomics methods have shown promise towards uncovering fundamental biological phenomena that are unresolved when bulk cell populations are interrogated.[1,2] By contrast, single cell metabolic assays have remained relatively unexplored, although recent progress in both mass spectrometric[3] and microchip methods is promising.[4] The rapid response of cellular metabolic responses to many drugs makes metabolic assays a valuable tool for rapid screening assays and investigating early biological responses to treatments. Such assays, if carried out at the single cell level, have the potential to identify metabolic outliers—i.e. individual cells exhibiting responses to drugs that are well above or below the population average. The identification of such outliers in a manner that permits further analysis at the genomic or transcriptomic level may offer new insights for understanding therapeutic resistance.

We report on an integrated microfluidic chip / beta-particle imaging camera (the Betabox) that is a first step for enabling such questions to be explored. An accelerated rate of aerobic glycolysis within many tumors (the Warburg effect) provides the diagnostic basis for using a glucose analog, 2-deoxy-2-[F-18]fluoro-D-glucose (^{18}F-FDG), as a

positron emission tomography (PET) *in vivo* molecular imaging probe[5] of the rate of glycolysis within tumors. ^{18}F-FDG PET can also be used to image the metabolic responses of those tumors to drugs. In a similar manner, ^{18}F-FDG can serve as a radio-labeled probe to measure altered states of glycolysis in cancer cells *in vitro*, including alterations in glycolytic rates that are induced by therapeutic interventions. We recently reported on a microfluidic platform mated to a beta particle imaging camera of the Betabox.[6–8] The Betabox was used to analyze the short time frame (~hour) influence of targeted inhibitors on glycolysis in cell populations. We measured the glycolytic response of the model glioblastoma (GBM) cell line, U87EGFRvIII, to inhibition of the epidermal growth factor receptor (EGFR) by erlotinib.[6] As anticipated from PET ^{18}F-FDG in cancer patients, erlotinib treatment of the U87EGFRvIII cells reduced the rate of glycolysis, although, surprisingly, that reduction was uneven over the 4-hours following start of treatment. This uneven decrease in glycolysis was accompanied by oscillations in the levels of various phosphoproteins downstream of EGFR signaling.

In the present study, we report on a redesign of Betabox that permits a similar kinetic study, but at the level of single cells. The modified Betabox is shown to be sufficiently sensitive and quantitative that the variance of glycolysis across a statistical number of single cells is resolved for the first time. The assay is non-destructive to the cells, and the results may be integrated with optical microscopy measurements that permit the rates of glycolysis to be compared against cell size.

2.2 Materials and methods

2.2.1 Betabox assay platform

The Betabox assay platform consists of a silicon-based β-particle imaging camera (Betabox camera) and a polydimethylsiloxane (PDMS)-based microfluidic chip (Betabox device). The Betabox camera was validated and operated as previously described. The design in this paper is developed based on the general considerations of previous work. The current version of the Betabox device, however, has improved the measurement sensitivity about 20% by implementing a thinner bottom PDMS film (13 μm, instead of 50 μm used in previous report) between position-sensitive avalanche photodiode (PSAPD, Radiation Monitoring Devices) and the cells. This improvement in measurement sensitivity enables single cell-based metabolic measurements. To make the fabrication process simpler, all the features, including the dust filter and cell traps are moved to the top layer.

The Betabox microchip device has 3 key features: 1) a cell trap array, 2) inlet filters, and 3) a perfusion channel (Figure 2.1 and Figure 2.6, Appendix A). Different designs permitted different numbers of cell traps (1-, 7-, or 40-cell traps) depending on the purpose of the study. Each individual cell trap consists of 2 micro hurdles with 5μm gap. The shape of the cell trap was optimized to minimize the chance of trapping more than one cell per chamber (Figure 2.6c). We utilized two different configurations of solution inlets. By sharing a single inlet for all the channels, we can test a single condition per device (Figure 1b). Testing multiple conditions, such as in a kinetic study, is enabled by placing independent inlets/outlets for each channel (Figure 2.6d). The inlet filters are essential for preventing dust, cell debris, or clumped cells from blocking the active region of cell traps. Detailed shape, layout, and dimensions of the filter region are shown in Figure 2.6b. Two

sets of inlets and filters are placed upstream to minimize the failure rate of the device due to unexpected clogging.

Analysis on single cells can be achieved by measuring multiple devices for a single condition. As described in Figure 2.2, the Betabox signals can be adjusted to a single time point (usually the first or the last time point) based calibrations against the decay of ^{18}F-FDG radioactivity. Cell loading efficiency for cell traps is around 90%. However, a single trap can capture two or more cells and trapped single cells can be lost during the handling. The final loading efficiency for single cells is 50-80%. Currently up to 20 Betabox devices can be measured in a single day and the yield of single cell measurement will be improved through the further optimization of the test protocol.

2.2.2 Betabox device fabrication

The Betabox device consists of 2 PDMS layers fabricated by standard soft lithography methods. The top layer is ~5mm thick, and contains all the described key features of the Betabox device in microchannels with ~30 μm height. The top layer is molded with a master fabricated by standard photolithography with SU-8 2025 photoresist (Microchem) on a silicon wafer. The master is treated with trimethylsilyl chloride (TMCS, Sigma Aldrich) for 10 minutes before each use. 10:1 mixture (w/w) of PDMS prepolymer and curing agent (Sylgard 184®, Corning) was poured onto the master, degassed in a vacuum chamber, and baked at 80ºC for 2 hours. The cured PDMS slab was peeled off from the master, and holes for inlets and outlets were punched. The bottom layer used in this study is ~13 μm thick, and it does not contain any features. 25mm×75 mm sized, 1mm thick, pre-cleaned glass slides (Gold Seal® Rite-on® Microslides, Gold Seal® Products) were

cleaned with piranha solution (3 Sulfuric acid : 1 hydrogen peroxide, v/v) at 120°C for 20 minutes followed by through rinsing with distilled water and drying at 80°C for 20 minutes. Dried glass slides were treated with TMCS for 30 minutes. The degassed 10:1 mixture (w/w) of PDMS prepolymer and curing agent was poured onto the treated glass slide and was spun at 4000 rpm for 1 minute followed by baking at 80°C for 1 hour. The top and bottom PDMS layers were irreversibly bonded by plasma treatment (PDC-32G, Harrick Plasma) for 1 minute.

2.2.3 System evaluation with radioactive phantoms

Radioactive phantoms were prepared based on the Betabox device layout by printing a mixture of ink and ^{18}F-FDG solution on Epson Ultra Premium photo paper GLOSSY with an inkjet printer (Canon iP4700 printer). The ink cartridge was emptied prior to printing the radioactive phantoms. 1mL of ink mixture containing 3.7×10^7 Bq/ml ^{18}F-FDG was prepared and injected into the ink cartridge. The level of radioactivity was adjusted with a radiometer (ATOMLAB^{TM} 500 BIODEX). β-particles, generated from the disintegration of printed ^{18}F-FDG pattern, were captured by the Betabox with 5 minutes of acquisition time. The results were used to check the measurement error of the Betabox by location and to calibrate the decay of ^{18}F-FDG radioactivity (Figure 2.2 and Table 2.2, Appendix B).

2.2.4 Cell culture and drug treatment

GBM39 primary neurospheres and HK393 cells were cultured in Dulbecco's Modified Eagle Media Nutrient Mix F-12 (DMEM/F12, Invitrogen) supplemented with B27

(Invitrogen), Glutamax (Invitrogen), Heparin (1µg/mL), Epidermal Growth Factor (EGF, 20ng/mL, Sigma), Fibroblast Growth Factor (FGF, 20ng/mL, Sigma), and 100 U/mL of penicillin and streptomycin (Gibco) in a humidified 5% CO_2 (v/v) incubator, at 37°C. For the drug treatment, 1 million cells were suspended in 10 mL of media containing 1 µM erlotinib (ChemieTek / Selleckchem). The cells were then treated for designated periods of time and processed for tests. For the growth curve experiments, GBM39 primary neurospheres and HK393 cells were cultured in the same media conditions with or without 1 µM erlotinib. Cells were counted and passaged with medium replenishment every 3-4 days.

2.2.5 The Betabox assay procedures

1) *^{18}F-FDG treatment.* Single cell suspension was prepared from the GBM39 neurospheres, HK393 cells, or the erlotinib treated, pre-dissociated GBM39 / HK393 cells. 1×10^6 cells / mL were treated with 3.7×10^7 Bq/mL ^{18}F-FDG in the glucose free medium (Table S1) in a 5% CO_2 (v/v) humidified incubator at 37°C for 1 hour. After treatment, cells were washed with the full medium three times to remove residual unbound ^{18}F-FDG.

2) *Betabox measurement.* The device was first filled with glucose free medium before the assay was executed. 5-10 µL of ^{18}F-FDG treated GBM39 / HK393 cells, prepared at a concentration of 2×10^6 cells / mL in the glucose free medium, were loaded by applying negative pressure with a 1mL syringe from the outlet. After cell trapping, about 80 µL of glucose free media was flown to remove untrapped cells. For the measurement, the Betabox device was aligned with the Betabox camera and image was acquired for 5 minutes. A custom-coded Matlab (Natick) program was used to control the Betabox, collect, and

analyze the data. After radioactivity measurement, optical images of the captured cells were recorded with a microscope (Nikon Eclipse T*i*-S) for cell count and size measurement.

3) *Data analysis.* Depending on the Betabox device design, 20 or 30 rectangular regions of interest (ROIs) were set on the radio-image, and the total measured β-particle count in each ROI was quantified by the custom-coded Matlab program. The average of the total β-particle count from all the empty chambers was used as the background level. This background level was subtracted from the total β-particle count for each chamber with cells. Counts per minute (CPM) refers to the actual total β-particle counts from a chamber divided by the acquisition time (5 minutes for this study). CPM/cell values were calculated, dividing CPM by the number of captured cells in a chamber. CPM/cell data, from multiple Betabox assays in a day, were adjusted considering the time interval between the assays based on the calibration data. Since the detected decay of the ^{18}F-FDG radioactivity exactly follows the theoretical prediction, all the data obtained at different time points could be adjusted to the ones at a single time point for direct comparison. Cell size was measured from the optical image with ImageJ (NIH). The equivalent diameter of each cell was calculated based on the 2D area of captured cells. Cell volume calculated with the equivalent diameter (with the assumption that a cell has a spherical shape) was used for the correlation analysis.

2.2.6 Statistical analysis

The levels of glycolysis were measured as CPM/cell and mean values plus and minus the standard deviation were also presented along with the single cell measurement values. To

compare control and erlotinib-treated groups with various treatment times unpaired, two-tailed student t-tests were performed to determine whether the conditions produced significantly different results. P values less than or equal to 0.005 were considered statistically significant. For the correlation analysis between cells size and glycolysis level, Spearman correlation value was calculated between cell volume and CPM and the correlation value was 0.36 (p value=0.006).

2.3 Results and discussion
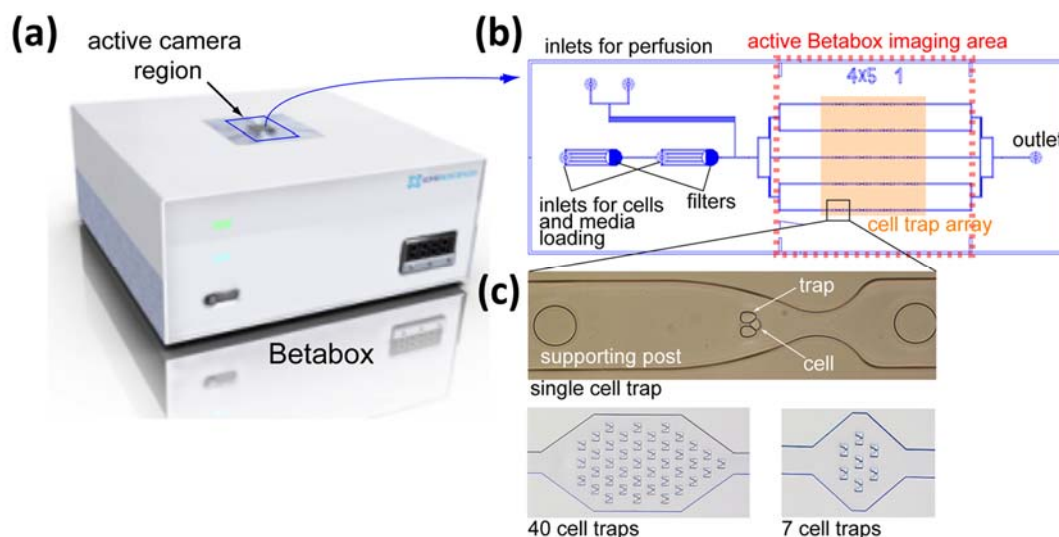
Figure 2.1 The Betabox and device design. (a) Image of the Betabox. The Betabox device is placed on the active camera region for the measurement. (b) CAD image of the Betabox microfluidic device. (c) Optical image of the single cell trap with a captured cell (top) and examples of the flexible designs of cell traps (bottom).

The Betabox is composed of two chips; a position-sensitive silicon avalanche photodiode detector to image and measure beta-particle emission from probes radio-labeled with positron emitting isotopes, ^{14}C, ^{18}F, etc., and a polydimethylsiloxane (PDMS) microfluidic chip for capturing cells in culture media. The microfluidic chip is placed on

the Si camera. The layout of the Betabox with representative examples of microfluidic chip designs containing cell traps are illustrated in Figure 2.1. The Si camera can image and measure beta particle emission simultaneously from each of the cell traps. The Si camera of the Betabox has been previously validated and described elsewhere.[7,8]

The microfluidic chip is a 2-layer device fabricated with standard photolithography and rapid prototyping methods (see Appendix A).[9] The chips used for this study have either 4 or 5 cell capture microchambers in each of 5 or 6 separate channels, respectively. Thus, each microfluidic chip has either 20 or 30 chambers as an array format of 4 by 5 or 5 by 6. All the chambers can be used for a single test condition by sharing a common inlet (Figure 2.1b). A modified design with separate inlets and outlets for each channel permits 5 or 6 independent assays per chip, such as those required to perform a kinetic study (Figure 2.6d, Appendix A). Several features in the chip design promote high signal sensitivity and single cell spatial resolution. The first feature is a thin bottom membrane of the chip that separates the cells from the camera, and is designed to minimize signal attenuation of the beta particles emitted by radio-labeled probe in the microfluidic chip. We tested several membrane thicknesses by utilizing various spin coating speeds during the PDMS bottom layer fabrication step (Figure 2.7, Appendix A). A 13 μm-thick membrane was found to offer an optimized combination of signal sensitivity and mechanical strength, and yielded 20% increase in the sensitivity for detecting the beta particle emission from the radio-labeled probes relative to our previous design (Figure 2.7, Appendix A).[6] A second design feature is the cell traps, which draw from previous literature.[10,11] The cell traps, coupled with the transparent microfluidic chip, permit direct observation and recording of which traps contain single cells. The optical image can be registered with the Si camera image to

assign rates of glycolysis to the individual cells. A third feature is the inlet filters, which are designed to prevent particles and clumped cells from clogging the active areas of the microfluidic chip. Design details are shown in Figure 2.6, Appendix A.

The Betabox performance was evaluated by using phantoms that were printed using an inkjet on glossy photographic paper. The printed pattern replicated the microfluidic chip design, with each location containing ^{18}F-FDG (Figures 2.1b and 2.2a).[7,12] The Si camera recording of beta particle emission from each location of the phantom showed a 5% of coefficient of variation (CV) (Table 2.2, Appendix B). This variation is likely attributable to small variations in the PDMS membrane thickness, but, whatever the source, the low CV value indicates that the intrinsic error of the Betabox is low. A related, previously reported evaluation that was designed to account for the inkjet printer error revealed a CV of below 2%.[7] A time course measurement of the ^{18}F decay curve from the phantom was also recorded over a 12-hour period at 15-minute intervals (Figure 2.2b). The measured time-dependence of the activities follows the known ^{18}F half-life of 109.8 minutes. This result provides calibration data for combining results from multiple independent Betabox measurements, thus significantly increasing the statistical sampling of the single cell measurements.

The Betabox design, with its 5 independent microchannels, each designed with a selected number of cell traps, permits kinetic assays of glycolysis under drug treatments at the single cell level (Figure 2.6d, Appendix A). As a demonstration, we measured the alteration in glycolysis of a patient-derived, EGFR over-expressing glioblastoma neurosphere tumor model (GBM39) to EGFR inhibition with erlotinib. We determined glycolysis at 1, 4, 12, and 24 hours following start of treatment versus the untreated control

(Figures 2.3a to 2.3d). To validate the single cell platform, experimental assays were compared. The first was the Betabox design with 5 independent channels, each containing 4 chambers with 40-cell traps (Figure 2.6d, Appendix A). The ~40-50% reduction in glycolysis following 24 hours erlotinib treatment (Fig 2.3a, b) is in reasonable agreement with both *in vivo* measurements (using ^{18}F-FDG PET) of a GBM39 mouse xenograft tumor model.[4] The Betabox platform, applied to cell populations, has also been previously validated against bulk in vitro radioassays using standard methods.[6] These results indicate that the 40-cell trap design (Fig 2.1c) yields a reliable population-based analysis.
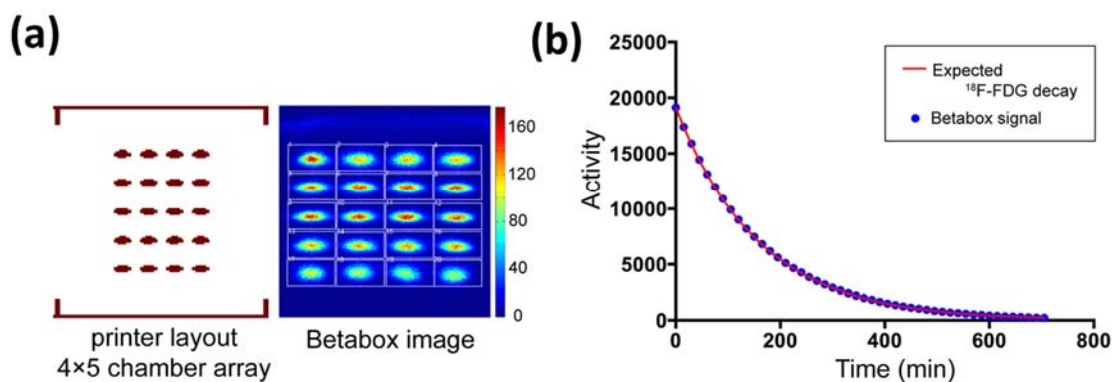
Figure 2.2 The Betabox calibration. (a) Image of the printer layout used for evaluating the Betabox performance (left) and the actual acquired image of the printed pattern with the Betabox (right). Signal is collected from each ROIs shown in the image. (b) ^{18}F-FDG activity imaged with the Betabox for 12 hours. Printed ^{18}F-FDG pattern shown in (a) was used to measure the decay of ^{18}F-FDG activity. The activities acquired with the Betabox exactly follow the expected decay of ^{18}F-FDG activity with the known ^{18}F-FDG half- life, 110 min.

The second assay was with the Betabox designed for single cell resolution: 5 microchannels, each containing 4 chambers with a single cell trap (Figure 2.1c, bottom). GBM39 cells have been shown previously to exhibit decreased glycolysis with ^{18}F-FDG upon erlotinib treatment.[13] The 40-trap device captured a slightly increased signal with 1-hour treatment, followed by a significant decrease at 12 and 24 hours (Figure 2.3b).

Averaged signal intensities of single cells showed a similar response, although the single cell measurements provided additional information that demonstrated the heterogeneity of glycolytic alterations within individual cells (Figure 2.3d). For a more in-depth analysis of the heterogeneity, we chose two conditions (control vs. 24 hours erlotinib treatment) and tested them with five sets of microfluidic chips per condition. These independent measurements were corrected for the decay of ^{18}F activity based on the calibration data and then, for each separate condition, combined. Out of 100 cell traps, 43 and 46 traps captured single cells for the control and the drug-treated condition, respectively. Erlotinib treatment decreased glycolysis by approximately 40%, with a standard deviation that was decreased by ~55%, relative to control. This measured variance in glycolysis of GBM39 cells is an important aspect of the Betabox technology as the metabolic outliers may have value for understanding therapeutic resistance.[14]
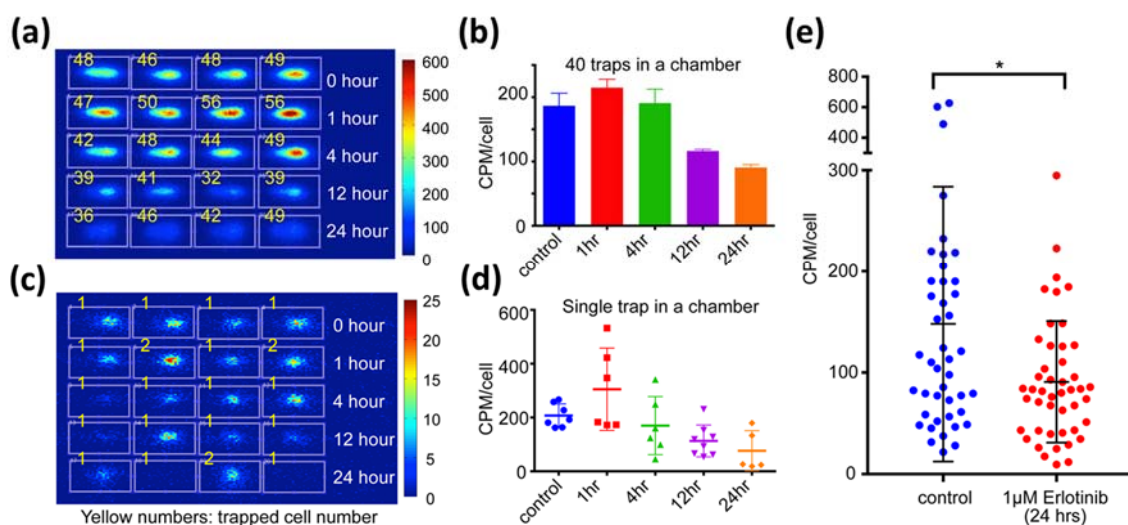
Figure 2.3 The Betabox measurement of GBM 39 cells with erlotinib treatment. (a) Image of the ^{18}F-FDG activity of 30-50 GBM 39 cells under erlotinib treatment with various treatment times (0, 1, 4, 12, and 24 hours). (b) Quantified ^{18}F-FDG activity per cell from (a). (c) Image of the ^{18}F-FDG activity of single GBM 39 cells under erlotinib treatment with various treatment times (0, 1, 4, 12, and 24 hours). (d) Quantified ^{18}F-FDG activity per cell from (c). (e) ^{18}F-FDG activity of GBM39 single cells with/without erlotinib treatment measured with multiple devices.
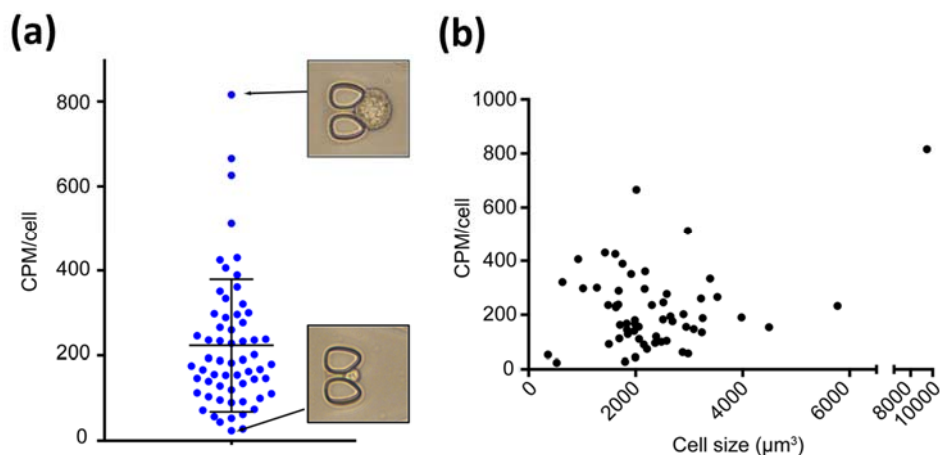
Figure 2.4 Cell size vs. ^{18}F-FDG uptake of GBM39 cells. (a) ^{18}F-FDG uptake level of single GBM 39 cells. Representative images of actual cells in two extreme cases are shown as well. (b) Scatter plot of ^{18}F-FDG uptake level versus cell size shows no correlation between the two parameters.

The transparency of the PDMS microfluidic chip, coupled with knowledge of the cell-trap locations, permit simultaneous measurements of cell morphology and size. GBM39 cells, by their nature, are characterized by a broad distribution of cell sizes. In these Betabox studies, it is straightforward to determine whether the heterogeneity in cell size is associated with a corresponding heterogeneity in glycolysis. We investigated this relationship for 58 single cells. Images of cells for the two extreme cases are shown in Figure 2.4a. Even though the two extreme cases point to a correlation between cell size and glycolysis, only a weak positive correlation (Spearman correlation of 0.36 with p-value of 0.006) was detected when the whole population was analyzed (Figure 2.4b). Using a single cell barcode chip (SCBC) platform, we recently reported on a combined analysis of metabolites and phosphoprotein signaling pathways from statistical numbers of single cells separated from a GBM39 tumor model. In that study, we found that two metabolic phenotypes dominate the measured cellular heterogeneity: 80% of the cells exhibit high

glucose uptake and low cAMP and cGMP, while 20% of the cells exhibit high cAMP and cGMP, but low glucose uptake.[4] Unlike the Betabox, the SCBC analysis is destructive to the cells, and so the gene regulatory networks that underlie this metabolic heterogeneity could not be identified. However, the single cell Betabox platform should permit the metabolic outliers to be further analyzed via exome or transcriptomic analysis. This is a major power of the platform.
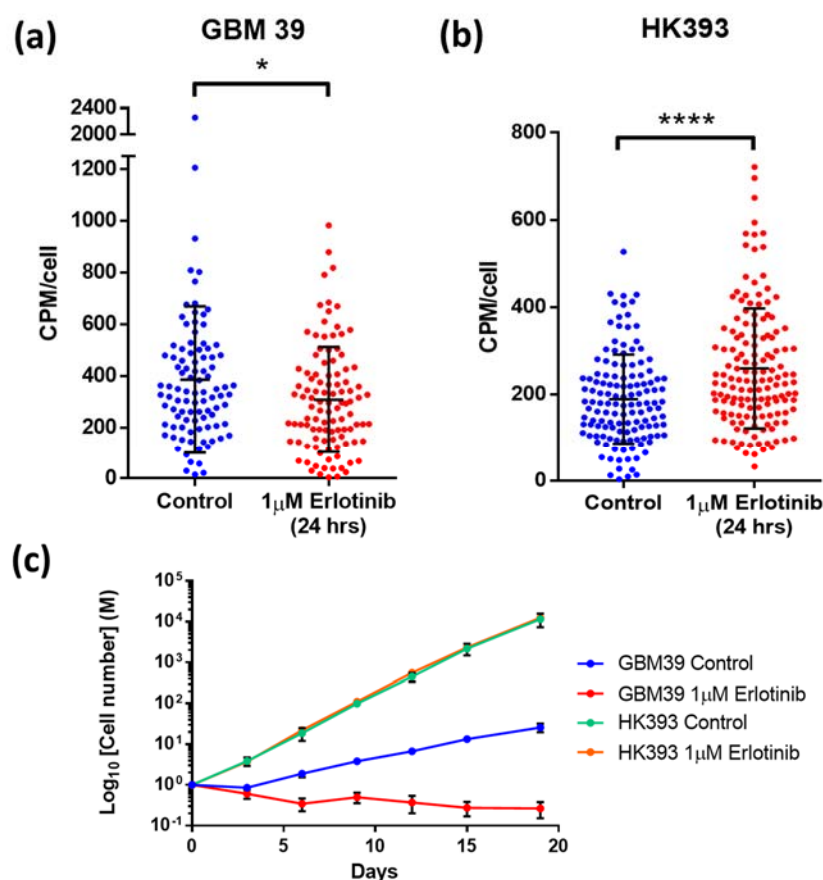
Figure 2.5 Early metabolic response is a predictive marker for a long-term drug efficacy. (a) Metabolic activity of GBM39 cells with / without erlotinib treatment. 24 hours of treatment decreased ~20% average ^{18}F-FDG uptake (control: 96 cells and drug treated: 106 cells) (b) Metabolic activity of HK393 cells with/without erlotinib treatment. 24 hours of treatment increased ~35% average ^{18}F-FDG uptake (control: 133 cells and drug treated: 137 cells). (c) Growth curves of GBM39 and HK393 cells with / without erlotinib treatment. The growth of HK393 cells was not affected by erlotinib treatment whereas the growth of GBM39 cells was inhibited. (*, $p<0.05$; ****, $p<0.001$).

Furthermore, the Betabox can be a rapid assay platform to screen potentially effective drugs for model GBM cell lines (Figure 2.5). Previous ^{18}F-FDG PET clinical studies reported that early metabolic responses of cancer patients to a drug treatment may be a predictive marker for long-term drug efficacy.[15,16] Here the metabolic responses were defined by the changes in ^{18}F-FDG uptake, and the decrease of measured activities after short-term drug treatment predicted the long-term drug efficacy. We demonstrated that the Betabox can be also used for the same drug efficacy assessment *in vitro*. The metabolic responses of 2 GBM cell lines, GBM39 and HK393, to 24 hours erlotinib treatment were measured by the Betabox. GBM39 cells showed the decrease in ^{18}F-FDG uptake whereas HK393 cells actually showed the increase. Then, the growth of GBM39 and HK393 cells was monitored during 19 days with / without erlotinib. As expected, only the growth of GBM39 cells were inhibited by erlotinib treatment. This observation corresponded to those previous studies and proposed that the Betabox platform can be used in the drug screening process.

2.4 Conclusion

We have demonstrated the Betabox design that has sufficient sensitivity and spatial resolution to provide images and robust/quantitative measurements of glycolysis with ^{18}F-FDG in single cells. We applied this technology for quantitative assays of glycolysis in single GBM cells over a time period of a few hours following erlotinib treatment. The variance in glycolysis across a statistical number of single cells was resolved. For both control and drug treated GBM39 cells, the variation in glycolysis across single cells was broad, with standard deviation values of approximately 92% and 66% of the average,

respectively. Furthermore, this variation exhibited only a weak correlation with the broad distribution of cell sizes that are characteristic of the GBM39 cells. We also showed that this platform can be used for the rapid screening of potentially effective drugs for model GBM cell lines. The Betabox assay is non-destructive to the cells, and so further molecular analysis of the radioassayed cells should permit deeper insights into this heterogeneity.[17] In addition, there is a wide range of available PET probes for various metabolic, signal transduction, synthetic processes associated with disease states. The Betabox can thus serve as a valuable tool for quantitating the heterogeneity of various biological functions in single cells and for helping explore the implications of that heterogeneity in disease and disease treatments.[18]

2.5 References

(1)   Yu, J.; Zhou, J.; Sutherland, A.; Wei, W.; Shin, Y. S.; Xue, M.; Heath, J. R. *Annu. Rev. Anal. Chem.* **2014**, *7* (1), 275.

(2)   Blainey, P. C.; Quake, S. R. *Nat. Methods* **2014**, *11* (1), 19.

(3)   Zenobi, R. *Science* **2013**, *342* (6163), 1243259.

(4)   Xue, M.; Wei, W.; Su, Y.; Kim, J.; Shin, Y. S.; Mai, W. X.; Nathanson, D. A.; Heath, J. R. *J. Am. Chem. Soc.* **2015**, *137* (12), 4066.

(5)   Gatenby, R. A.; Gillies, R. J. *Nat. Rev. Cancer* **2004**, *4* (11), 891.

(6)   Wang, J.; Hwang, K.; Braas, D.; Dooraghi, A.; Nathanson, D.; Campbell, D. O.; Gu, Y.; Sandberg, T.; Mischel, P.; Radu, C.; Chatziioannou, A. F.; Phelps, M. E.; Christofk, H.; Heath, J. R. *J. Nucl. Med.* **2013**, *54* (10), 1820.

(7)   Dooraghi, A. A.; Vu, N. T.; Silverman, R. W.; Farrell, R.; Shah, K. S.; Wang, J.;

Heath, J. R.; Chatziioannou, A. F. *Phys. Med. Biol.* **2013**, *58* (11), 3739.

(8) Vu, N. T.; Yu, Z. T. F.; Comin-Anduix, B.; Søndergaard, J. N.; Silverman, R. W.; Chang, C. Y. N.; Ribas, A.; Tseng, H.-R.; Chatziioannou, A. F. *J. Nucl. Med.* **2011**, *52* (5), 815.

(9) Duffy, D. C.; Mcdonald, J. C.; Schueller, O. J. A.; Whitesides, G. M. *Anal.Chem* **1998**, *70* (23), 4974.

(10) Di Carlo, D.; Wu, L. Y.; Lee, L. P. *Lab Chip* **2006**, *6* (11), 1445.

(11) Wheeler, A. R.; Throndset, W. R.; Whelan, R. J.; Leach, A. M.; Zare, R. N.; Liao, Y. H.; Farrell, K.; Manger, I. D.; Daridon, A. *Anal. Chem.* **2003**, *75* (14), 3581.

(12) van Staden, J. a; du Raan, H.; Lötter, M. G.; van Aswegen, A.; Herbst, C. P. *Phys. Med. Biol.* **2007**, *52*, N329.

(13) Nathanson, D. A.; Gini, B.; Mottahedeh, J.; Visnyei, K.; Koga, T.; Gomez, G.; Eskin, A.; Hwang, K.; Wang, J.; Masui, K.; Paucar, A.; Yang, H.; Ohashi, M.; Zhu, S.; Wykosky, J.; Reed, R.; Nelson, S. F.; Cloughesy, T. F.; James, C. D.; Rao, P. N.; Kornblum, H. I.; Heath, J. R.; Cavenee, W. K.; Furnari, F. B.; Mischel, P. S. *Science* **2014**, *343* (6166), 72.

(14) Deberardinis, R. J.; Thompson, C. B. *Cell* **2012**, *148* (6), 1132.

(15) Prior, J. O.; Montemurro, M.; Orcurto, M.-V.; Michielin, O.; Luthi, F.; Benhattar, J.; Guillou, L.; Elsig, V.; Stupp, R.; Delaloye, A. B.; Leyvraz, S. *J. Clin. Oncol.* **2008**, *27* (3), 439.

(16) Wang, C.; Guo, W.; Zhou, M.; Zhu, X.; Ji, D.; Li, W.; Liu, X.; Tao, Z.; Zhang, X.; Zhang, Y.; Li, J. *Clin. Cancer Res.* **2015**, *22* (7), 1603.

(17) Patel, A. P.; Tirosh, I.; Trombetta, J. J.; Shalek, A. K.; Gillespie, S. M.; Wakimoto,

H.; Cahill, D. P.; Nahed, B. V.; Curry, W. T.; Martuza, R. L.; Louis, D. N.; Rozenblatt-Rosen, O.; Suvà, M. L.; Regev, A.; Bernstein. E. B. *Science* **2014**, *344* (6190), 1396.

(18) Czernin, J. and Phelps, M. E. *Ann. Rev. Med.* **2002**, *53* (1), 89.

2.6 Appendix A: Supplementary figures
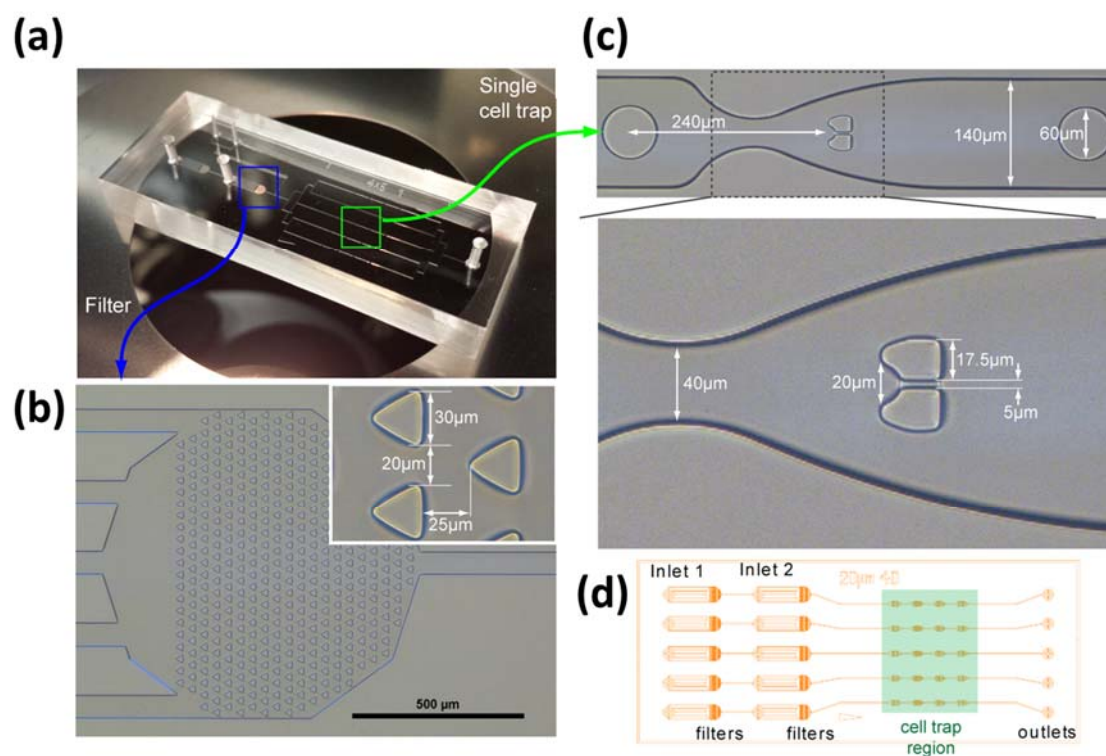
Figure 2.6 Betabox device image and dimensions. (a) Actual Betabox device image. (b) Image of the filter region and dimensions of key features. (c) Image of the single cell trap region with dimensions. (d) CAD image of the Betabox device with individually accessible channels.
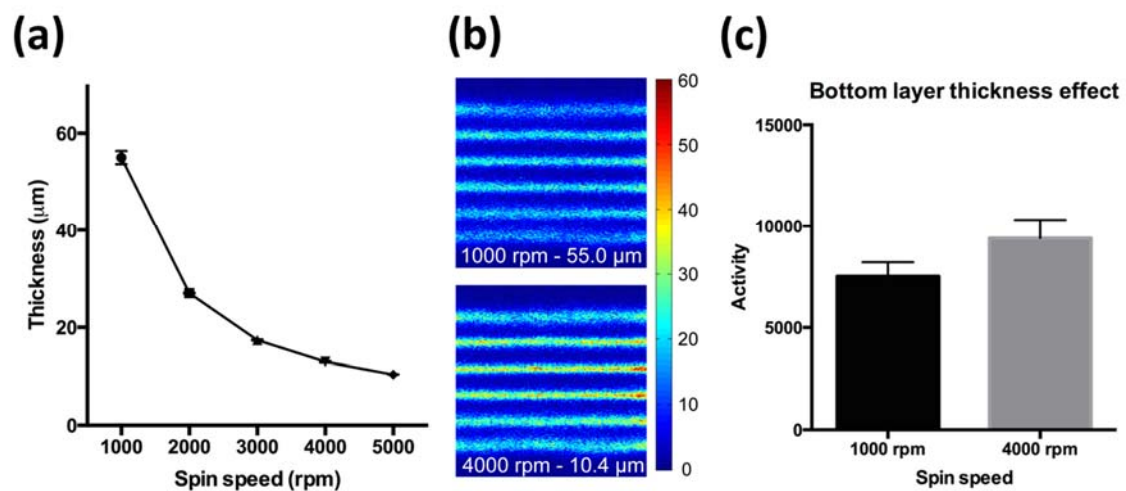
Figure 2.7 Bottom layer thickness effect to the sensitivity of the Betabox measurement. (a) Thickness of the PDMS layer with various spin speeds. (b) Image of the ^{18}F-FDG activity measured from the actual Betabox devices with two different bottom layer thickness: 13μm (4000 rpm) and 55μm (1000 rpm). All the channels are filled with ^{18}F-FDG solution with 3.7×10^7 Bq/ml of concentration. (c) Quantified activities from the images in (b). Signal is increased about 20% by using higher spin speed, 4000 rpm than 1000 rpm.

2.7 Appendix B: Supplementary tables

Table 2.1 The list of the media and the ingredients used.

Full Medium	
Ingredient (Manufacturer)	**Concentration**
Dulbecco's Modified Eagle Media Nutrient Mix F-12 (DMEM/F-12, Gibco®, Life Techonologies)	
GlutaMAX^{TM} (Gibco®, Life Techonologies)	1X
B27® Supplements (Gibco®, Life Techonologies)	1X
Heparin sodium salt from porcine intestinal mucosa (Sigma Aldrich)	1 µg/mL
Epidermal Growth Factor (EGF, Sigma Aldrich)	20 ng/mL
Fibroblast Growth Factor (FGF, Sigma Aldrich)	20 ng/mL
Penicillin-Streptomycin mix (Gibco®, Life Techonologies)	1X
Glucose Free Medium	
Ingredient (Manufacturer)	**Concentration**
Glucose free DMEM medium (Gibco®, Life Techonologies),	
GlutaMAX^{TM} (Gibco®, Life Techonologies)	1X
B27® Supplements (Gibco®, Life Techonologies)	1X
Sodium Pyruvate (Gibco®, Life Techonologies)	1X

Table 2.2 The average and the coefficient of variation (CV) of the actual signals from different chamber locations of the Betabox device.

4 by 5 chamber layout		5 by 6 chamber layout	
ROI ID	Total Activity	ROI ID	Total Activity
1	27754	1	23439
2	28000	2	25010
3	28381	3	24083
4	27299	4	24848
5	24602	5	24667
6	25910	6	21889
7	25762	7	25124
8	24746	8	23622
9	24940	9	24902
10	25458	10	22958
11	25784	11	20981
12	24417	12	24179
13	25786	13	23086
14	26060	14	24394
15	26850	15	22188
16	25142	16	21810
17	23959	17	24281
18	24469	18	23576
19	24048	19	25192
20	23503	20	22510
		21	20443
		22	23064
		23	23111
		24	23800
		25	22116
		26	21923
		27	22982
		28	21966
		29	23085
		30	22613
Average	25643.5	Average	23261.4
STDEV	1405.18	STDEV	1261.83
CV (%)	5.48	CV (%)	5.42

Chapter 3

Plasma proteomic measurement for monitoring and predicting glioblastoma patient responses to an anti-angiogenic drug treatment

3.1 Introduction

Quantifying patient tumor response during drug treatment is important in monitoring efficacy and resistance development during cancer therapy. Non-invasive imaging techniques, such as Magnetic Resonance Imaging (MRI), Computed Tomography (CT), and Positron Emission Tomography (PET), are well established for tracking physical sizes and metabolic activities of tumor during therapy.[1] However, imaging examinations usually require time intervals of at least one month because of both safety concerns and costs. This time interval is sometimes too broad to effectively monitor tumor responses and capture the initiation of drug resistance. Moreover, images are often poorly evaluated to detect tumor growth, which fails to capture the early drug resistance development. As a result, patients often receive treatments that are no longer effective to treat their tumors, yielding elevated risk and economic burdens.[2] Therefore, time intervals for monitoring tumor responses should be precisely and reasonably tuned depending on tumor types.

Glioblastoma multiforme (GBM), the most common type of brain tumor with a survival time of 12 - 15 months, is exemplary of a highly lethal tumor that needs response-

monitoring with fine time resolution. Contemporary therapeutic strategies for GBM are limited, thus leading to short survival time. For primary GBM patients, surgical resection is first executed and then combinatory therapy of radiotherapy and temozolomide treatment are administered for suppressing secondary tumors. However, some tumor cells remain after surgical resection, which forces clinicians to rely on targeted drug treatment despite the limited drug delivery capacity by the blood brain barrier. The high heterogeneity of GBM lowers the therapeutic efficacy of the drug and resistance subpopulations quickly proliferate. Once a patient develops a secondary tumor, clinical options become extremely limited. With only 3 FDA approved drugs for recurrent GBM, median survival times of recurrent GBM patients reduces to 8-10 months.[3–5]

This study focuses on the clinical case of the bevacizumab treatment, an anti-angiogenic drug, in a group of recurrent GBM patients. Bevacizumab is a humanized monoclonal antibody targeting vascular endothelial growth factor (VEGF).[6] The rationale for this targeted therapy is based on the observation that tumor cells induce surrounding endothelial cells to develop bulky vascular structures in order to increase nutrient supplies. Cancer cells secret VEGF which stimulates the vessel formation of endothelial cells via receptor tyrosine kinases (RTKs) signaling. Bevacizumab depletes available VEGF proteins in tumor microenvironment and hence inhibits the vessel formation. In 2009, FDA approved this drug for treating recurrent GBM after a clinical trial.[7] However, subsequent clinical trials have not successfully shown prolonged overall survival, and only a small subset of the recurrent GBM patients benefited.[5]

We hypothesize that a panel of plasma protein markers can be employed for monitoring patient therapeutic responses to the bevacizumab treatment. Above all, blood contains rich biological information such as DNA, RNA, proteins, and circulating tumor cells associated with tumor proliferation and drug response.[8,9] Blood sampling is also minimally invasive and thus can be frequently executed. Among those tumor relevant biomarkers, proteins are particularly useful in that their functions are clearly understood, and we might be able to characterize what functional changes occur during therapy. In the context of cancer biology, unique proteomic signatures associated with drug resistance might guide us to define the next drug targets. However, single plasma protein biomarkers have shown limited diagnostic power, and only 2 markers, CA-125 for ovarian cancer and PSA for prostate cancer, were approved by FDA for diagnosing tumor status. Instead, proteomic classifiers, defined as a function of multiple selected protein markers, have been developed and evaluated for cancer diagnosis with the aid of the technological development in proteomics tools in mass spectrometry and immunoassays.[10–12] For example, OVA1, composed of 5 marker proteins including CA-125, displayed higher predictive capacity in ovarian cancer diagnosis than a sole maker of CA-125.

For this work, patient proteome profiling was performed by multiplexed, sandwich immuno-fluorescence assays on a microchip.[13,14] This technology has two components: a DNA barcode chip and a DNA-encoded antibody library (DEAL) (Figure 3.2). First, up to 20 orthogonal single-stranded DNA (ssDNA) oligomers were flow-patterned in parallel within 50 μm channels on a microscope glass slide. This process was engineered for the mass production over 20 DNA barcode chips. Second, DEAL was prepared by conjugating capture antibodies with ssDNA oligomers complementary to barcode DNAs. Then, 16

individual assays of finger-prick volume (30 µL) were simultaneously performed on the barcoded glass surface. An array of ssDNA oligomers is converted into an array of antibodies by hybridizing the DNA patterns with the DEAL antibody conjugates, and the locations of antibody conjugates are designated by their DNA sequences. Then, serum samples and fluorescence labeled detection antibodies are sequentially loaded. The glass slide is finally scanned, and the collected fluorescence signals are digitized for quantitation. Fluorescence intensity can be converted into absolute quantity (ng/mL) with calibration curves from recombinant proteins.

We first identified 14 serum protein markers for diagnosing GBM tumor responses to the bevacizumab treatment. From an initial pool of 62 patient samples, 35 plasma proteins were measured, and tumor responses associated with each sample were clinically evaluated as binary variables.[15] We then found 14 proteins with the high classification capacity of patient treatment responses among 35 proteins by developing a multivariate statistical model. We sought to validate our model to a larger group of samples in order to evaluate those 14 serum proteins as the predictive markers of the drug responses. Thus, we measured 14 proteins in 516 serum samples from 105 GBM patients who were receiving the treatment. We sought a robust model of the drug responses as a function of serum proteins, so that the drug efficacy and its resistance development can be readily assessed.

Furthermore, the longitudinal changes of patient tumor volumes were quantitatively assessed by analysis of functional neuroimages (AFNI) software.[5,16,17] This approach can quantitatively track the volumetric changes of tumor during treatment and resolve the qualitative assessment of tumor responses, which cause inaccurate diagnostics.[18] To test

this idea, we chose a group of patients who first responded to the drug but later showed drug resistance during blood sampling periods. Using the AFNI software, we obtained contrast material-enhanced T1 weighted subtraction maps from those patients' MRI scan data and estimated tumor volumes in mm^3 scale. We then generated a mathematical model combining plasma proteomic signatures with tumor volumes to predict tumor drug responses.

3.2 Materials and methods

3.2.1 Study design

Plasma samples were collected from 105 primary or recurrent GBM patients who were treated with bevacizumab as a part of the standard care. Plasma sampling periods mostly included before, during, and after the bevacizumab treatment. Drug doses varied depending on patients. Majority of patients had received the standard radiation therapy before the bevacizumab treatment. More patient clinical characteristics can be found in Table 3.1, Appendix A.

3.2.2 Plasma collection and processing

Patient blood samples were collected and processed by standard phlebotomy procedures. 10mL of blood drawn from a patient was first collected in a tube containing anti-coagulant (BD Vacutainer Yellow Acid-citrate-dextrose (ACD) Blood Collection Tubes). Tubes were centrifuges at 1500×g in a refrigerated centrifuge (3-5°C). ~200μL Plasma samples were aliquoted into cryogenic vials and stored at -80°C. Samples were

processed within 2 hours of blood draw. The aliquoted samples were thawed and used only once for the multiplexed sandwich immunofluorescence assay.

3.2.3 DNA-barcode chip fabrication and DNA-encoded antibody library (DEAL) preparation

Methods for DNA-Encoded Antibody Library (DEAL) preparation, DNA barcode patterning, and PDMS microwell slab fabrication were previously described.[14,19] Lists of DNA sequences and antibodies are summarized in Appendix A, Table 3.2 and 3.3.

3.2.3.1 DNA-patterning on a glass slide

A mold of 50 μm wide and 40 μm high patterns was first prepared with SU8 2025 (Microchem) by the standard photolithography. Mold surface was treated with trimethylchlorosilane (TMCS, Sigma Aldrich). Sylgard 184 (Dow Corning) was mixed (pre-polymer : curing agent = 10:1), degassed, poured on the mold, and cured at 80°C for 2 hours. Cured PDMS slab was cut, peeled from the mold, inlet and outlet punched, and aligned with a poly-L-lysine (PLL) coated glass slide (Thermo Scientific). The aligned PDMS slab and PLL glass slide were bonded at 80°C for 2 hours. 15 channels were used in this study. After bonding, 0.1% PLL solution (Sigma Aldrich) was flown through the channel and dried overnight by air flow overnight, using solution loading devices. Details about the solution loading devices can be found in chapter 5 of this thesis. Then, DNA solution of single stranded DNA (ssDNA) oligo B-Q (Bioneer, Inc) was loaded in the PLL-deposited channel by airflow, using the solution loading devices (Table 3.2, Appendix A). Dimethyl sulfoxide (DMSO, American Type Culture Collection) phosphate buffered saline (PBS) at pH 7.4 (Corning) were used for preparing ssDNA solution. The ssDNA solution

was dissolved in DMSO/PBS (2:3) solution, and mixed with BS3 (bis(sulfosuccinimidyl)suberate), ThermoFisher Scientific) linker solution in PBS. This DNA-solution filled PDMS-glass assembly was incubated at incubated at room temperature for 2 hours in a humidifier chamber. The PDMS slab was peeled off after the incubation, and the DNA patterned glass slide was washed with 0.02% SDS once and Millipore water three times sequentially. The glass slide was spin-dried with a Miniarray microcentrifuge (VWR). A region of DNA pattern near one edge of the glass slide were incubated with Cy3-complemenaty ssDNA solution (Integrated DNA Technologies) in 1% BSA in PBS at 37°C for 1 hour for the DNA pattern quality assessment. The region was scanned with Axon GenePix 4400A (532nm at PMT 450, laser power 15%, 10μm/pixel), and the fluorescence intensity was measured.

3.2.3.2 DNA-antibody conjugation

Anti-streptavidin mouse monoclonal antibody was first reconstituted in PBS and desalted using a Zeba (ThermoFisher Scientific) spin column (Table 3.3, Appendix A). Succinimidyl 4-hydrazinonicotinate acetone hydrazine (S-HyNic, Solulink) in anhydrous N,N-dimtheylformamide (DMF, Solulink) solution was added to the antibody solution and incubated at room temperature for 2 hours. In parallel, ssDNA oligo B'-Q' (Bioneer, Inc) was dissolved in PBS and mixed with S-4FB in DMF solution (Table 3.2, Appendix A). The mixture was incubated at room temperature for 2 hours. Each reaction mixture was buffer exchanged into a pH 6.0 citrate buffer using Zeba spin columns. These buffer-exchanged solutions were combined, and incubated at room temperature for 2 hours and then at 4°C overnight. The DNA-antibody conjugate was purified by FPLC (GE,

Pharmacia Superdex 200 gel filtration column), and the purified conjugate was concentrated by a centrifugation (Millipore, Amicon Ultra-4, MWCO 10kDa).

3.2.3.3 Multiplexed sandwich immunofluorescence assays for protein measurements

1) *Microarray preparation.* A 16 microwell PDMS slab and a DNA-patterned glass slide were first aligned. The DNA-antibody conjugate was prepared in the BSA solution (1% in PBS) was pipetted in each microwell and incubated at 37°C for 1 hour in order to hybridize ssDNA on the glass with the antibody conjugates. Surface was washed with 1X PBST. Additional surface blocking was done with BSA solution (1% in PBS) at 37°C for 1 hour.

2) *Patient serum sample loading.* Patient serum samples were thawed and centrifuged at $21130 \times g$ for 5 mins. Supernant was added to the microwells and incubated at room temperature with gentle shaking for 1 hour. After the incubation, the surface was washed with 1× PBST.

3) *Detection antibody loading.* Detection antibody cocktail solution was prepared in the BSA solution (1% in PBS) and pipetted in the each microwell. It was incubated at room temperature for 1 hour. Surface was washed with 1X PBST. Streptavidin-Alexa Fluor 647 conjugate solution was prepared in the BSA solution (1% in PBS), and the same procedures were performed as the detection antibody solution during loading, incubating, and washing.

4) *Fluorescence readout.* The 16 well PDMS was peeled off, and the microarray slide is washed with 1X PBS, 0.5X PBS, and Millipore water sequentially. The microarray slide was spin-dried with the miniarray microcentrifuge. The slide is scanned by an Axon GenePix 4400A (635nm: PMT 600, laser power 80%, 10μm/pixel and 532nm: PMT 450,

laser power 10%, 10µm/pixel). The scanned image was digitized, and fluorescence signal intensities were extracted using the manufacturer's software.

3.2.4 Clinical data acquisition

Patient tumor progression was monitored by magnetic resonance imaging (MRI). Details of MRI scan conditions can be found in reference 5.[5] Clinicians interpreted MRI data and assign categorical variables for the tumor progression. Values are 0 for responders (stable disease, i.e. the drug responsive period of responders) and 1 for non-responders (progressive disease, i.e. the non-responsive period of responders and all the treatment cycles of non-responders). These binary values were linked to the measured 14 plasma protein levels.

3.2.5 Analysis of functional image analysis

AFNI was performed for the MRI scan data from 23 patients as previously described.[16,17] Tumor volumes were estimated using this software. If MRI data on the exact plasma sampling date were available, estimated tumor volumes were accepted as they were. If MRI data were not available on the same plasma sampling dates, the range of tumor volume was estimated with the 2 MRI scan data closest to the sampling date (maximum ± 1 month). Then, assuming a constant change rate of tumor volumes between those 2 time points, tumor volumes on the sampling date were estimated.

3.2.6 Statistical analysis

Pairwise comparison of protein levels in two groups (tumor growth vs. no growth) was performed by two-tailed Mann-Whitney test. Spearman's rank method was used for

obtaining correlation coefficients between protein levels and tumor sizes. Only the coefficients, with Bonferroni-corrected statistical significance, were summarized in Appendix A, Table 3.8.

3.2.7 Data analysis

All the statistical analysis was performed with XLSTAT (Addinsoft) software. We screened the most predictive markers of GBM patient responses to the bevacizumab treatment by partial least square discriminant analysis (PLS-DA).[20–22] We used a data set of 62 patient samples with 35 measured protein levels, and this data set was obtained from a previous study.[15] Both raw and feature scaled protein levels were separately tested with PLS-DA. Variable importance in the projection (VIP), calculated by the software, was used as the measure of the predictive capacity of individual protein markers. More detailed description of PLS-DA can be found in chapter 4 of this thesis. 14 proteins with the highest VIP were selected to the follow-up measurement of 516 samples from 105 GBM patients. The data set of 14 protein levels and the GBM patient responses was analyzed by principal component analysis logistic regression method.[23] Here in this modeling, the used protein levels were either raw or normalized with the estimated tumor volumes. A logistic regression was separately performed for the modeling of estimated tumor volumes and GBM patient responses.

3.3 Results and discussion
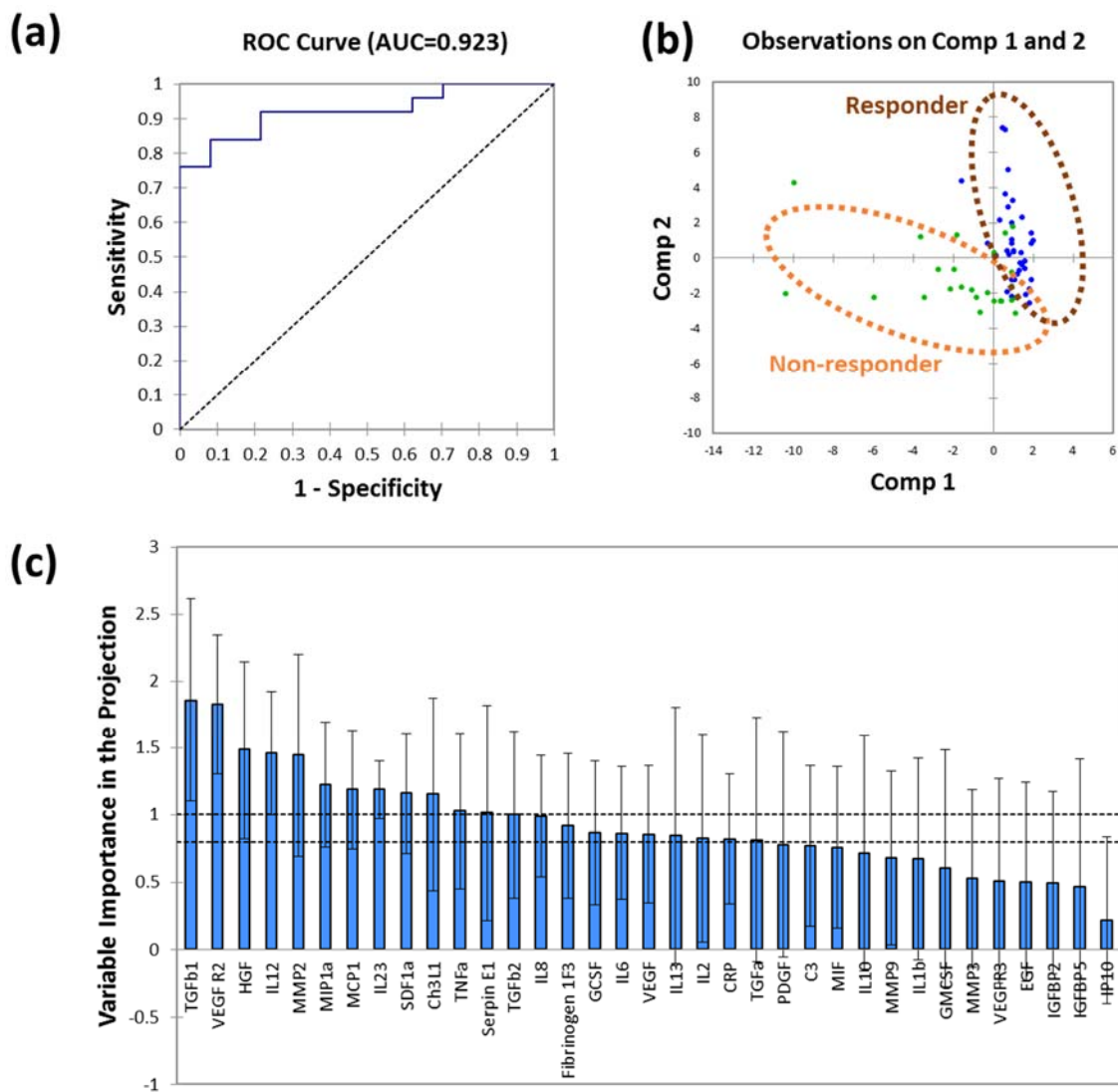
Figure 3.1 PLS-DA modeling of the 35-plex proteome data of 62 samples. Raw protein levels were used here. (a) Receiver operating characteristic curve of the model with the area under the curve of 0.923. (b) Projection of the data points onto 2 components of the fitted model. (c) Variance importance in the projection of the 35 protein markers. 95% confidence interval shown as the bars.

PLS-DA models of patient responses and 35-plex proteome were fitted in two data sets: raw protein levels and feature scaled protein levels (Figure 3.1 and Figure 3.9, Appendix B). The fitted models showed robust classification capacity with the area under

the curve (AUC) of 0.923 (raw protein levels, Figure 3.1a) and 0.914 (normalized protein levels, Figure 3.9a in Appendix B). Proteomics data points, projected onto two components from original 35 dimensional spaces, were well-separated, which confirmed the robust classification capacity (Figure 3.1b and Figure 3.9b, Appendix B). In each data set, we obtained classification functions of responders and non-responders (Table 3.4 and 3.6, Appendix A) and VIP of all the 35 protein markers (Figure 3.1c, Figure 3.9c, Table 3.5, and Table 3.7, Appendices A and B).

Total 14 protein markers among 35 protein markers were selected from the two fitted PLS-DA models. Since VIP is the measure of predictive capacity of individual markers, we looked at protein markers with top 12 greatest VIP values in each model. 10 proteins were shown in common, 1) growth factors and receptor proteins such as transforming growth factor β1 (TGF β1), hepatocyte growth factor (HGF), vascular endothelial growth factor receptor 2 (VEGF R2), 2) cytokines such as interleukin(IL)-12, IL-23, macrophage inflammatory protein-1 α (MIP-1α, i.e. CCL3), monocyte chemotactic protein 1 (MCP-1, i.e. CCL2), and 3) enzymes such as matrix metalloproteinase-2 (MMP-2), plasminogen activator inhibitor (Serpin E1), chitinase-3-like protein 1 (Ch3L1). Additionally, IL-13 and IL-10 were found from the raw protein level model, and stromal cell-derived factor 1α (SDF-1α, i.e. C-X-C motif chemokine 12) and tumor necrosis factor α (TNFα) were from the feature scaled protein level model. A total of 14 proteins, combined from those top 12 predictive markers in each PLS-DA model, were selected as the protein panel for the sandwich-type immunofluorescence assay. These screened protein markers are highly related, implying the multi-collinearity between them (Figure 3.10).
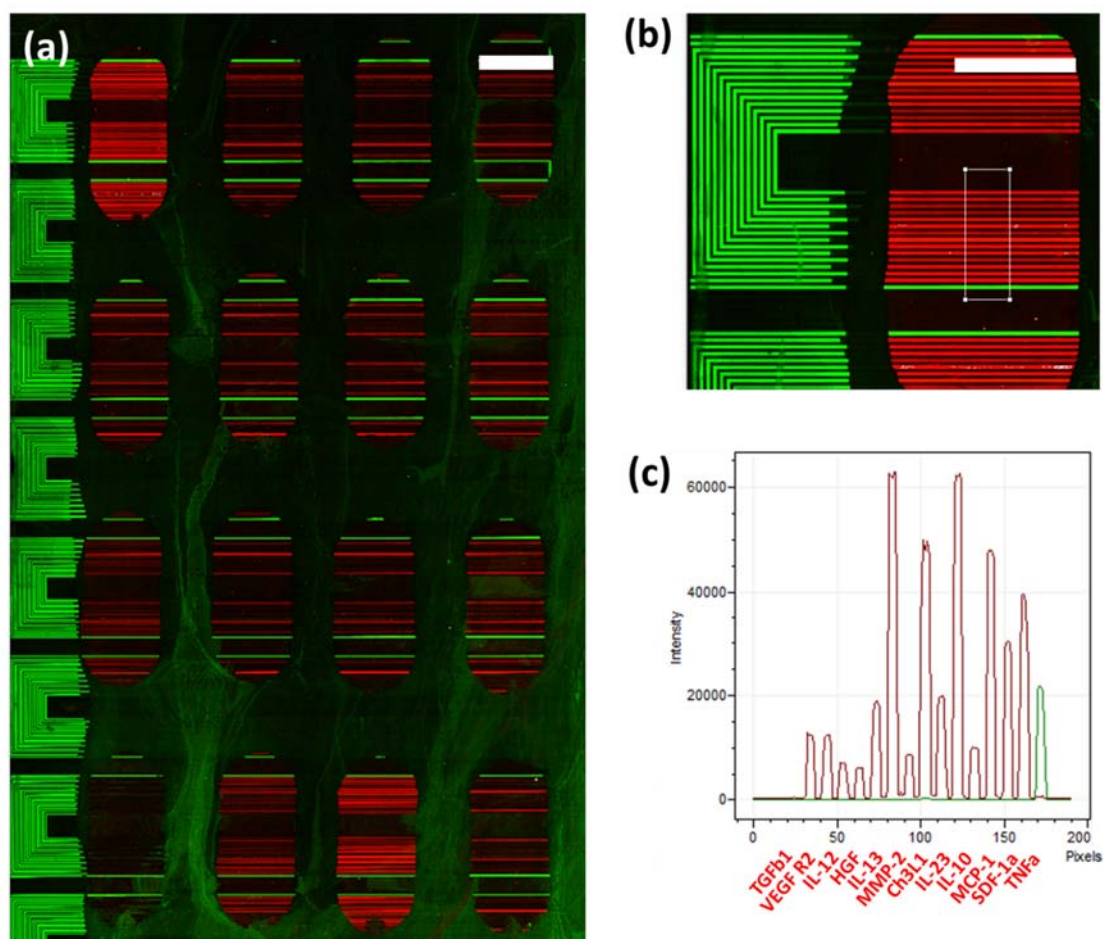
Figure 3.2 Raw scan image. (a) Raw scan of a barcode chip after the 14-plex plasma proteomic measurement. Total 16 plasma samples were measured (scale bar: 3mm). (b) A single well magnified in the raw scan. Each well contains 2 sets of antibody arrays for the 14-plex sandwich-type immunofluorescence assays. Cy3 fluorescence, shown as a green stripe, indicated the spatial location of other barcode stripes which identified analytes. Fluorescence intensities were digitized from a line scan, shown as a white box (scale bar: 1.5mm). (c) Digitization results. A red graph represented signals from the immunofluorescence assays and a green graph were from the location indicator of Cy3 fluorescence. Identities of each analyte were labeled.

We then sought to validate the classification capacity of this screened protein panel to diagnose the drug responses of a large pool of patient samples. DEAL conjugates and DNA barcode chips were prepared, validated, and calibrated as previously described (Figure 3.2 and Figure 3.11, Appendix B).[13,14] We performed the 14-plex proteomic measurement of total 516 samples from 105 patients in this study, and relevant clinical data

were also obtained (Figure 3.3). This raw data set was divided into several sub-data sets

depending on blood sample dates (before, during, after the bevacizumab treatment) and

drug responses (responder and non-responder). However, none of the 14 protein levels

were significantly different from responders and non-responders during the bevacizumab

treatment in this large sample pool of 350 samples (Figure 3.4).
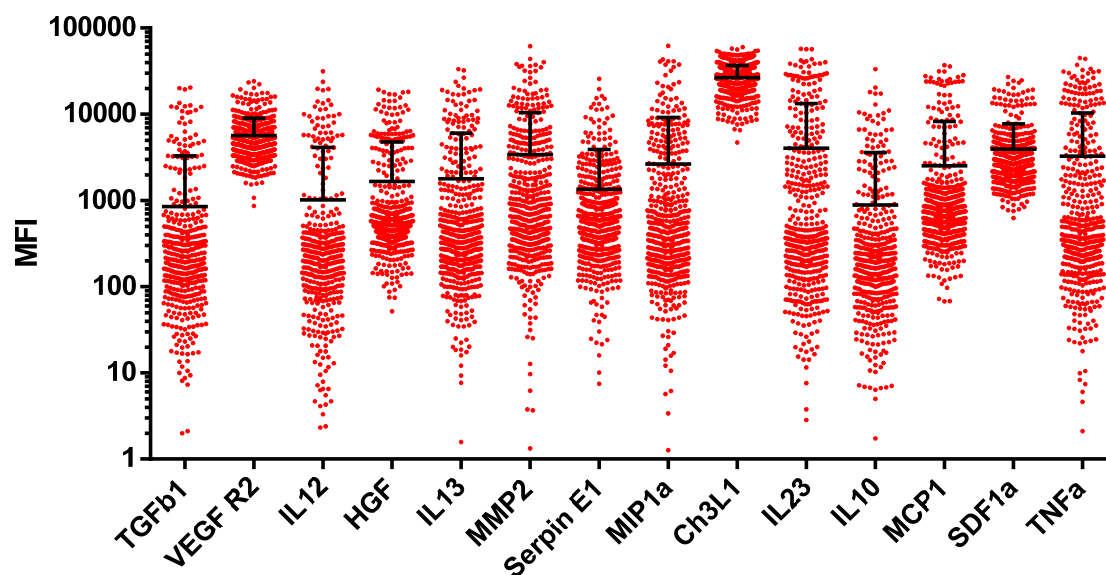
Figure 3.3 Raw protein levels from the 14-plex proteomic measurement. Total 516 samples from 105 GBM patients were measured including before, during, and after the bevacizumab treatment. Averages and standard deviations of the measured 14 proteins were shown.

We hypothesize that the qualitative assessment of patient drug responses, e.g.

scores, might cause the inaccurate classification of drug responses. The assessment is

typically performed by clinicians, as longitudinal comparison of patient MRI scan data sets

at several time points. This method intrinsically accompanies the variations between

clinicians who evaluate the drug responses, and clinical interpretation is often challenging

for some MRI scan data sets.[18] Therefore, these issues may contribute to the lack of difference in the blood signatures of responders and non-responders.
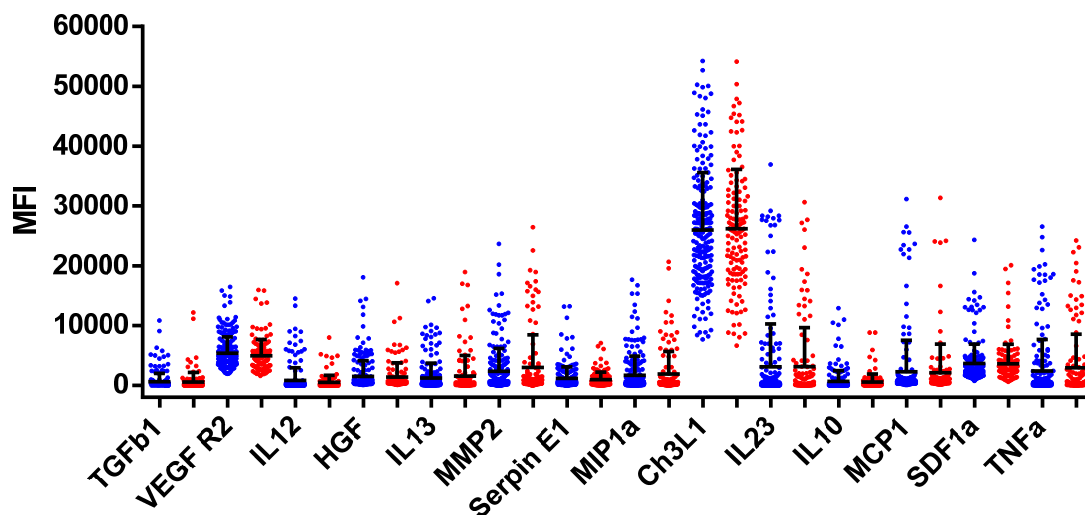
Figure 3.4 Raw protein levels in the 350 samples collected from GBM patients during the bevacizumab treatment. Blue (n=221) were responders and red (n=129) were non-responders. No protein levels were significantly different between responders and non-responders. Averages and standard deviations were shown.

AFNI is an alternative option to quantitatively assessing patient drug responses, thereby resolving the issues in the clinical evaluations (Figure 3.5 and Figure 3.12, Appendix B).[16,17] This open-source software provides tools for processing and analyzing the MRI scan data, and have two key features to estimate tumor volumes. First, this software provides the subtraction function between MRI data from different conditions, for precisely defining tumor lesion (Figure 3.5a – 3.5c). Since MRI contrast agents are designed to specifically target tumor, and the contrast material-enhanced region in the scan images is tumor lesion. In the manner of background subtraction, only the tumor lesion can be selectively highlighted by subtracting T1 weighted MRI scans (background) and

contrast material-enhanced T1 weighted MRI scans (signal). It is very useful function because a user does not need to compare two separate MRI data sets for finding tumor legions anymore. Also, it basically reduces human error and variations in the clinical interpretation of the challenging data sets. Second, this software supports tools to draw region of interest (ROI) on the scan images for estimating tumor volumes (Figure 3.5d and Figure 3.12a, Appendix B). Depending on the scan conditions, this software calculates the mm^3 volume per pixel of a scan image and estimates the volume of ROI. Thus, patient tumor volumes can be acquired by integrating the estimated ROI volumes in individual scan images in a MRI data set (Figure 3.12b, Appendix B).

For AFNI, we categorized GBM patient groups depending on drug responses. Based on medical history and sampling dates, we could divide the 105 patients into 3 subgroups: patients who were 1) responsive early but non-responsive later, 2) responsive all the time, and 3) non-responsive all the time. Since the AFNI requires high labor input, we decided focused on the first subgroup (subgroup 1) and estimated 128 tumor volumes. We looked at correlations between individual protein levels and estimated tumor volumes (Table 3.8, Appendix A). There were no significant correlations found, and no protein markers in our panel could be directly used for getting tumor volumes. We also looked at correlations of tumor volume changes vs. protein marker levels / protein marker level changes, but no correlations were found (data not shown).
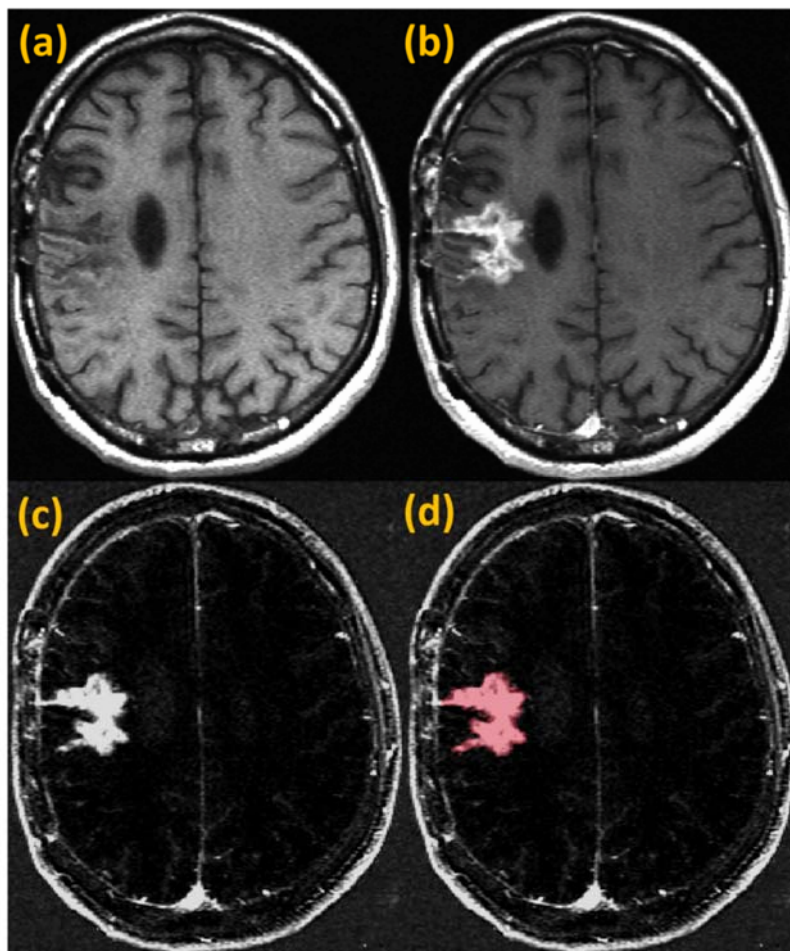
Figure 3.5 Analysis of functional neuroimages (AFNI). (a) T1 weighted MRI scan image. (b) Contrast material-enhanced T1 weighted MRI scan image at the same location of (a). (c) Image subtraction between (a) and (b). Only the enhanced region visualized and highlighted a tumor lesion. (d) Selected ROI for the volume estimation with the AFNI program. Each pixel in an image has a designated volume depending on MRI scan conditions. Multiple MRI scans will be integrated into tumor volumes (mm^3).

Next, we investigated if the estimated tumor volumes can be used for normalizing measured protein levels and thus improving the drug response classification via plasma proteomic signatures (Figure 3.6). The idea was essentially to resolve the inter- and intra-patient variability existing in patient blood. In other words, plasma protein levels vary not only among patients in the same drug response status but also among different time points

of a same patient. Since we did not know an internal standard for quantitatively assessing such biological noises during the drug treatment, we hypothesized that tumor volumes could be used instead. This hypothesis surprisingly worked well for the subgroup 1, making all the normalized protein levels in the drug responses significantly different.
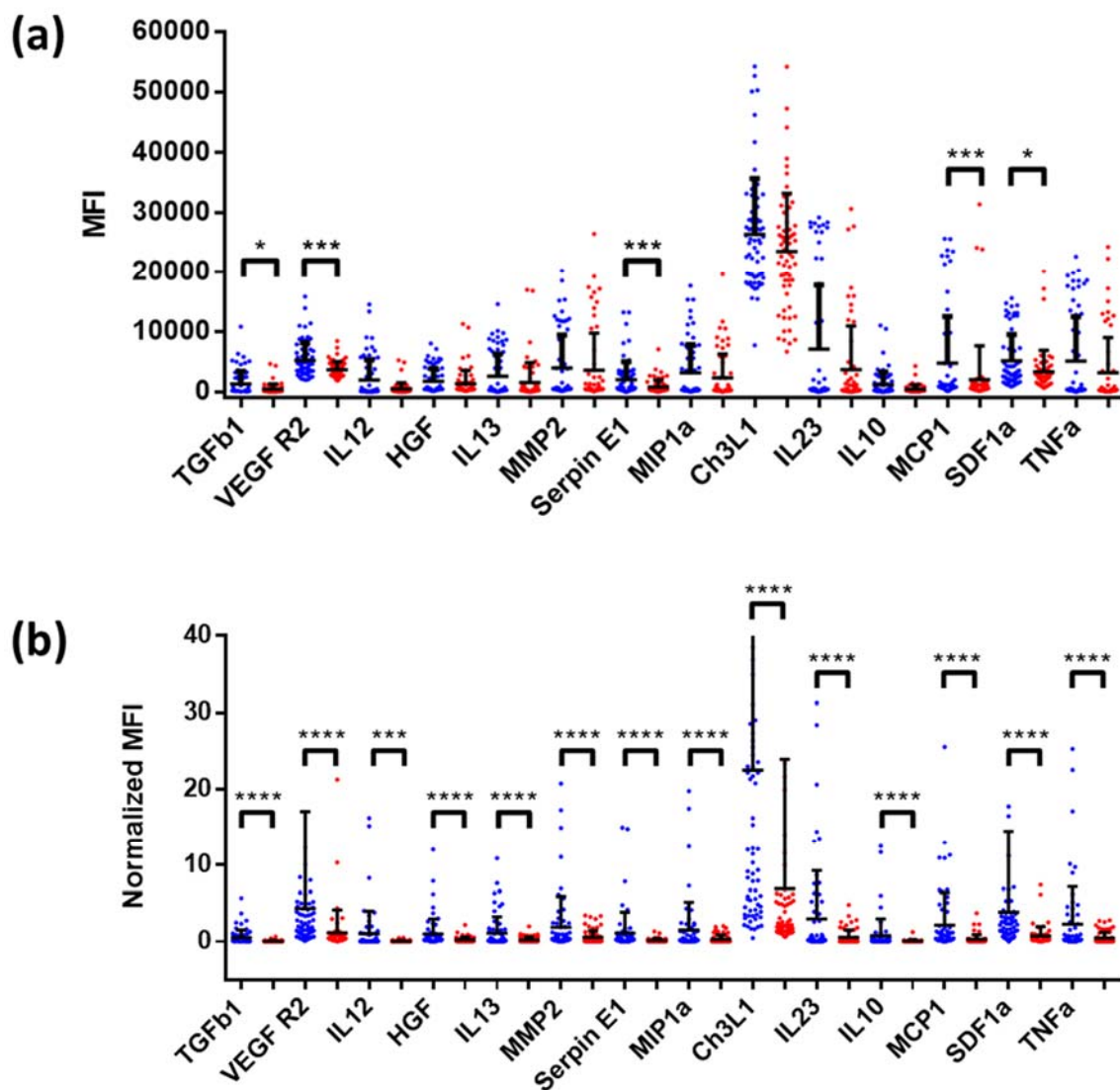
Figure 3.6 Subgroup 1 data with or without normalization to estimated tumor volumes (n=128). (a) Raw protein levels between responders (blue, n=66) and non-responders (red, n=62). (b) Normalized protein levels. (*, p<0.05; **, p<0.005; ***, p<0.0005; ****, p<0.0001). Averages and standard deviations were shown.

We further generated a model to link the normalized protein levels and drug responses in the patient subgroup 1, using the PCA logistic regression method. We randomly split the entire data set into a training set (103 samples) and a prediction set (25 samples). Then we make a model based on the training set and apply the fitted model to the prediction set. The accuracy of the model in the prediction set basically represents the quality of model. We repeated 5 iterations of this modeling work and calculated average. First of all, we compared diagnostic capacity of the fitted models in the training set in Figure 3.7. As expected, the model with the normalized protein levels showed the highest AUC value (Figure 3.7a), although either raw protein levels or tumor volumes also showed moderate AUC values (Figure 3.7b and 3.7c). We also applied the same modeling method to the entire raw protein level data set of all the patient subgroups (n=350), the trained model had relatively poorer capacity (Figure 3.7d). Confusion matrices and parameters of the models in Figure 3.7 can be found in Table 3.9-3.20, Appendix A.

Model validation results are summarized in Figure 3.8. We calculated the model accuracy from the obtained confusion matrices (Figure 3.8a and b, confusion matrices from the additional 4 iterations were not shown). The model with the normalized protein levels showed $83.8 \pm 2.66\%$ (the training set) and $73.5 \pm 7.18\%$ (the prediction set), whereas other models with either raw protein levels or tumor volume had lower accuracies (raw protein level model: 71.1 ± 3.39 % in the training set and 66.4 ± 7.20 % in the prediction set; tumor volume model: 67.4 ± 2.23 % in the training set and 64.0 ± 8.49 % in the prediction set). AUC values in the training set were 0.907 ± 0.0190, 0.804 ± 0.0377, and 0.766 ± 0.0341 respectively, and the normalized protein level showed the highest values (Figure 3.8c). Again, this modeling method was applied to the entire raw protein level data set, we

obtained 68.4 ± 0.824 % accuracy in the training set, 65.4 ± 3.41 % accuracy in the prediction set, and AUC of 0.687 ± 0.0183. All of these findings propose that the protein levels normalized to tumor volumes should be used for developing the classifiers which can the best predict the drug responses of GBM patients in the bevacizumab treatment.
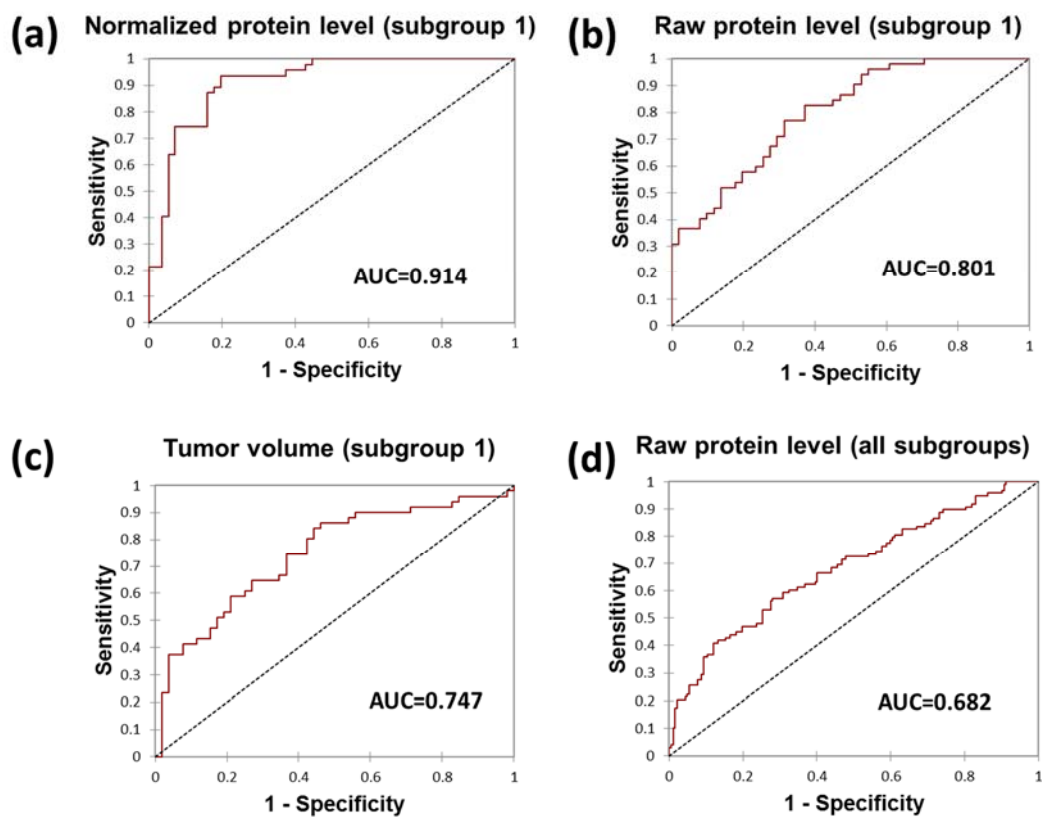
Figure 3.7 Receiver operating characteristic of the developed models in the training sets (one of 5 iterations, closest to the average). (a) Subgroup 1 with normalized protein levels. (b) Subgroup 1 with raw protein levels. (c) Subgroup 1 with estimated tumor volumes only. (d) All subgroups with raw protein levels.
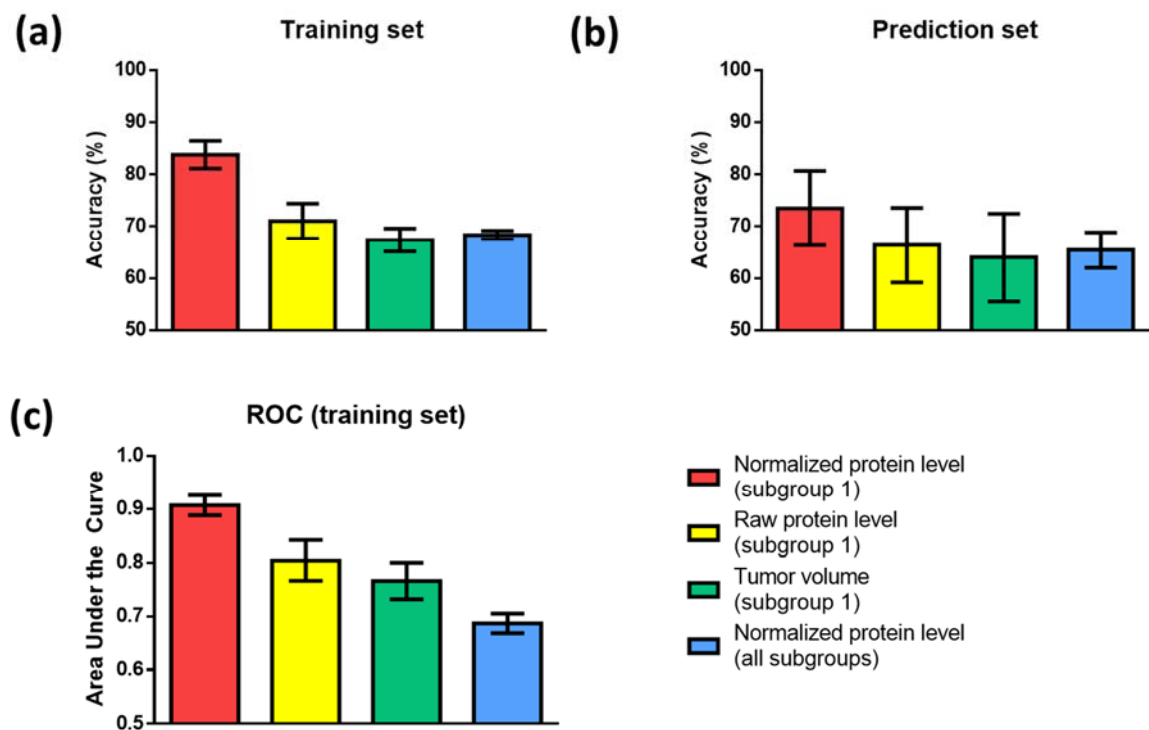
Figure 3.8 Summary of the model evaluation. (a) Model accuracy in the training data sets. (b) Model accuracy in the prediction data sets. (c) Area under the curves in the training data sets. Averages and standard deviations were shown.

3.4 Conclusion

Here we have demonstrated the miniaturized and multiplexed immunofluorescence assay platform as a proteomics tool. We investigated the plasma proteomic signatures of GBM patients associated with the drug responses to the bevacizumab treatment. 14 the most predictive protein markers were screened from 35 proteins of 62 patient samples measured in a previous study. Then, those 14 protein levels in a large panel of 516 patient plasma samples were measured. Measured protein levels from the 350 patient samples during the bevacizumab treatment were associated with the drug responses, and the developed model had a moderate prediction accuracy of $65.4 \pm 3.41\%$. In order to develop

a diagnostic model with a higher prediction capacity, tumor volumes of a patient subgroup (n=128) were quantitatively estimated from patient MRI scans by the computational image analysis tool. Although no single protein markers were significantly correlated with the tumor volume, all of these quantities, taken together, yielded a powerful diagnostic model with the prediction accuracy of 73.5 ± 7.18%. This approach can be expanded to the rest of patient subgroups.

The general workflow of this approach can be readily implemented in clinical settings. The modular design of these devices enables barcodes to bear virtually any panel of antibodies. Thus, the multiplexed measurement of biomarkers is straightforward for any disease. Moreover, their bulk fabrication reduces cost and increases the throughput at which diagnoses are made. Because of our small sample chambers, these devices inherently require finger-prick volumes of blood, drastically improving patient compliance. As a result, this platform is well-suited for the future integration into routine tumor drug response monitoring.

3.5 References

(1)   Kim, M. M.; Parolia, A.; Dunphy, M. P.; Venneti, S. *Nat. Rev. Clin. Oncol.* **2016**, *13* (12), 725.

(2)   Prasad, V.; De Jesus, K.; Mailankody, S. *Nat. Rev. Clin. Oncol.* **2017**, *14* (6), 381.

(3)   Cloughesy, T. F.; Cavenee, W. K.; Mischel, P. S. *Annu. Rev. Pathol. Mech. Dis.* **2014**, *9* (1), 1.

(4)   Prados, M. D.; Byron, S. A.; Tran, N. L.; Phillips, J. J.; Molinaro, A. M.; Ligon, K. L.; Wen, P. Y.; Kuhn, J. G.; Mellinghoff, I. K.; De Groot, J. F.; Colman, H.; Cloughesy, T. F.; Chang, S. M.; Ryken, T. C.; Tembe, W. D.; Kiefer, J. A.; Berens, M. E.; Craig, D. W.; Carpten, J. D.; Trent, J. M. *Neuro. Oncol.* **2015**, *17* (8), 1051.

(5)   Ellingson, B. M.; Gerstner, E. R.; Smits, M.; Huang, R. Y.; Colen, R.; Abrey, L. E.; Aftab, D. T.; Schwab, G. M.; Hessel, C.; Harris, R. J.; Chakhoyan, A.; Gahrmann, R.; Pope, W. B.; Leu, K.; Raymond, C.; Woodworth, D. C.; de Groot, J.; Wen, P. Y.; Batchelor, T. T.; van den Bent, M. J.; Cloughesy, T. F. *Clin. Cancer Res.* **2017**, Epub ahead of print (doi: 10.1158/1078-0432.CCR-16-2844).

(6)   Ferrara, N.; Hillan, K. J.; Gerber, H.-P.; Novotny, W. *Nat. Rev. Drug Discov.* **2004**, *3* (5), 391.

(7)   Cohen, M. H.; Shen, Y. L.; Keegan, P.; Pazdur, R. *Oncologist* **2009**, *14*, 1131.

(8)   Westphal, M.; Lamszus, K. *Nat. Rev. Neurol.* **2015**, *11* (10), 556.

(9)   Siravegna, G.; Marsoni, S.; Siena, S.; Bardelli, A. *Nat. Rev. Clin. Oncol.* **2017**.

(10)   Wulfkuhle, J. D.; Liotta, L. a; Petricoin, E. F. *Nat. Rev. Cancer* **2003**, *3* (4), 267.

(11)   Li, X.; Hayward, C.; Fong, P.-Y.; Dominguez, M.; Hunsucker, S. W.; Lee, L. W.; McLean, M.; Law, S.; Butler, H.; Schirm, M.; Gingras, O.; Lamontagne, J.; Allard, R.; Chelsky, D.; Price, N. D.; Lam, S.; Massion, P. P.; Pass, H.; Rom, W. N.; Vachani, A.; Fang, K. C.; Hood, L.; Kearney, P. *Sci. Transl. Med.* **2013**, *5* (207), 207ra142.

(12)   Borrebaeck, C. A. K. *Nat. Rev. Cancer* **2017**, *17* (3), 199.

(13)   Fan, R.; Vermesh, O.; Srivastava, A.; Yen, B. K. H.; Qin, L.; Ahmad, H.; Kwong, G. a; Liu, C.-C.; Gould, J.; Hood, L.; Heath, J. R. *Nat. Biotechnol.* **2008**, *26* (12), 1373.

(14)   Xue, M.; Wei, W.; Su, Y.; Kim, J.; Shin, Y. S.; Mai, W. X.; Nathanson, D. A.; Heath, J. R. *J. Am. Chem. Soc.* **2015**, *137* (12), 4066.

(15)   Vermesh,   O.   **2011**,   http://resolver.caltech.edu/CaltechTHESIS:04272011-115528661

(16)   Cox, R. W. *Comput. Biomed. Res.* **1996**, *29*, 162.

(17)   Ellingson, B. M.; Kim, H. J.; Woodworth, D. C.; Pope, W. B.; Cloughesy, J. N.; Harris, R. J.; Lai, A.; Nghiemphu, P. L.; Cloughesy, T. F. *Radiology* **2014**, *271* (1), 200.

(18)   Chinot, O. L.; Macdonald, D. R.; Abrey, L. E.; Zahlmann, G.; Kerloëguen, Y.; Cloughesy, T. F. *Curr. Neurol. Neurosci. Rep.* **2013**, *13* (5), 347.

(19)   Shi, Q.; Qin, L.; Wei, W.; Geng, F.; Fan, R.; Shik Shin, Y.; Guo, D.; Hood, L.; Mischel, P. S.; Heath, J. R. *Proc. Natl. Acad. Sci.* **2012**, *109* (2), 419.

(20)   Szymańska, E.; Saccenti, E.; Smilde, A. K.; Westerhuis, J. A. *Metabolomics* **2012**, *8*, 3.

(21)   Xia, J.; Wishart, D. S. *Nat. Protoc.* **2011**, *6* (6), 743.

(22)   Pérez-Enciso, M.; Tenenhaus, M. *Hum. Genet.* **2003**, *112* (5–6), 581.

(23)   Aguilera, A. M.; Escabias, M.; Valderrama, M. J. *Comput. Stat. Data Anal.* **2006**, *50* (8), 1905.

3.6 Appendix A: Supplementary tables

Table 3.1 Patient clinical characteristics for this trial (last updated on 05.18.2017)

		Numbers
Patient follow-up information	Deceased	99
	Alive	1
	Unknown	5
Age (years)	Mean	59.0
	Median	60.5
	Range	28 - 89
Overall Survival (days), unknown patients excluded	Mean	1111.3
	Median	644.5
	Range	219 - 6957

Table 3.2 Single stranded DNAs used in this study.

Name	DNA Sequence
B	5'-NH$_2$-C6-AAA AAA AAA AAA AGC CTC ATT GAA TCA TGC CTA -3'
B'	5'-NH$_2$-C6-AAA AAA AAA ATA GGC ATG ATT CAA TGA GGC -3'
C	5'-NH$_2$-C6-AAA AAA AAA AAA AGC ACT CGT CTA CTA TCG CTA -3'
C'	5-NH$_2$-C6-AAA AAA AAA ATA GCG ATA GTA GAC GAG TGC -3'
D	5'-NH$_2$-C6-AAA AAA AAA AAA AAT GGT CGA GAT GTC AGA GTA-3'
D'	5'-NH$_2$-C6-AAA AAA AAA ATA CTC TGA CAT CTC GAC CAT-3'
E	5'-NH$_2$-C6-AAA AAA AAA AAA AAT GTG AAG TGG CAG TAT CTA -3'
E'	5'-NH$_2$-C6-AAA AAA AAA ATA GAT ACT GCC ACT TCA CAT-3'
F	5'-NH$_2$-C6-AAA AAA AAA AAA AAT CAG GTA AGG TTC ACG GTA-3'
F'	5'-NH$_2$-C6-AAA AAA AAA ATA CCG TGA ACC TTA CCT GAT-3'
G	5'-NH$_2$-C6-AAA AAA AAA AAA AGA GTA GCC TTC CCG AGC ATT-3'
G'	5'-NH$_2$-C6-AAA AAA AAA AAA TGC TCG GGA AGG CTA CTC-3'
H	5'-NH$_2$-C6-AAA AAA AAA AAA AAT TGA CCA AAC TGC GGT GCG-3'
H'	5'-NH$_2$-C6-AAA AAA AAA ACG CAC CGC AGT TTG GTC AAT-3'
K	5'-NH$_2$-C6-AAA AAA AAA AAA ATA ATC TAA TTC TGG TCG CGG-3'
K'	5'-NH$_2$-C6-AAA AAA AAA ACC GCG ACC AGA ATT AGA TTA-3'
L	5'-NH$_2$-C6-AAA AAA AAA AAA AGT GAT TAA GTC TGC TTC GGC-3'
L'	5'-NH$_2$-C6-AAA AAA AAA AGC CGA AGC AGA CTT AAT CAC-3'
M	5'-NH$_2$-C6-AAA AAA AAA AAA AGT CGA GGA TTC TGA ACC TGT-3'
M'	5'-NH$_2$-C6-AAA AAA AAA AAC AGG TTC AGA ATC CTC GAC-3'
N	5'-NH$_2$-C6-AAA AAA AAA AAA AGT CCT CGC TTC GTC TAT GAG-3'
N'	5'-NH$_2$-C6-AAA AAA AAA ACT CAT AGA CGA AGC GAG GAC-3'
O	5'-NH$_2$-C6-AAA AAA AAA AAA ACT TCG TGG CTA GTC TGT GAC-3'
O'	5'-NH$_2$-C6-AAA AAA AAA AGT CAC AGA CTA GCC ACG AAG-3'
P	5'-NH$_2$-C6-AAA AAA AAA AAA ATC GCC GTT GGT CTG TAT GCA-3'
P'	5'-NH$_2$-C6-AAA AAA AAA ATG CAT ACA GAC CAA CGG CGA-3'
Q	5'-NH$_2$-C6-AAA AAA AAA AAA ATA AGC CAG TGT GTC GTG TCT-3'
Q'	5'-NH$_2$-C6-AAA AAA AAA AGA CAC GAC ACA CTG GCT TAT-3'

Table 3.3 List of capture and detection antibodies used in this study.

DNA	Protein	Manufacturer	Capture Ab Catalog #	Detection Ab Catalog #
B'	TGFb1	R&D	DY240	
C'	VEGF R2	R&D	DY357	
D'	IL12	eBioscience	14-7128-82	13-7129-85
E'	HGF	R&D	DY294	
F'	IL13	BD	554570	
		eBiosience		13-7138-81
G'	MMP2	R&D	DY1496	
H'	Serpin E1	R&D	DY1786	
I'	MIP1a	R&D	DY270	
K'	Ch3L1	R&D	DY2599	
L'	IL23	eBioscience	14-7238-85	13-7129-85
N'	IL10	eBioscience	16-7108-85	13-7109-85
O'	MCP1	eBioscience	16-7099-85	13-7096-85
P'	SDF1a	R&D	DY350	
Q'	TNFa	eBioscience	16-7348-85	13-7349-85

Table 3.4 The fitted classification functions of the PLS-DA model with raw protein levels.

Variable	Responder	Non-responder
Intercept	5.311E-01	4.689E-01
IL2	1.836E-05	-1.836E-05
MCP1	-3.286E-05	3.286E-05
IL6	1.562E-05	-1.562E-05
GCSF	-1.120E-05	1.120E-05
MIF	3.265E-05	-3.265E-05
EGF	1.537E-05	-1.537E-05
VEGF	-1.379E-05	1.379E-05
PDGF	4.807E-05	-4.807E-05
TGFa	-9.965E-06	9.965E-06
IL8	-6.374E-06	6.374E-06
MMP3	5.040E-06	-5.040E-06
HGF	-3.866E-05	3.866E-05
IP10	2.793E-06	-2.793E-06
SDF1a	-9.881E-07	9.881E-07
IGFBP2	6.461E-06	-6.461E-06
IGFBP5	-4.348E-05	4.348E-05
MIP1a	-4.485E-05	4.485E-05
TGFb1	-2.108E-04	2.108E-04
Ch3L1	1.104E-05	-1.104E-05
VEGFR3	-2.496E-05	2.496E-05
TNFa	-1.568E-05	1.568E-05
C3	-1.377E-05	1.377E-05
MMP2	-1.211E-04	1.211E-04
IL10	3.375E-05	-3.375E-05
IL1b	-3.983E-05	3.983E-05
IL12	-7.947E-05	7.947E-05
MMP9	-1.142E-05	1.142E-05
TGFb2	3.961E-05	-3.961E-05
GMCSF	2.288E-05	-2.288E-05
CRP	-5.066E-06	5.066E-06
VEGF R2	8.319E-05	-8.319E-05
IL13	2.758E-05	-2.758E-05
IL23	-3.468E-05	3.468E-05
Serpin E1	3.641E-05	-3.641E-05
Fibrinogen 1F3	-6.714E-06	6.714E-06

Table 3.5 VIPs of the PLS-DA model with raw protein levels

Variable	VIP	Standard deviation	Lower bound (95%)	Upper bound (95%)
TGFb1	1.856	0.386	1.100	2.612
VEGF R2	1.825	0.267	1.301	2.348
HGF	1.485	0.338	0.823	2.146
IL12	1.460	0.236	0.997	1.922
MMP2	1.449	0.384	0.696	2.201
MIP1a	1.227	0.237	0.764	1.691
MCP1	1.187	0.225	0.747	1.628
IL23	1.186	0.109	0.971	1.400
SDF1a	1.163	0.229	0.715	1.611
Ch3L1	1.154	0.367	0.434	1.873
TNFa	1.030	0.295	0.452	1.608
Serpin E1	1.017	0.409	0.215	1.818
TGFb2	1.003	0.317	0.382	1.625
IL8	0.991	0.231	0.537	1.444
Fibrinogen 1F3	0.917	0.275	0.379	1.456
GCSF	0.867	0.273	0.332	1.402
IL6	0.866	0.252	0.372	1.360
VEGF	0.858	0.260	0.348	1.368
IL13	0.850	0.488	-0.107	1.806
IL2	0.829	0.396	0.053	1.604
CRP	0.821	0.245	0.340	1.301
TGFa	0.816	0.465	-0.095	1.727
PDGF	0.782	0.428	-0.056	1.620
C3	0.770	0.305	0.171	1.369
MIF	0.760	0.306	0.160	1.360
IL10	0.718	0.448	-0.160	1.596
MMP9	0.681	0.329	0.037	1.325
IL1b	0.672	0.383	-0.078	1.423
GMCSF	0.605	0.449	-0.276	1.486
MMP3	0.528	0.336	-0.131	1.186
VEGFR3	0.510	0.388	-0.250	1.270
EGF	0.502	0.377	-0.238	1.242
IGFBP2	0.495	0.346	-0.184	1.173
IGFBP5	0.466	0.485	-0.484	1.416
IP10	0.217	0.318	-0.405	0.840

Table 3.6 The fitted classification functions of the PLS-DA model with feature scaled protein levels.

Variable	Responder	Non-responder
Intercept	0.119	0.956
IL2	0.179	-0.027
MCP1	-0.099	0.148
IL6	0.116	0.049
GCSF	-0.005	0.124
MIF	0.197	-0.051
EGF	0.126	0.004
VEGF	-0.043	0.118
PDGF	0.180	-0.054
TGFa	-0.055	0.083
IL8	-0.043	0.090
MMP3	0.175	-0.013
HGF	-0.233	0.215
IP10	0.113	0.003
SDF1a	-0.067	0.100
IGFBP2	0.074	0.026
IGFBP5	0.006	0.047
MIP1a	-0.153	0.150
TGFb1	-0.300	0.266
Ch3L1	0.262	-0.084
VEGFR3	0.006	0.057
TNFa	-0.090	0.126
C3	-0.017	0.123
MMP2	-0.164	0.194
IL10	0.235	-0.072
IL1b	-0.033	0.104
IL12	-0.247	0.223
MMP9	0.025	0.092
TGFb2	0.152	-0.034
GMCSF	0.151	-0.029
CRP	-0.020	0.113
VEGF R2	0.335	-0.175
IL13	0.284	-0.134
IL23	-0.135	0.151
Serpin E1	0.295	-0.101
Fibrinogen 1F3	-0.088	0.122

Table 3.7 VIPs of the PLS-DA model with feature scaled protein levels

Variable	VIP	Standard deviation	Lower bound (95% CI)	Upper bound (95% CI)
TGFb1	2.177	0.583	1.034	3.320
VEGF R2	1.820	0.474	0.890	2.750
IL12	1.815	0.443	0.948	2.683
HGF	1.732	0.413	0.923	2.542
IL13	1.474	0.609	0.280	2.668
MMP2	1.440	0.566	0.331	2.548
Serpin E1	1.343	0.659	0.051	2.636
MIP1a	1.186	0.424	0.355	2.018
Ch3L1	1.166	0.762	-0.328	2.660
IL23	1.141	0.416	0.325	1.957
IL10	1.032	0.591	-0.126	2.191
MCP1	1.031	0.364	0.318	1.744
TNFa	0.892	0.473	-0.035	1.819
Fibrinogen 1F3	0.862	0.518	-0.154	1.878
MIF	0.821	0.499	-0.158	1.799
PDGF	0.785	0.482	-0.159	1.729
VEGF	0.730	0.430	-0.113	1.572
SDF1a	0.695	0.407	-0.103	1.492
C3	0.692	0.540	-0.366	1.751
GCSF	0.670	0.364	-0.044	1.384
IL2	0.659	0.533	-0.385	1.703
CRP	0.644	0.632	-0.595	1.884
IL1b	0.630	0.615	-0.576	1.836
TGFb2	0.613	0.541	-0.447	1.673
MMP3	0.586	0.529	-0.450	1.622
GMCSF	0.582	0.499	-0.396	1.561
IL8	0.581	0.358	-0.120	1.281
TGFa	0.575	0.479	-0.364	1.513
MMP9	0.436	0.425	-0.397	1.269
EGF	0.371	0.486	-0.581	1.323
IP10	0.335	0.659	-0.956	1.625
VEGFR3	0.287	0.490	-0.673	1.247
IL6	0.239	0.247	-0.246	0.724
IGFBP5	0.237	0.424	-0.594	1.069
IGFBP2	0.156	0.267	-0.367	0.679

Table 3.8 Correlation coefficients between the estimated tumor volumes and the measured protein levels

	TGFb1	VEGF R2	IL12	HGF	IL13	MMP2	Serpin E1	MIP1a	Ch3L1	IL23	IL10	MCP1	SDF1a	TNFa	Tumor Volume
TGFb1															
VEGF R2	0.6415														
IL12	0.8923	0.5638													
HGF	0.7173	0.6239	0.7219												
IL13	0.8780	0.6405	0.8450	0.7820											
MMP2	0.7696	0.5056	0.7562	0.7026	0.8462										
Serpin E1	0.7584	0.6844	0.7190	0.7338	0.8078	0.7399									
MIP1a	0.7459	0.4522	0.7496	0.6999	0.7956	0.8883	0.7704								
Ch3L1															
IL23	0.8123	0.5821	0.7371	0.7351	0.8786	0.8745	0.8320	0.8865							
IL10	0.8032	0.5415	0.8439	0.7169	0.7767	0.7061	0.7807	0.7661		0.7967					
MCP1	0.8128	0.7433	0.6969	0.7170	0.7609	0.6312	0.7861	0.7040		0.7846	0.7930				
SDF1a	0.6915	0.6564	0.6663	0.5935	0.7177	0.6322	0.7517	0.6369		0.6807	0.6526	0.7730			
TNFa	0.6687	0.5406	0.5626	0.5902	0.7556	0.7890	0.7243	0.7852		0.8597	0.6238	0.6830	0.6304		
Tumor Volume			0.3563		0.3079	0.2584									

Table 3.9 Confusion matrix of the training set (Normalized protein level, subgroup 1)

from \ to	0	1	Total	% correct
0	46	10	56	82.14%
1	6	41	47	87.23%
Total	52	51	103	84.47%

Table 3.10 Confusion matrix of the prediction set (Normalized protein levels, subgroup 1)

from \ to	0	1	Total	% correct
0	7	3	10	70.00%
1	2	13	15	86.67%
Total	9	16	25	80.00%

Table 3.11 Confusion matrix of the training set (Raw protein level, subgroup 1)

from \ to	0	1	Total	% correct
0	33	18	51	64.71%
1	12	40	52	76.92%
Total	45	58	103	70.87%

Table 3.12 Confusion matrix of the prediction set (Raw protein level, subgroup 1)

from \ to	0	1	Total	% correct
0	8	7	15	53.33%
1	2	8	10	80.00%
Total	10	15	25	64.00%

Table 3.13 Confusion matrix of the training set (tumor volume only, subgroup 1)

from \ to	0	1	Total	% correct
0	42	10	52	80.77%
1	24	27	51	52.94%
Total	66	37	103	66.99%

Table 3.14 Confusion matrix of the prediction set (tumor volume only, subgroup 1)

from \ to	0	1	Total	% correct
0	13	1	14	92.86%
1	8	3	11	27.27%
Total	21	4	25	64.00%

Table 3.15 Confusion matrix of the training set (Raw protein level, all subgroups)

from \ to	0	1	Total	% correct
0	172	10	182	94.51%
1	76	22	98	22.45%
Total	248	32	280	69.29%

Table 3.16 Confusion matrix of the prediction set (Raw protein level, all subgroups)

from \ to	0	1	Total	% correct
0	36	3	39	92.31%
1	25	6	31	19.35%
Total	61	9	70	60.00%

Table 3.17 Model parameters of the fitted training set (Normalized protein level, subgroup 1)

Source	Value	Standard error	Lower bound (95%)	Upper bound (95%)
Intercept	2.138E+00	5.799E-01	1.001E+00	3.274E+00
TGFb1	-1.883E+01	1.555E+01	-4.931E+01	1.165E+01
VEGF R2	-6.993E-01	1.063E+00	-2.782E+00	1.383E+00
IL12	-6.317E+01	1.763E+01	-9.773E+01	-2.862E+01
HGF	2.466E+00	1.441E+00	-3.586E-01	5.290E+00
IL13	1.132E+01	9.019E+00	-6.353E+00	2.900E+01
MMP2	2.933E+00	6.735E+00	-1.027E+01	1.613E+01
SerpinE1	-3.930E+00	2.884E+00	-9.582E+00	1.722E+00
MIP1a	-8.065E+00	6.525E+00	-2.085E+01	4.723E+00
Ch3L1	-3.838E-02	1.581E-01	-3.483E-01	2.716E-01
IL23	1.460E+01	5.762E+00	3.305E+00	2.589E+01
IL10	-1.476E+01	8.231E+00	-3.089E+01	1.372E+00
MCP1	2.253E+00	2.504E+00	-2.654E+00	7.161E+00
SDF1a	-2.597E-01	1.037E+00	-2.292E+00	1.773E+00
TNFa	-4.830E+00	3.418E+00	-1.153E+01	1.869E+00

Table 3.18 Model parameters of the fitted training set (Raw protein level, subgroup 1)

Source	Value	Standard error	Lower bound (95%)	Upper bound (95%)
Intercept	1.330E+00	1.136E+00	-8.964E-01	3.556E+00
TGFb1	1.418E-03	1.393E-03	-1.311E-03	4.147E-03
VEGF R2	-4.432E-04	2.589E-04	-9.506E-04	6.421E-05
IL12	-2.013E-03	1.483E-03	-4.920E-03	8.946E-04
HGF	2.733E-04	2.491E-04	-2.149E-04	7.614E-04
IL13	1.929E-03	9.353E-04	9.584E-05	3.762E-03
MMP2	5.050E-04	5.085E-04	-4.916E-04	1.502E-03
SerpinE1	-2.333E-03	1.005E-03	-4.303E-03	-3.630E-04
MIP1a	-8.393E-04	6.460E-04	-2.106E-03	4.269E-04
Ch3L1	1.566E-05	4.028E-05	-6.328E-05	9.461E-05
IL23	-1.290E-04	3.558E-04	-8.264E-04	5.684E-04
IL10	2.720E-05	1.823E-03	-3.546E-03	3.600E-03
MCP1	-2.190E-04	2.359E-04	-6.814E-04	2.434E-04
SDF1a	2.318E-04	2.778E-04	-3.128E-04	7.764E-04
TNFa	5.273E-05	4.014E-04	-7.339E-04	8.394E-04

Table 3.19 Model parameters of the fitted training set (Tumor volume, subgroup 1)

Source	Value	Standard error	Lower bound (95%)	Upper bound (95%)
Intercept	-9.569E-01	3.183E-01	-1.581E+00	-3.331E-01
Tumor Volume	1.181E-04	3.339E-05	5.262E-05	1.835E-04

Table 3.20 Model parameters of the fitted training set (Raw protein level, All subgroups)

Source	Value	Standard error	Lower bound (95%)	Upper bound (95%)
Intercept	-7.054E-01	5.101E-01	-1.705E+00	2.944E-01
TGFb1	3.824E-04	5.100E-04	-6.172E-04	1.382E-03
VEGF R2	-1.952E-04	8.077E-05	-3.535E-04	-3.693E-05
IL12	-5.970E-04	5.718E-04	-1.718E-03	5.237E-04
HGF	2.418E-05	6.724E-05	-1.076E-04	1.560E-04
IL13	4.490E-04	2.921E-04	-1.235E-04	1.022E-03
MMP2	2.477E-04	1.672E-04	-8.000E-05	5.754E-04
SerpinE1	-3.602E-04	2.401E-04	-8.308E-04	1.104E-04
MIP1a	-4.126E-04	2.223E-04	-8.483E-04	2.314E-05
Ch3L1	4.440E-05	1.793E-05	9.268E-06	7.954E-05
IL23	-1.440E-04	1.454E-04	-4.290E-04	1.410E-04
IL10	-1.865E-04	2.520E-04	-6.804E-04	3.073E-04
MCP1	2.583E-06	1.028E-04	-1.990E-04	2.041E-04
SDF1a	-5.525E-05	1.466E-04	-3.425E-04	2.320E-04
TNFa	2.454E-04	1.649E-04	-7.781E-05	5.687E-04

3.7 Appendix B: Supplementary figures
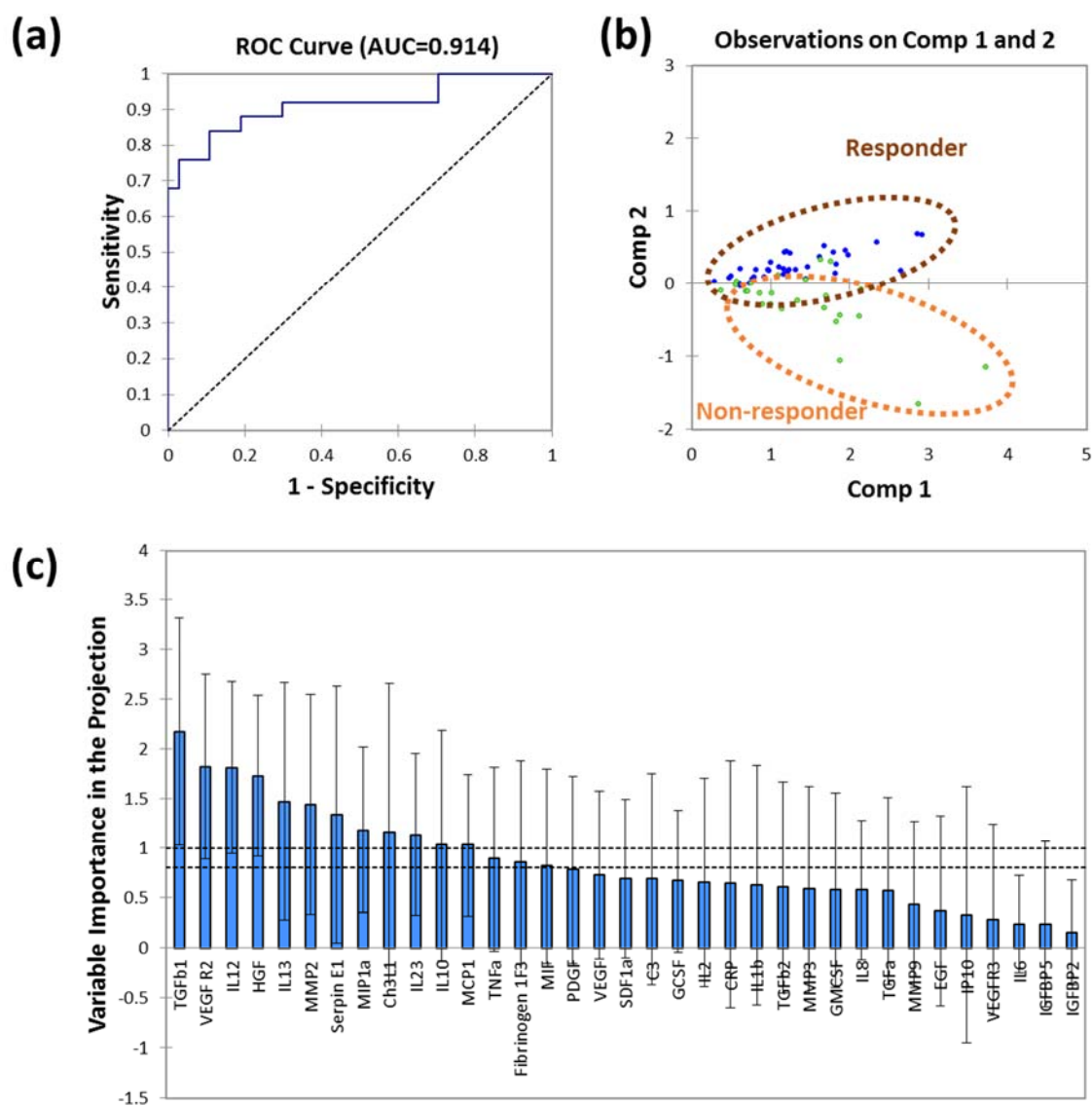
Figure 3.9 PLS-DA modeling of 35-plex proteome data of 62 samples. Feature scaled protein levels were used here. (a) Receiver operating characteristic curve of the model with the area under the curve of 0.914. (b) Projection of the data points onto 2 components of the fitted model. (c) Variance importance in the projection of the 35 protein markers. 95% confidence interval shown as the bars.
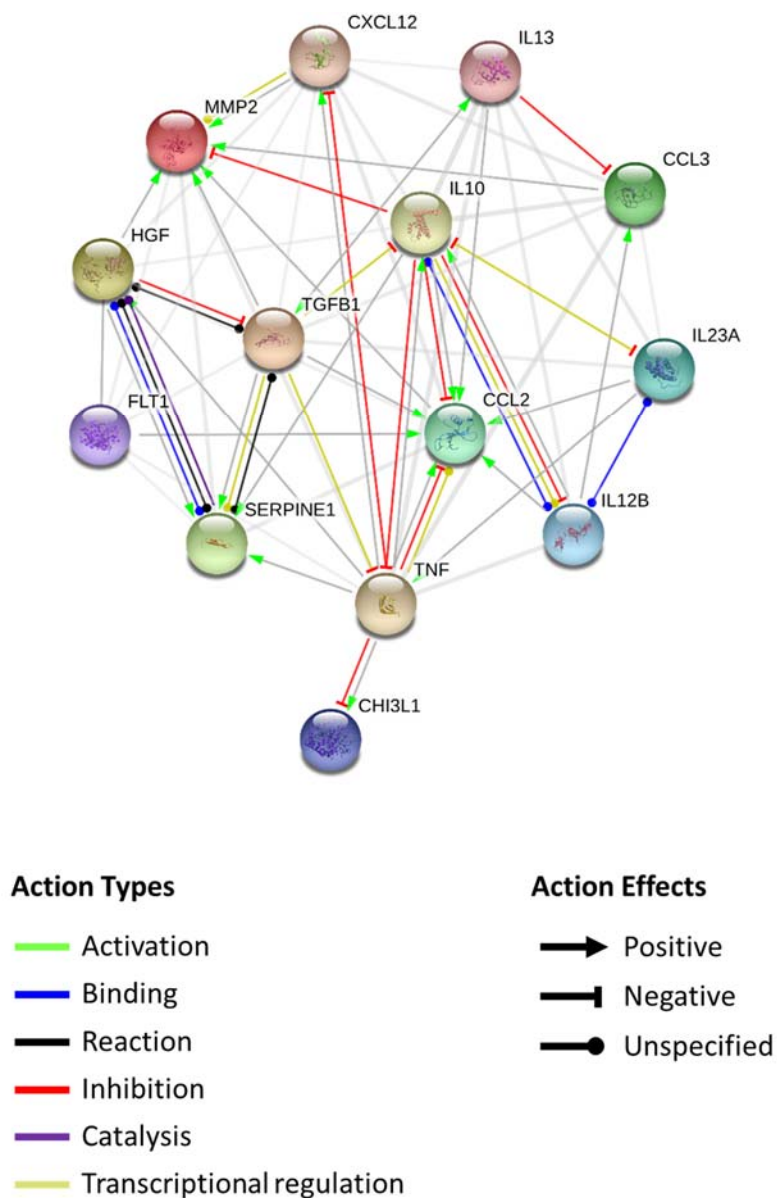
Figure 3.10 Protein-protein interaction map of 14 protein markers measured in this study. STRING (Search Tool for the Retrieval of Interacting Genes/Proteins), a web-based open source software, was used to map out these interactions (https://string-db.org/). Most of the proteins are highly related with each other which causes the multi-collinearity in the data set. (FLT1, Fms-related tyrosine kinase 1, i.e. vascular endothelial growth factor/vascular permeability factor receptor; IL12B, IL-12 p40; IL23A, IL23; CCL2, MCP-1; CCL3, MIP-1α; CXCL12, SDF-1α).
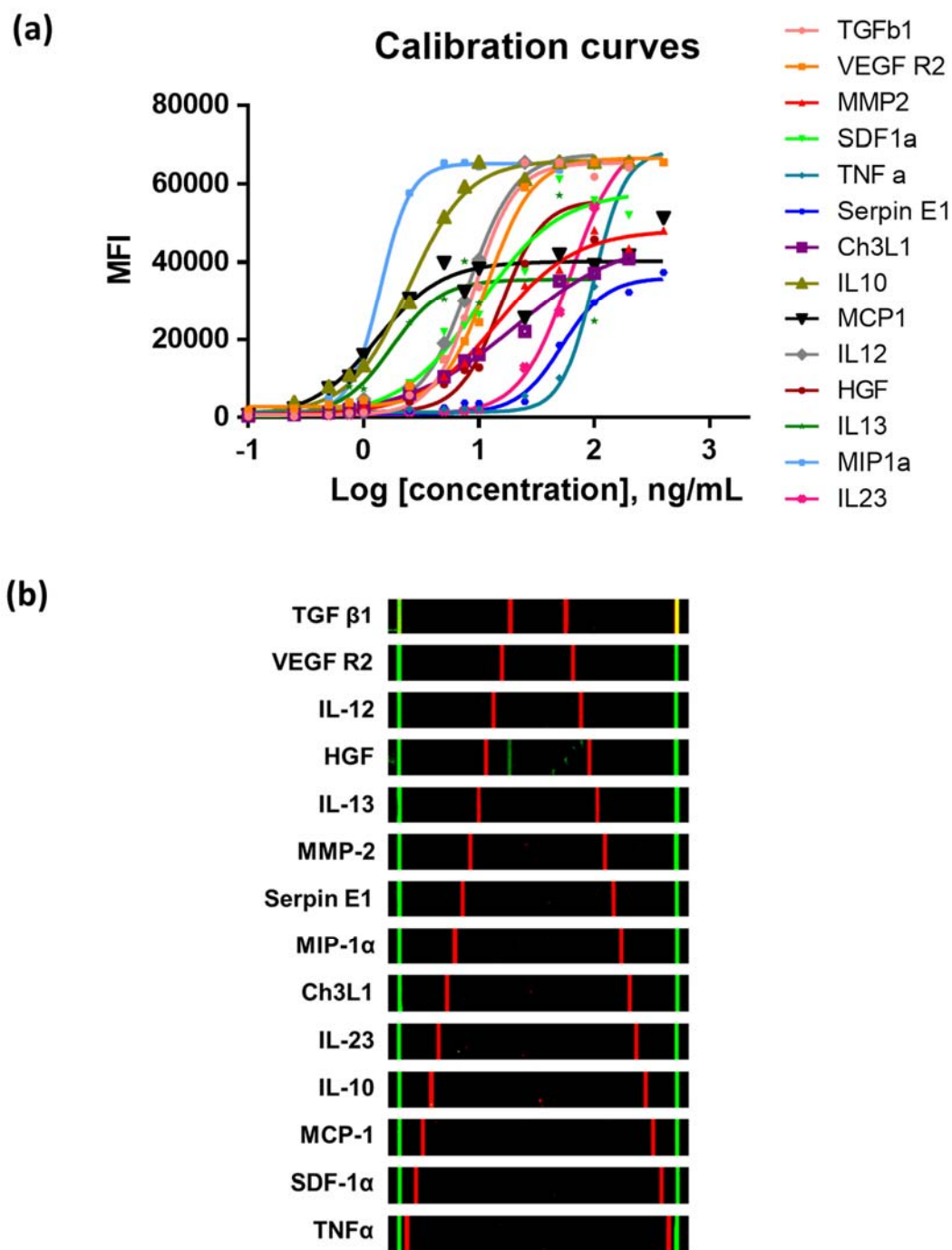
Figure 3.11 Technology validation. (a) Calibration curves. A four-parameter logistic model was fitted to all 14 proteins (b) Cross-talk validation of the antibody panel used in this study.
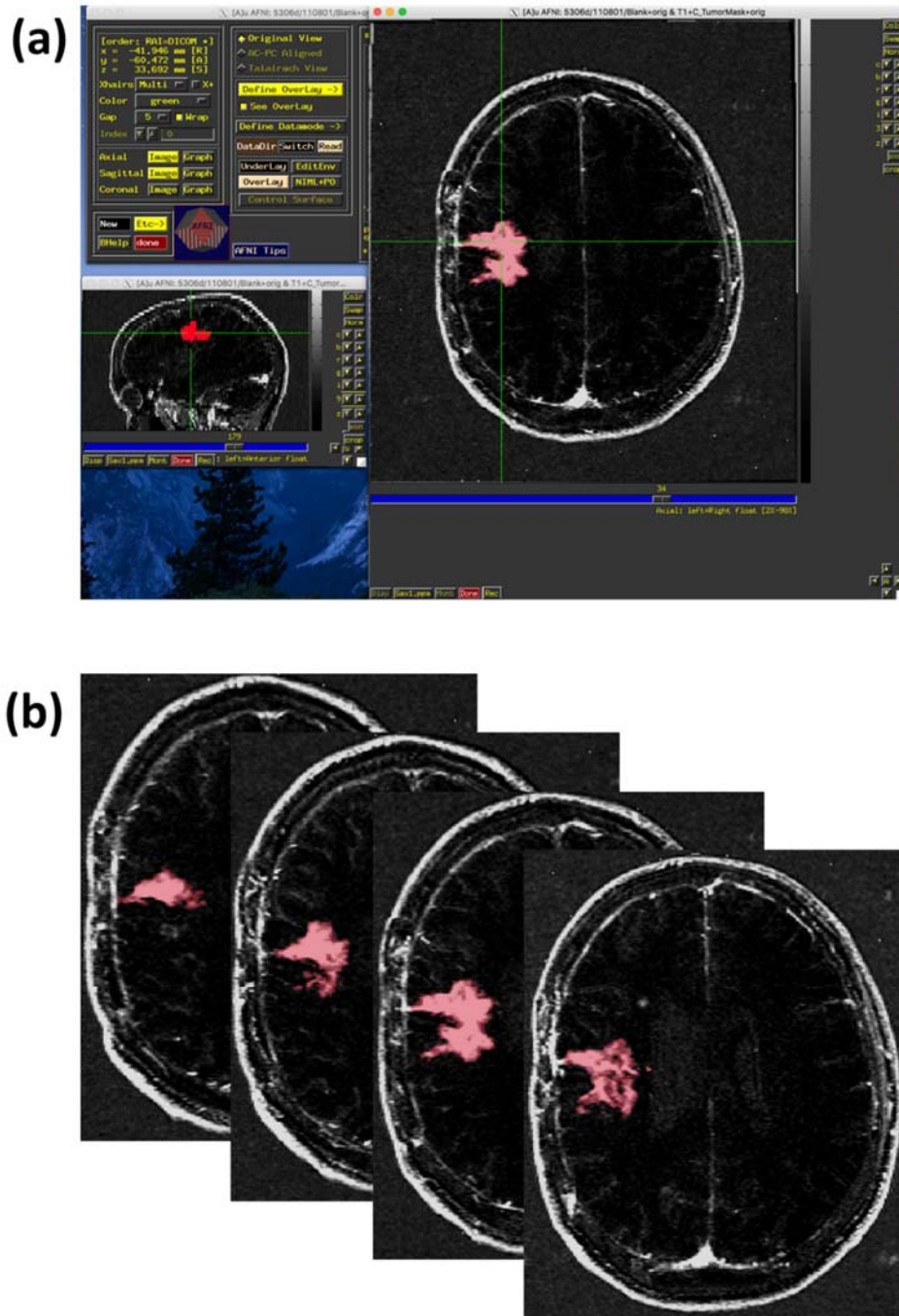
Figure 3.12 Operation of AFNI software. (a) Software interface. Basic information of MRI scan slices was shown at the upper left corner with available program functions. Tools to visualize scan slices and to draw ROIs were shown at the upper right corner. ROI was drawn on the tumor and highlighted in red. Selected tumor location (cross points of green lines) was displayed in 2 trajectories (x-y and y-z planes). (b) MRI scan slices of a GBM patient with ROIs drawn. ROIs were stacked and integrated into tumor volume.

Chapter 4

Plasma proteomic measurement for diagnosing and predicting the early responses to a phosphoinositide 3-kinase (PI3K) targeted therapy in recurrent glioblastoma

4.1 Introduction

The phosphoinositide 3-kinase (PI3K) signaling transduction pathway plays a pivotal role in regulating various cellular functions such as metabolism, protein synthesis, proliferation, and apoptosis. PI3K phosphorylates phosphatidylinositol 4,5-bisphophate (PIP2), a phospholipid in cell membranes, into phosphatidylinositol 3,4,5-trisphophate (PIP3) which is a secondary messenger to activate the downstream protein kinase B (Akt) and mechanistic target of rapamycin (mTOR) effector pathways sequentially. There are 3 classes of PI3Ks, and class I is most implicated in cancer. The class I PI3K is a heterodimer of p110 catalytic subunit and p85 regulatory subunit. The p85 subunit binds to the phosphotyrosine residues of the activated receptor tyrosine kinases (RTKs) and consequently activates the p110 subunits. There are additional regulators in the PI3K pathway. PIP3 is dephosphorylated by phosphatase and tensin homolog (PTEN) as the negative regulation mechanism. Rat sarcoma protein (Ras), a class of GTPase, can activate the p110 subunit. Oncogenic activation of this complicated cellular signaling machinery is

frequently associated with most of cancer types, and the diverse genetic alterations in PI3K, RTKs, PTEN, and RAS have been reported to cause this dysfunction. Particularly in glioblastoma multiforme (GBM), the genetic alterations of PI3KCA (a gene encoding the p110α subunit), epidermal growth factor receptor (EGFR), or PTEN account for 63-86% of primary and 31% of secondary tumor patients.[1–3]

Buparlisib, also known as BKM120, is small molecule inhibitor of pan-class I PI3K and is orally deliverable to tumor patients. It acts as an ATP-competitive inhibitor for all four p110 subunit isoforms, exhibiting the greatest inhibitory potency to the p110α subunit. This drug was developed by a structure-guided approach which involved a series of modifications on its functional groups. In the development process, pharmacokinetic assays were performed to evaluate *in vitro* and *in vivo* inhibitory effects of the drug analogs in terms of PI3K activity, Akt phosphorylation, and tumor proliferation. Buparlisib specifically inhibited the proliferation of cancer cell lines bearing PI3KCA mutations but neither PTEN nor KRas mutations. However, this drug is still tested in clinical trials in several types of solid tumors including breast cancer, lung cancer, colorectal cancer, brain cancer, skin cancer, ovarian cancer, and prostate cancer.[2,4–6]

As discussed in chapter 3, there is an outstanding need for quantitative biomarkers or classifiers that can differentiate responders from non-responders for GBM patients treated with targeted inhibitors. We thus sought to obtain a biomarker signature that could differentiate responders to buparlisib from non-responders in patients with recurrent GBM via serum proteomic analysis. The same methodology of the microchip-based sandwich immunofluorescence assay was employed in this study as the bevacizumab clinical trial in

chapter 3. We collected serum samples from each patient at several points over the time-course of the trial, and then analyzed that serum for the levels of a panel of relatively general plasma protein biomarkers that we have observed as abundant in the serum of GBM cancer patients. The panel was comprised of immune markers, including the cytokines Interleukin (IL)-1β, IL-12, IL-2, and transforming growth factor β1 (TGF β1), the matrix metalloprotease 9 (MMP9), protease inhibitor Serpin E1, the angiogenesis associated vascular endothelial growth factor receptor 2 (VEGF R2) and its ligand VEGF, and Complement component 3 (C3). Because these measured protein levels show the inter-individual variability in the GBM patients, we normalized the measured levels for each patient to what was measured for that patient pre-treatment.

4.2 Materials and methods

4.2.1 Study design

This study was conducted as a part of a clinical study entitled, "A phase II study of BKM 120 for patients with recurrent glioblastoma and activated PI3K pathway." Registered clinical trial identifier number is NCT01339052, and more detailed information about this study can be found in the clinical study depository of the U.S. National Institutes of Health, at https://clinicaltrials.gov/.[7]

In summary, 65 recurrent GBM patients (≥ 18 years of age & Karnofsky performance status ≥ 60) participated in this study. These patients had not received more than 2 prior therapies before this clinical trial. They were classified into 2 cohorts, one

which received surgery (cohort 1, n = 15) and the other which did not receive surgery (cohort 2, n = 50). Cohort 1 received the monotherapy of buparlisib ($100^{mg}/_{day}$, 8-12 days prior to surgery and 28-day cycles after surgery). Cohort 2 received the same therapy with the same dose for 28-day cycles. Buparlisib was taken orally by the patients, and the treatment continued until disease progression occurred or the patients suffered unacceptable toxicity. Patient cohort clinical characteristics for this trial can be found in Appendix A, Table 4.1.

4.2.2 Plasma collection and processing

Patient blood samples were collected and processed as follows. On the first day of each drug treatment cycle, 8-10mL of blood was drawn from a patient and transferred to a tube containing anti-coagulant (BD Vacutainer Yellow Acid-citrate-dextrose (ACD) Blood Collection Tubes). Samples were mixed thoroughly by inverting tubes 8-10 times. Tubes were centrifuges at 1500×g in a refrigerated centrifuge (3-5°C). ~200μL Plasma samples were aliquoted into cryogenic vials and stored at -80°C. Samples were processed within 2 hours of blood draw. The aliquoted samples were thawed and used immediately for the sandwich immunofluorescence assay.

4.2.3 DNA-barcode chip fabrication and DNA-encoded antibody library (DEAL) preparation

The methods for DNA-Encoded Antibody Library (DEAL) preparation, antibody Alexa Fluor 647 (AF647) conjugation, cross-reactivity validation of DEAL conjugates and detection antibodies, DNA barcode microarray patterning, and 16-microwell PDMS slab

fabrication are previously described.[8,9] Procedures are briefly described here. Lists of DNA sequences and antibodies are summarized in Appendix A, Table 4.2 and 4.3.

4.2.3.1 DNA-patterning on a glass slide

Each mold of 50 µm wide and 40 µm high patterns was prepared with SU8 2025 (Microchem) by standard photolithograpy methods. The mold surface was treated with trimethylchlorosilane (TMCS, Sigma Aldrich). Polydimethylsiloxane (PDMS) barcode slab was prepared as follows. Sylgard 184 elastomer was mixed (pre-polymer : curing agent = 10:1, Dow Corning), degassed, poured on the mold, and cured at $80\,^\circ$C for 2 hours. Cured PDMS slab was cut, peeled from the mold, inlet and outlet holes punched, and aligned with a poly-L-lysine (PLL) coated glass slide (Thermo Scientific). The aligned PDMS slab and PLL glass slide were bonded at $80\,^\circ$C for 2 hours. 10 channels were used in this study. After bonding, a 0.1% PLL solution (Sigma Aldrich) was flown through the individual channels and dried overnight by air flow overnight, using solution loading devices. Details about the solution loading devices can be found in chapter 5 of this thesis. Then, the solutions of single stranded DNA (ssDNA) oligo B to M (Bioneer, Inc.) were loaded in the PLL-deposited channels by airflow, using the solution loading devices. Stock ssDNA solutions were first prepared in a mixture of dimethyl sulfoxide (DMSO, American Type Culture Collection) and phosphate buffered saline at pH 7.4 (PBS, Corning). The ssDNA solutions were mixed with bis(sulfosuccinimidyl)suberate (BS3, ThermoFisher Scientific) linker solution in PBS immediately before flowing. This DNA-solution filled PDMS-glass assembly was incubated at incubated at room temperature for 2 hours in a humidifier chamber. The PDMS slab was peeled off after the incubation, and the DNA

patterned glass slide was washed with 0.02% SDS once and Millipore water three times sequentially. The glass slide was spin-dried with a Miniarray microcentrifuge (VWR). A region of DNA pattern near one edge of the glass slide was incubated with a cocktail of Cy3 conjugated B'- M' (Integrative DNA Technologies) in 1% BSA in PBS at 37 $^\circ$C for 1 hour for DNA pattern quality assessment. The region was scanned with an Axon GenePix 4400A machine (532nm at PMT 450, laser power 15%, $10^{\mu m}/_{pixel}$), and the fluorescence intensity was measured.

4.2.3.2 DNA-antibody conjugation

Each capture antibody was first reconstituted in PBS and desalted using a Zeba spin column (ThermoFisher Scientific). Succinimidyl 4-hydrazinonicotinate acetone hydrazine (S-HyNic, Solulink) in anhydrous N,N'-dimtheylformamide (DMF, Solulink) solution was added to the antibody solution and incubated at room temperature for 2 hours. In parallel, individual ssDNA oligos B'-L' (Integrative DNA Technologies) were dissolved in PBS and mixed with succinimidyl 4-formylbenzoate (S-4FB, Solulink) in DMF solution. The mixture was incubated at room temperature for 2 hours. Each reaction mixture was buffer exchanged into a pH 6.0 citrate buffer using Zeba spin columns. These buffer-exchanged solutions were combined, and incubated at room temperature for 2 hours then at 4°C overnight. The DNA-antibody conjugate was purified by Fast protein liquid chromatography (FPLC, GE Pharmacia Superdex 200 gel filtration column), and the purified conjugate was concentrated by centrifugation (Millipore, Amicon Ultra-4, MWCO 10kDa).

4.2.3.3 Antibody Alexa Fluor 647 conjugation

Only the C3 detection antibody (Abcam, ab14232) was conjugated with AF647. The antibody was first desalted using a Zeba spin column and buffer exchanged into Phosphate Buffer Saline (PBS, Irvine Scientific). Antibody was reacted with AF647-succinimidyl ester (Life Technologies) following the manufacturer's protocol.

4.2.4 Multiplexed sandwich immunofluorescence assays for protein measurements

Sandwich immunofluorescence assay was performed for measuring proteins in the patient serum samples. Procedures were as follows.

1) *Conversion of DNA barcode microarray into capture antibody microarrays.* A 16-microwell PDMS microwell slab was dried by air-blowing and aligned with the DNA barcode glass slide. The capture antibody cocktail solution was added to the microwells and incubated at 37 °C for 1 hour. The cocktail solution of the DEAL conjugates and Cy3-M' was prepared in 1% Bovine Serum Albumin (BSA, Sigma Aldrich) in PBS. Cy3-M' was used as a reference for the DNA pattern order. Unbound DEAL conjugates and Cy3-M' were removed by washing the microwells with 1× PBST (Cell Signaling) 3 times. Washing was performed by aspirating the solution in the microwells (from the previous step) and adding 1× PBST solution sequentially. After washing, all the microwells were blocked with 1% BSA in PBS at 37 °C for 1 hour. Residual 1% BSA in PBS was removed by washing the microwells with 1× PBST once.

2) *Patient serum sample loading.* Patient serum samples were thawed and centrifuged at 21,130 × g for 3 mins. Only the supernatant was added to the microwells and incubated at

room temperature with shaking for 1 hour. Residual patient serum samples were removed by washing the microwells with 1× PBST once.

3) *Detection antibody cocktail loading.* The detection antibody cocktail solution was added to the microwells and incubated at room temperature for 1 hour. The cocktail solution was prepared in 1% BSA in PBS by mixing and diluting all the stock solutions of biotin-labeled detection antibodies, AF647 conjugated streptavidin (Life Technologies), and AF647 conjugated C3 antibody stock. Residual detection antibody cocktail was removed by washing the microwells with 1× PBST once.

4) *Fluorescence readout.* The PDMS microwell slab was peeled off and the barcode glass slide was washed with 1× PBS, 0.5× PBS, and Millipore deionized water sequentially. The barcode glass slide was spin-dried and scanned by an Axon GenePix 4400A (Molecular Devices) at $10^{\mu m}/_{pixel}$ resolution: (635nm: PMT 600, 80% power, 532nm: PMT 400, 10% power). Signals from the two color channels were collected and digitized, and the fluorescence signals of barcodes were extracted by the manufacturer's software. 10 spots per barcode lane were extracted for calculating the values of average and coefficient of variation.

4.2.5 Clinical data interpretation

Patient tumor progression was monitored by magnetic resonance imaging (MRI) or computed tomography (CT) during the drug treatment. Patients were classified as responders when one or both following conditions were fulfilled: 1) a patient showed stable disease and 2) progression free survival was 6 months or longer. Clinicians determined the stable disease status, and this patient status implied that a tumor neither grew or shrunk.

The rest of patients were classified as non-responders. For the responders, their best response time point was also determined, and the drug treatment cycles completed before the best response time points were considered as the drug responsive period. Categorical variables were assigned as 0 for responder (stable disease i.e. the drug responsive period of responders) and 1 for non-responder (progressive disease i.e. the non-responsive period of responders and all the treatment cycles of non-responders). These binary values were associated with the measured 9 plasma protein levels.

4.2.6 Data analysis

4.2.6.1 Statistical methods

A two-tailed Mann-Whitney test was used for the pairwise comparison of individual protein levels between responders and non-responders. Correlation coefficients were calculated by Spearman's rank method, and only the correlation coefficients with statistical significance were accepted after the Bonferroni correction.

4.2.6.2 Partial least square discriminant analysis

Since the number of observations is low and the multi-collinearity between measured proteins is high (Figure 4.8, Appendix B), Partial Least Square Discriminant Analysis (PLS-DA) was performed to predict the membership of observations to the categories of responders and non-responders.[10,11] PLS-DA was performed with XLSTAT (Addinsoft) statistical software.

The goal of PLS-DA is to obtain a linear relationship between the measured protein levels and the patient responses to the drug treatment. The measured protein levels of each

patient were normalized by the protein levels of that patient before the treatment, in order to consider the protein level variations between individual patients. PLS-DA begins with a matrix in which the numbers of columns is the numbers of measured proteins and the numbers of rows is the numbers of patient samples. We seek a solution to that matrix that best resolves the responders from the non-responders with the most stable model. Specifically, K is the number of categories (total 2, for either responder or non-responder) of the dependent variable Y (the patient response). For each patient, we have 9 proteins measured. For each category $a_{k\ (k=1,2)}$, we obtain a separate classification function F, so that we obtain one fit that applies to all responders, and a second for all non-responders.

$$F(y_i, a_k) = b_0 + \sum_{j=1}^{p} b_i x_{ij}$$

Here, b_0 is the fitted intercept of the linear model associated each category a_k, p (total 9) is the number of measured proteins (also called explanatory variables) and b_i are the coefficients that weigh each protein within the model. A given patient i is associated to class k (responder or non-responder) depending on which model best describes blood protein levels measured from that patient. Formally, this is written as:

$$k^* = \arg \max_k F(y_i, a_k)$$

In the trial, most patients were treated for 1 or 2 cycles, with a non-statistical number of patient proceeding for additional cycles. Thus, we developed the model using patient responses at the end of Cycle 1 treatment, and validated the model by predicting

patient responses at the end of Cycle 2 treatment. The number of patients treated 3 or more

cycles was too small to develop a model.

4.3 Results and discussion
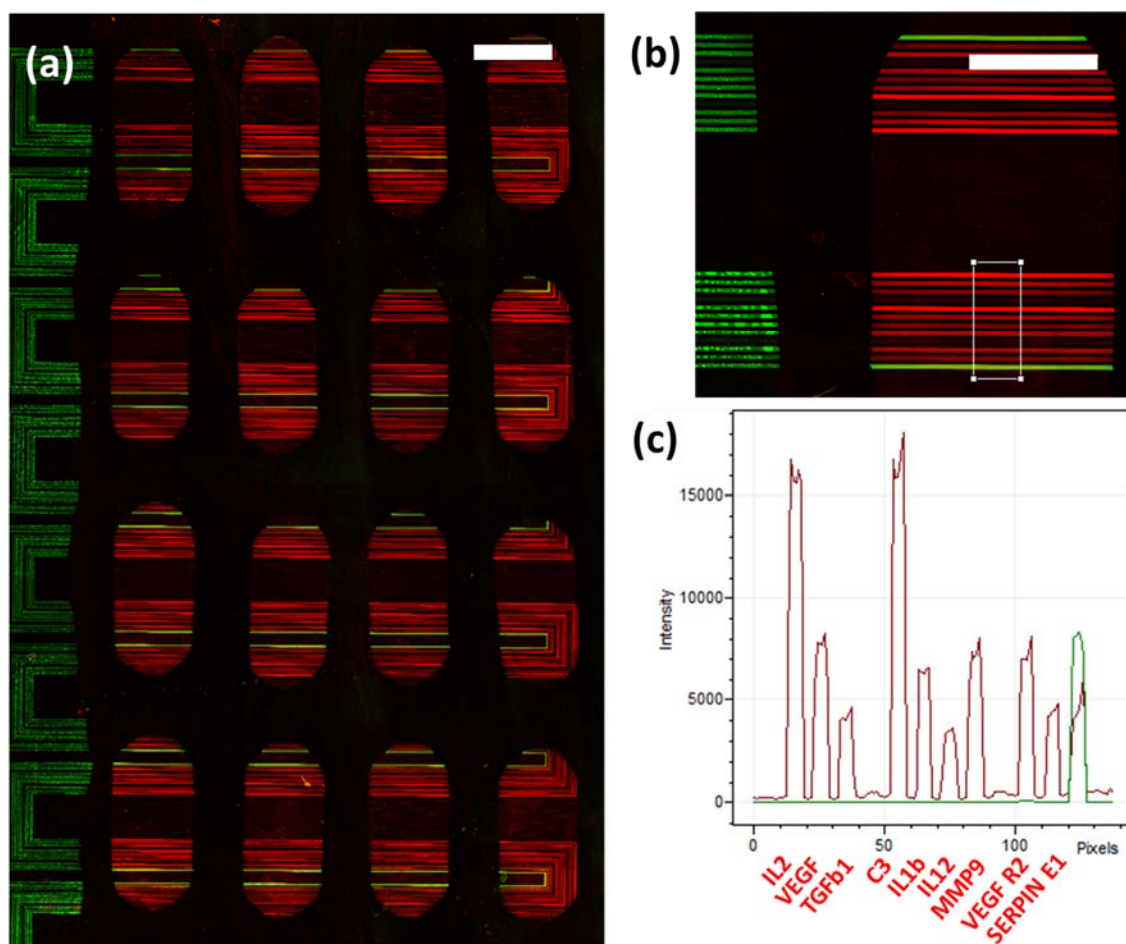
Figure 4.1 Raw data image. (a) Raw scan of a barcode chip after the 9-plex plasma proteomic measurement. Total 16 plasma samples were measured (scale bar: 3mm). (b) A single well magnified in the raw scan. Each well contains 2 sets of antibody arrays for the 9-plex sandwich-type immunofluorescence assays. Cy3 fluorescence, shown as a green stripe, indicated the spatial location of other barcode stripes which identified analytes. Fluorescence intensities were digitized from a line scan, shown as a white box (scale bar: 1.5mm). (c) Digitization results. A red graph represented signals from the immunofluorescence assays and a green graph were from the location indicator of Cy3 fluorescence. Identities of each analyte were labeled.
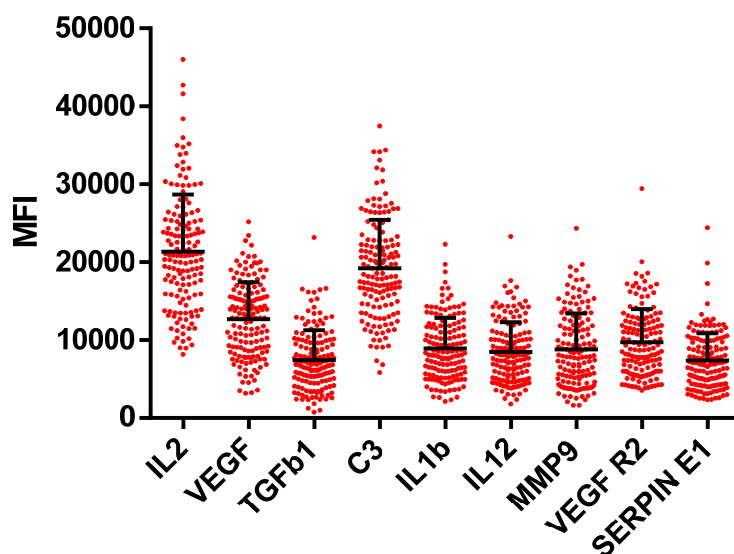
Figure 4.2 Raw measurement data of all the patient plasma samples (n=153). Averages and standard deviations of the measured 9 proteins were shown.

We simultaneously measured 9 proteins in total for the 153 plasma samples collected from cohort 1 and 2 by the sandwich-type immunofluorescence assay (Figure 4.1, Figure 4.2, and Figure 4.9, Appendix B). The average coefficient of variation of the protein measurement was 8.85%, and the range was 1.64%-28.89%. We first observed the interpatient variability in the measured protein levels and hypothesized that relative changes in the protein levels, not absolute values, might be linked to the patient drug responses. Thus, we normalized a patient's protein levels during all the drug treatment cycles to the patient's protein levels in pre-treatment. We then divided the raw data set into several sub-data sets by the following criteria: 1) cohort, 2) drug treatment cycles, and 3) clinically determined drug responses in each cycle. Both raw and normalized protein levels of each cohort are plotted in Appendix B, Figure 4.10-4.15.

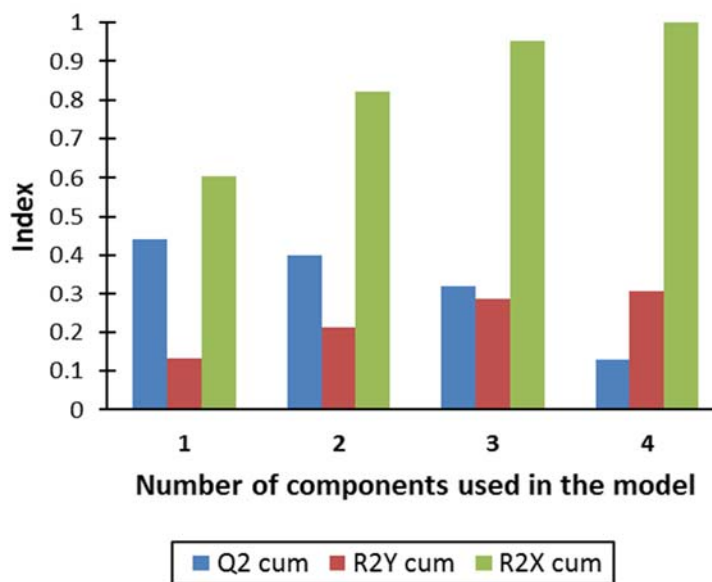**Figure 4.3** Assessment of the explanatory and predictive power of the model in the cohort 2 for the cycle 1 treatment. The explanatory power of the model increases with more components included, shown as increase of R^2X and R^2Y. However, the predictive power of the model decreases simultaneously, shown as decrease of Q^2.

We used PLS-DA for fitting patient responses in cohort 2 at the end of Cycle 1 treatment to either responders or non-responders. A danger of PLS-DA models is that they have the potential to over-fit the data, in which case the model explains 100% of the observations, but is not robust towards making new predictions. We sought a model that had an optimal trade-off between explanatory power and predictive power. Figure 4.3 provides the guidance for choosing an optimal model. In this plot, we evaluate the explanatory power of the model for the protein levels (R^2X cum; green bars) and for the patient responses (R^2Y cum; red bars) as the numbers of components in the fit are increased. When 4 or more components are included in the fit, 100% of the protein observations are explained. However, we also estimate the robustness of the model by 'leave one out' cross-validation computations (Q^2 cum; blue bars). The most predictive model is the least robust.

Based upon this cross-validation test, we utilized the single-component fit, as it should have the most predictive power.
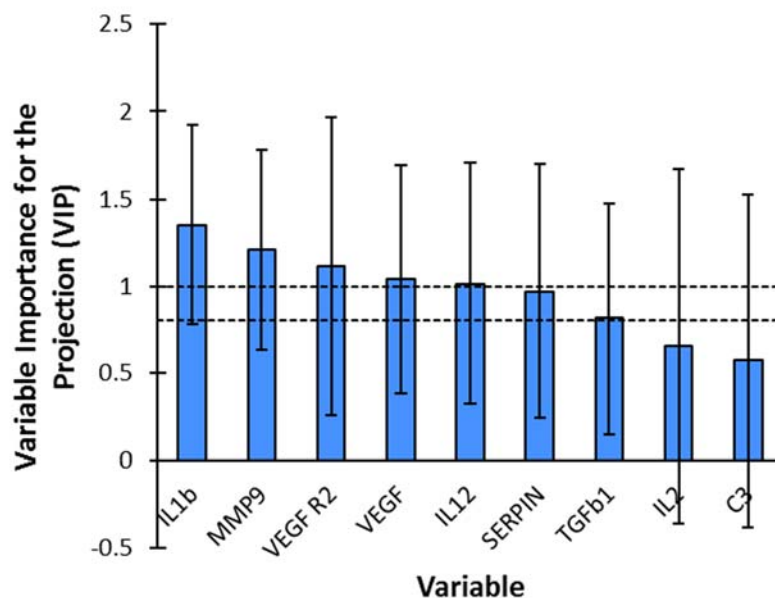
Figure 4.4 Variable Importance of the Projection (VIP) of the protein markers in the Figure 4.3 model. VIP values represent the predictive capacity of the protein markers. These values are obtained from the single-component fit and their 95% confidence intervals are shown.

As mentioned, the PLS-DA model was fitted by defining, for each patient, a baseline prior to the start of Cycle 1 treatment, and by analyzing changes in those protein levels after completion of the Cycle 1 treatment. Based upon the PLS-DA model, we evaluated which proteins exhibited the greatest predictive capacity (Figure 4.4). Proteins IL-1β and MMP9 exhibited the most predictive capacity, while IL-2 and C3 had no predictive power. The fitted classification functions that were determined by the end of Cycle 1 data are summarized in Appendix A, Table 4.4. The confusion matrix at the end of Cycle 1 is provided in Appendix A, Table 4.5. The model fits 12 of 17 responders

correctly, and fits 12 of 17 non-responders correctly, providing a ROC curve with the accuracy of 0.720 (Figure 4.5a).
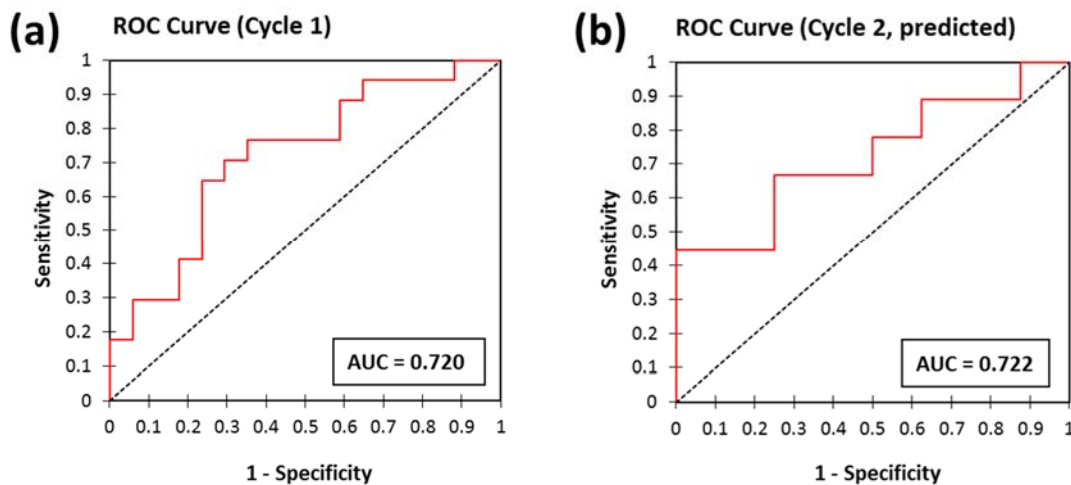
Figure 4.5 ROC curves. (a) ROC curve at the end of Cycle 1 treatment (b) ROC curve at the end of Cycle 2 treatment based on the model prediction.

We then tested the predictive capacity of the PLS-DA model by using the model to predict patient responses during treatment Cycle 2. The Confusion Matrix of the predicted patient responses for Cycle 2 and the ROC curve is provided in Figure 4.5b. and Appendix A, Table 4.6. The predictive capacity of the model for the Cycle 2 patient responses with the accuracy of 0.722 is apparently similar to its explanatory capacity for the Cycle 1 patient responses with the accuracy of 0.720, albeit with fewer patient samples. Nevertheless, this gives us some confidence that serum proteomics can provide insights into predicting patient responses to this targeted inhibitor. Additional analyses of further cycles of therapy treatment were not done, given the small number of patients who proceeded beyond Cycle 2 treatment.

The serum protein levels of patients in the cohort 1were analyzed separately, but again by developing a PLS-DA model using Cycle 1 measures and validating that model by predicting patient responses through Cycle 2. This analysis was statistically poor, because there were very few patients who underwent both surgery and drug treatment. The fitted classification functions and confusion matrices are summarized in Appendix A, Table 4.7-4.9.
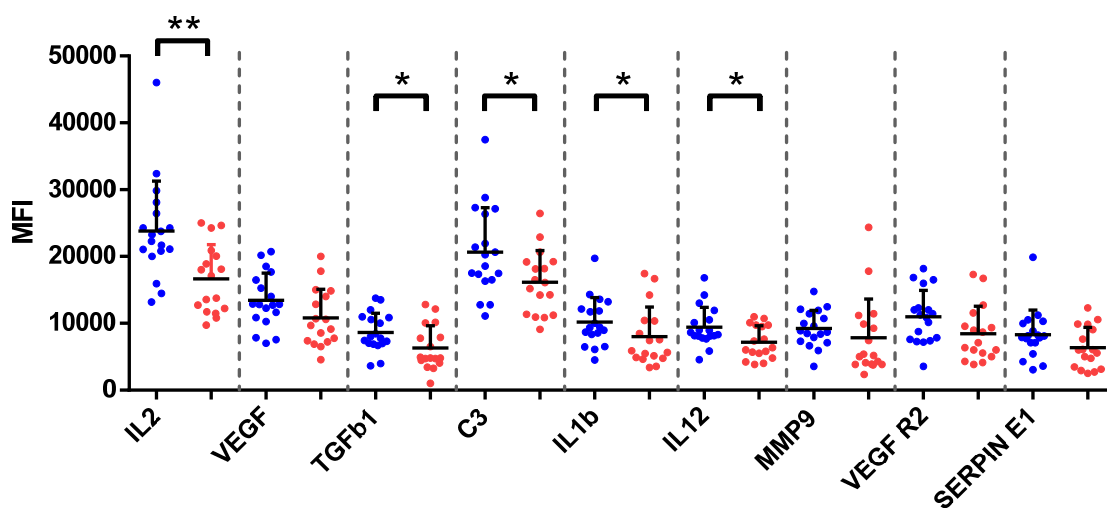
Figure 4.6 Cohort 2 raw protein levels in pre-treatment. Samples were classified by the drug responses after Cycle 1 treatment. Responders (blue, n=18) had higher IL-2, TGF β1, C3, IL-1β, and IL-12 levels compared to non-responders (red, n=17). (*, $p<0.05$; **, $p<0.005$). Averages and standard deviations were shown.

Interestingly, the cohort 2 responders and non-responders after Cycle 1 treatment had different proteomic signatures in their pre-treatment (Figure 4.6). Raw protein levels of IL-2, TGF β1, C3, IL-1β, IL-12 in responders were higher than those in non-responders. Moreover, their protein-protein correlation networks were distinctive (Figure 4.7). All the determined correlation coefficients were above 0.6, which showed only positive

correlations between the 9 measured proteins. More proteins were correlated in the non-responders than responders. Although this observation has to be further validated with higher sample numbers, it may imply that we can find the proteomic classifiers to predict the Cycle 1 drug responses. Such classifiers would be a powerful tool in that we can predict initial patient responses based on the one-time measured protein levels before administering the drug.
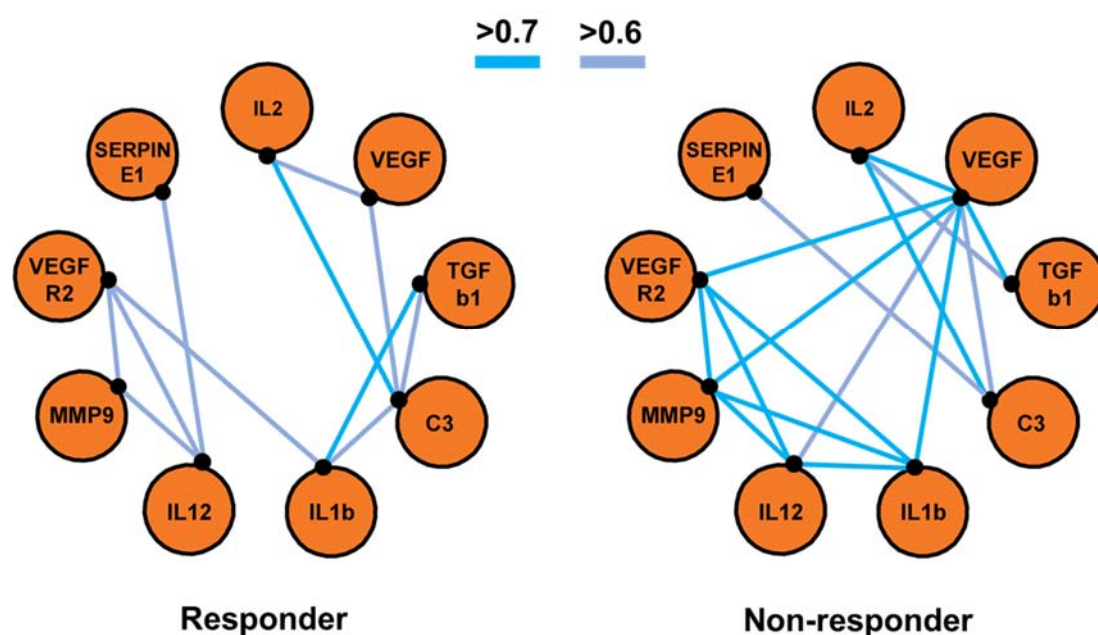
Figure 4.7 Pre-treatment protein-protein networks of cohort 2 responders and non-responders after Cycle 1 treatment.

4.4 Conclusion

We developed the proteomic classifiers for diagnosing the early drug responses of recurrent GBM patients after the first 28-day cycle of buparlisib treatment. These classifiers could predict the drug responses of the next cycle of the treatment. We also found that these classifier models worked with the normalized protein levels to the pre-

treatment levels. The diagnostic and predictive capacities of the model can be useful for monitoring the patient drug responses, which can save time and costs for the drug treatment particularly. This study was limited to a cohort of patients who did not have surgery due to small number of samples, but the findings can be further extended and applied to patients who had both surgery and the drug treatment. In general, this 9-plex proteomic measurement is performed from a finger-prick volume of a patient blood, and its operation is straightforward and easy. Therefore, this platform can be readily implemented in clinical settings for routine drug response monitoring.

4.5 References

(1)   Rodon, J.; Dienstmann, R.; Serra, V.; Tabernero, J. *Nat. Rev. Clin. Oncol.* **2013**, *10* (3), 143.

(2)   Dienstmann, R.; Rodon, J.; Serra, V.; Tabernero, J. *Mol. Cancer Ther.* **2014**, *13* (5), 1021.

(3)   Wen, P. Y.; Lee, E. Q.; Reardon, D. A.; Ligon, K. L.; Yung ,W. K. A. *Neuro. Oncol.* **2012**, *14* (7), 819.

(4)   Maira, S.-M.; Pecchi, S.; Huang, A.; Burger, M.; Knapp, M.; Sterker, D.; Schnell, C.; Guthy, D.; Nagel, T.; Wiesmann, M.; Brachmann, S.; Fritsch, C.; Dorsch, M.; Chene, P.; Shoemaker, K.; De Pover, A.; Menezes, D.; Martiny-Baron, G.; Fabbro, D.; Wilson, C. J.; Schlegel, R.; Hofmann, F.; Garcia-Echeverria, C.; Sellers, W. R.; Voliva, C. F. *Mol. Cancer Ther.* **2012**, *11* (2), 317.

(5)   Burger, M. T.; Pecchi, S.; Wagman, A.; Ni, Z.-J.; Knapp, M.; Hendrickson, T.;

Atallah, G.; Pfister, K.; Zhang, Y.; Bartulis, S.; Frazier, K.; Ng, S.; Smith, A.; Verhagen, J.; Haznedar, J.; Huh, K.; Iwanowicz, E.; Xin, X.; Menezes, D.; Merritt, H.; Lee, I.; Wiesmann, M.; Kaufman, S.; Crawford, K.; Chin, M.; Bussiere, D.; Shoemaker, K.; Zaror, I.; Maira, S.-M.; Voliva, C. F. *ACS Med. Chem. Lett.* **2011**, *2* (10), 774.

(6)   Bendell, J. C.; Rodon, J.; Burris, H. A.; De Jonge, M.; Verweij, J.; Birle, D.; Demanse, D.; De Buck, S. S.; Ru, Q. C.; Peters, M.; Goldbrunner, M.; Baselga, J. *J. Clin. Oncol.* **2012**, *30* (3), 282.

(7)   Phase II Study of BKM120 for Subjects With Recurrent Glioblastoma https://clinicaltrials.gov/ct2/show/NCT01339052.

(8)   Xue, M.; Wei, W.; Su, Y.; Kim, J.; Shin, Y. S.; Mai, W. X.; Nathanson, D. A.; Heath, J. R. *J. Am. Chem. Soc.* **2015**, *137* (12), 4066.

(9)   Shi, Q.; Qin, L.; Wei, W.; Geng, F.; Fan, R.; Shik Shin, Y.; Guo, D.; Hood, L.; Mischel, P. S.; Heath, J. R. *Proc. Natl. Acad. Sci.* **2012**, *109* (2), 419.

(10)   Pérez-Enciso, M.; Tenenhaus, M. *Hum. Genet.* **2003**, *112* (5–6), 581.

(11)   Szymańska, E.; Saccenti, E.; Smilde, A. K.; Westerhuis, J. A. *Metabolomics* **2012**, *8*, 3.

4.6 Appendix A: Supplementary tables

Table 4.1 Patient cohort clinical characteristics for this trial (last updated on 03.26.2015).

		Cohort 1 (n=15)	Cohort 2 (n=50)
Patient follow-up information	Deceased	9	40
	Alive	6	8
	Unknown	0	2
Progression Free Survival (Months)	Mean	4.7	1.8
	Median	1	1
	Range	0-21	0-11
Overall Survival (Months)	Mean	27.6	15.5
	Median	23	9
	Range	2-66	0-63
# of treatment cycles completed (Cycles)	Mean	5.3	2.2
	Median	2	1
	Range	0-23	0-10

Table 4.2 Single stranded DNAs used in this study.

Name	DNA Sequence
B	5'-NH$_2$-C6-AAA AAA AAA AAA AGC CTC ATT GAA TCA TGC CTA -3'
B'	5'-NH$_2$-C6-AAA AAA AAA ATA GGC ATG ATT CAA TGA GGC -3'
C	5'-NH$_2$-C6-AAA AAA AAA AAA AGC ACT CGT CTA CTA TCG CTA -3'
C'	5-NH$_2$-C6-AAA AAA AAA ATA GCG ATA GTA GAC GAG TGC -3'
D	5'-NH$_2$-C6-AAA AAA AAA AAA AAT GGT CGA GAT GTC AGA GTA-3'
D'	5'-NH$_2$-C6-AAA AAA AAA ATA CTC TGA CAT CTC GAC CAT-3'
E	5'-NH$_2$-C6-AAA AAA AAA AAA AAT GTG AAG TGG CAG TAT CTA -3'
E'	5'-NH$_2$-C6-AAA AAA AAA ATA GAT ACT GCC ACT TCA CAT-3'
F	5'-NH$_2$-C6-AAA AAA AAA AAA AAT CAG GTA AGG TTC ACG GTA-3'
F'	5'-NH$_2$-C6-AAA AAA AAA ATA CCG TGA ACC TTA CCT GAT-3'
G	5'-NH$_2$-C6-AAA AAA AAA AGA GTA GCC TTC CCG AGC ATT-3'
G'	5'-NH$_2$-C6-AAA AAA AAA AAA TGC TCG GGA AGG CTA CTC-3'
H	5'-NH$_2$-C6-AAA AAA AAA AAT TGA CCA AAC TGC GGT GCG-3'
H'	5'-NH$_2$-C6-AAA AAA AAA ACG CAC CGC AGT TTG GTC AAT-3'
K	5'-NH$_2$-C6-AAA AAA AAA ATA ATC TAA TTC TGG TCG CGG-3'
K'	5'-NH$_2$-C6-AAA AAA AAA ACC GCG ACC AGA ATT AGA TTA-3'
L	5'-NH$_2$-C6-AAA AAA AAA AGT GAT TAA GTC TGC TTC GGC-3'
L'	5'-NH$_2$-C6-AAA AAA AAA AGC CGA AGC AGA CTT AAT CAC-3'
M	5'-NH$_2$-C6-AAA AAA AAA AGT CGA GGA TTC TGA ACC TGT-3'
M'	5'-NH$_2$-C6-AAA AAA AAA AAC AGG TTC AGA ATC CTC GAC-3'

Table 4.3 List of capture and detection antibodies used in this study.

DNA	Protein	Manufacturer	Capture Antibody Catalog #	Detection Antibody Catalog #
B'	IL-2	R&D Systems	DY202 (KIT)	
C'	VEGF	R&D Systems	DY293B (KIT)	
D'	TGFb1	R&D Systems	DY240 (KIT)	
E'	C3	abcam	ab17455	ab14232
F'	IL-1b	ebioscience	14-7018	13-7016
G'	IL-12	ebioscience	14-7128	13-7129
H'	MMP9	R&D Systems	DY911 (KIT)	
K'	VEGF R2	R&D Systems	DY357 (KIT)	
L'	Serpin E1	R&D Systems	DY1786 (KIT)	

Table 4.4 The fitted classification function of the cohort 2 determined at the end of Cycle 1 treatment.

	b_0	b_{IL2}	b_{VEGF}	b_{TGFb1}	b_{C3}	b_{IL1b}	b_{IL12}	b_{MMP9}	b_{VEGFR2}	$b_{SerpinE1}$
F(R)	1.21	-0.0561	-0.104	-0.0838	-0.0513	-0.109	-0.0902	-0.114	-0.0994	-0.0928
F(NR)	-0.208	0.0561	0.104	0.0838	0.0513	0.109	0.0902	0.114	0.0994	0.0928

Table 4.5 Confusion matrix for the cohort 2 group at the end of Cycle 1 treatment.

Patient category	Predicted responder	Predicted non-responder	Total	% correct
Responder	12	5	17	70.6%
Non-responder	5	12	17	70.6%
Total	17	17	34	70.6%

Table 4.6 Confusion matrix for the cohort 2 group at the end of Cycle 2 treatment based on the model's prediction.

Patient category	Predicted responder	Predicted non-responder	Total	% correct
Responder	6	2	8	75.0%
Non-responder	3	6	9	66.7%
Total	9	8	17	70.6%

Table 4.7 The fitted classification function of the cohort 1 determined at end of Cycle 1 treatment.

	b_0	b_{IL2}	b_{VEGF}	b_{TGFb1}	b_{C3}	b_{IL1b}	b_{IL12}	b_{MMP9}	b_{VEGFR2}	$b_{SerpinE1}$
F(R)	0.160	-0.337	0.0344	0.0932	-0.143	-0.0977	0.223	-0.0274	0.144	0.216
F(NR)	0.840	0.337	-0.0344	-0.0932	0.143	0.0977	-0.223	0.0274	-0.144	-0.216

Table 4.8 Confusion matrix for Cohort 1 at the end of Cycle 1 treatment.

Patient category	Predicted responder	Predicted non-responder	Total	% correct
Responder	1	2	3	33.3%
Non-responder	0	5	5	100%
Total	1	7	8	72.5%

Table 4.9 Confusion matrix for the cohort 1 at the end of Cycle 2 treatment base on the model prediction.

Patient category	Predicted responder	Predicted non-responder	Total	% correct
Responder	2	1	3	66.7%
Non-responder	0	3	3	100%
Total	2	4	6	83.3%

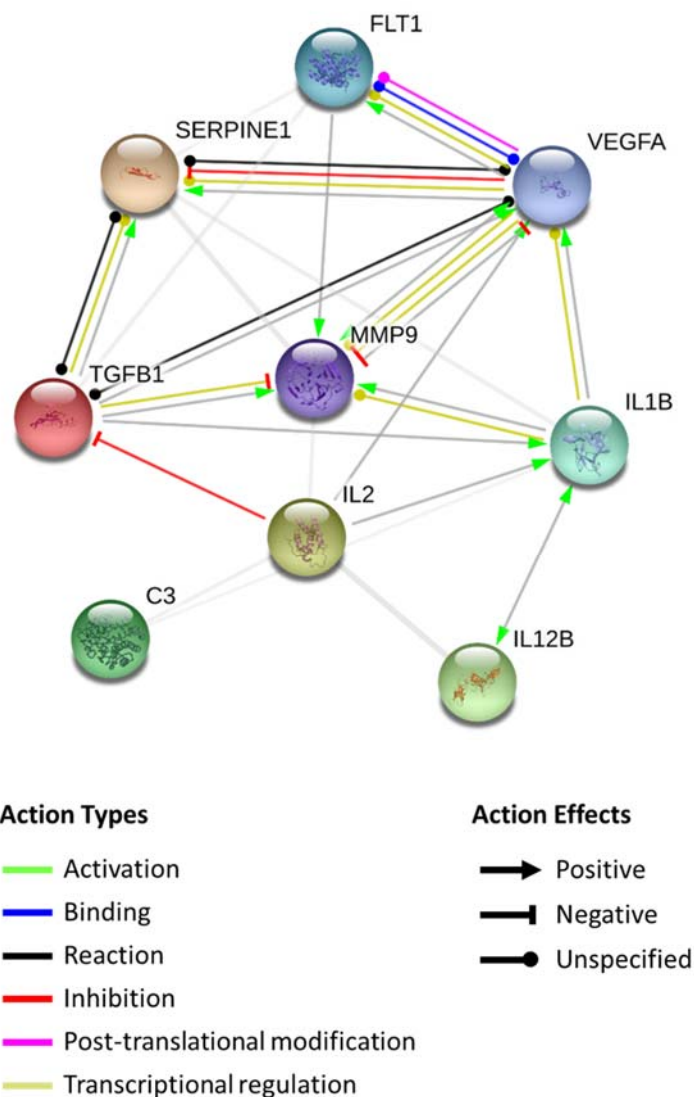## 4.7 Appendix B: Supplementary figures

Figure 4.8 Protein-protein interaction map of 9 protein markers measured in this study. STRING (Search Tool for the Retrieval of Interacting Genes/Proteins), a web-based open source software, was used to map out these interactions (https://string-db.org/). Most of the proteins are highly related with each other which causes the multi-collinearity in the data set. (FLT1, Fms-related tyrosine kinase 1, i.e. vascular endothelial growth factor/vascular permeability factor receptor; IL12B, IL-12 p40).
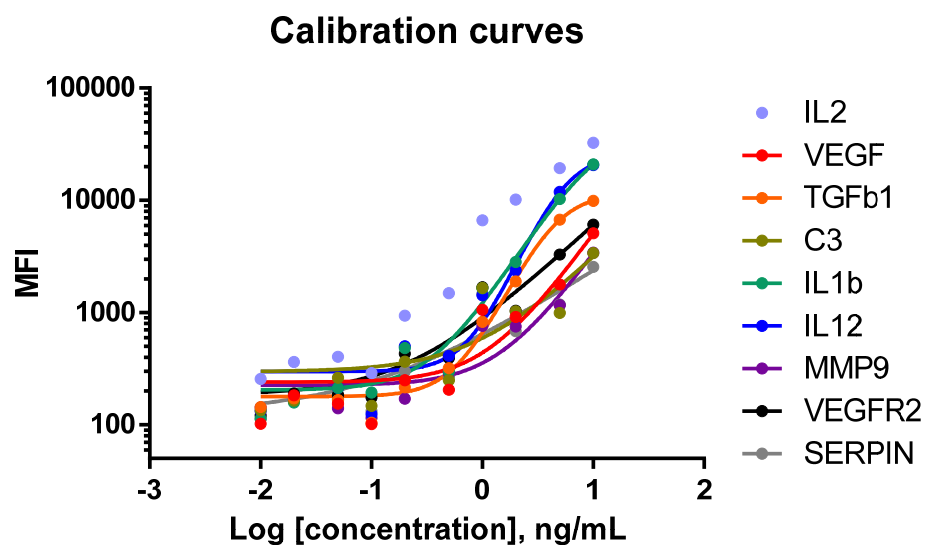
Figure 4.9 Calibration curves. A four-parameter logistic model was fitted to all the proteins markers except IL-2.
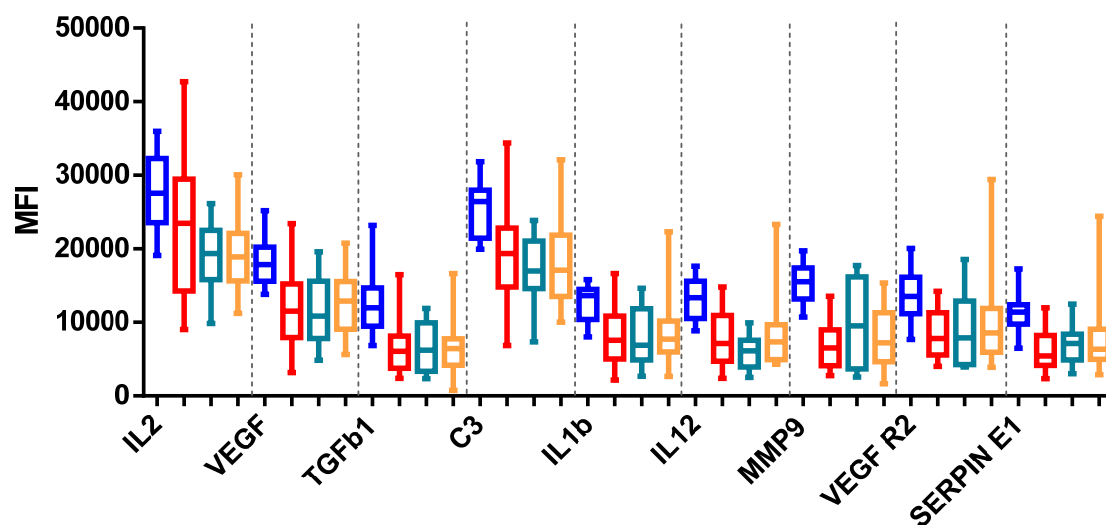

Figure 4.10 Box plot of the measured raw protein levels during the drug treatment. Data were classified by cohort and drug response. Cohort 1 is shown in blue (responders) and red (non-responders) and cohort 2 are shown in dark green (responders) and orange (non-responders).
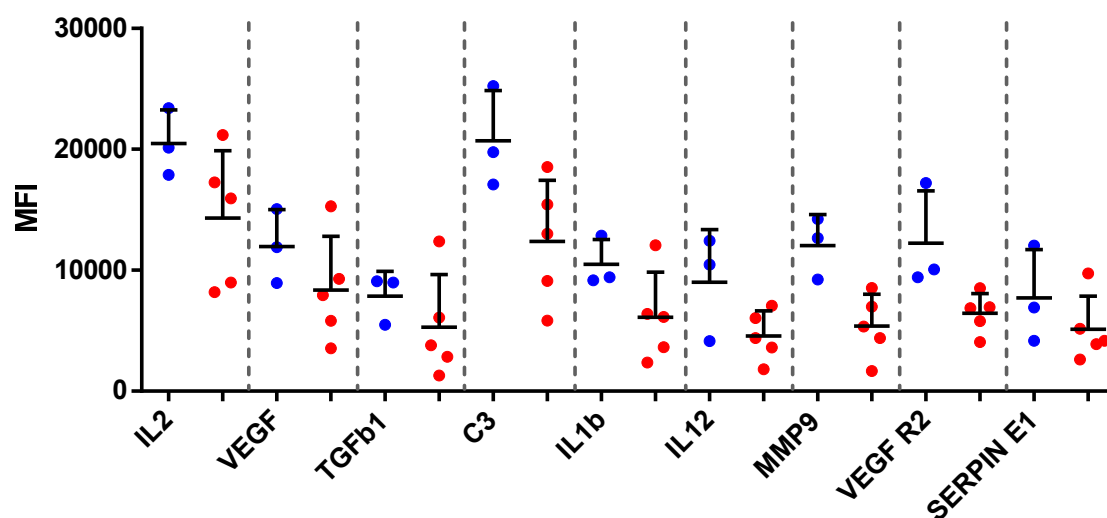
Figure 4.11 Raw protein levels of cohort 1 in pre-treatment. Samples were classified by the drug responses after Cycle 1 treatment. Due to small sample size, no statistical test was performed between responders (blue, n=3) and non-responders (red, n=5). Averages and standard deviations were shown.
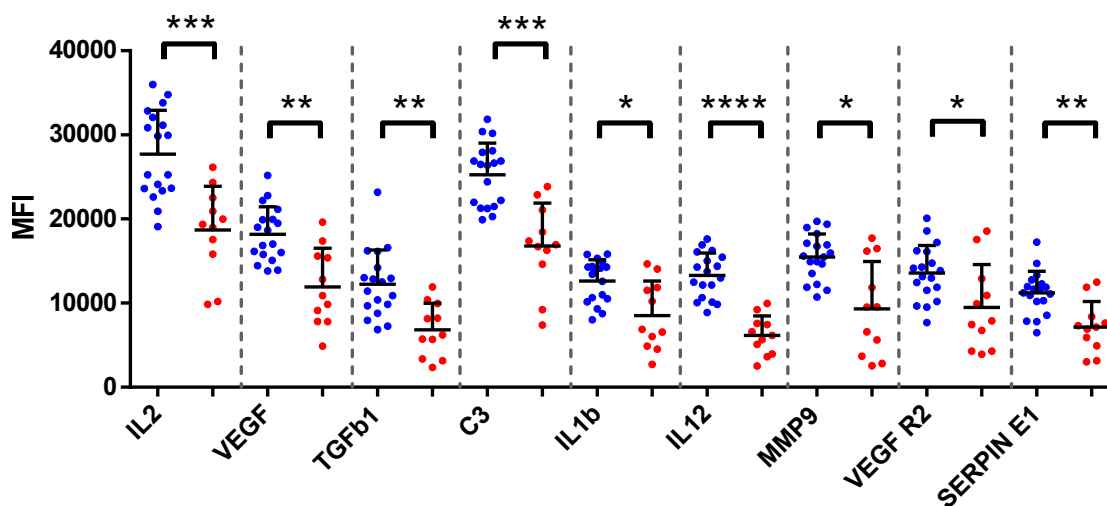

Figure 4.12 Cohort 1 raw protein levels during the treatment. Responders (blue, n=18) had higher levels of all the measured proteins than non-responders (red, n=11). (*, p<0.05; **, p<0.005; ***, p<0.0005; **** p<0.0001). Averages and standard deviations were shown.
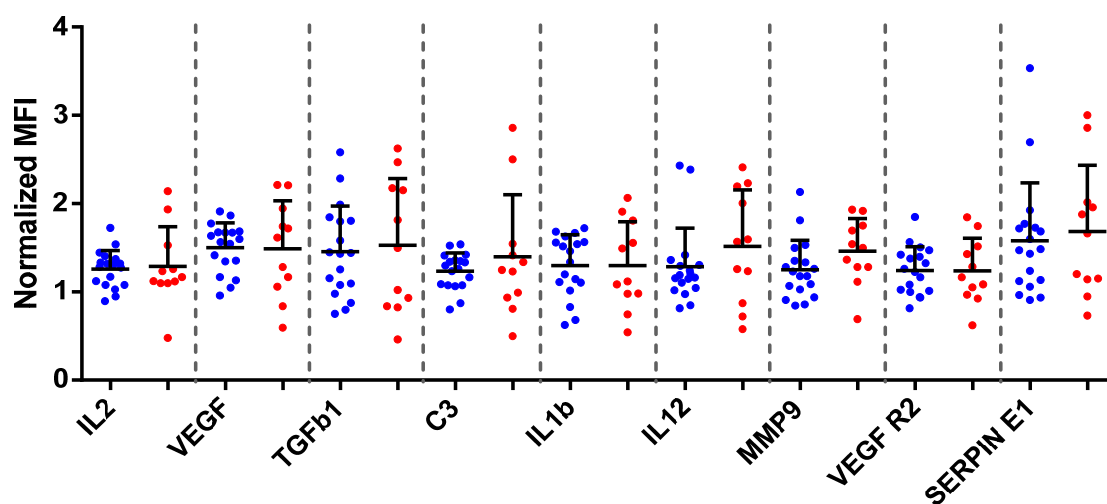
Figure 4.13 Cohort 1 normalized protein levels during the treatment. Protein levels in pre-treatment was used for the normalization. All the normalized values of responders (blue, n=18) and non-responders (red, n=11) were not different with statistical significance. Averages and standard deviations were shown.
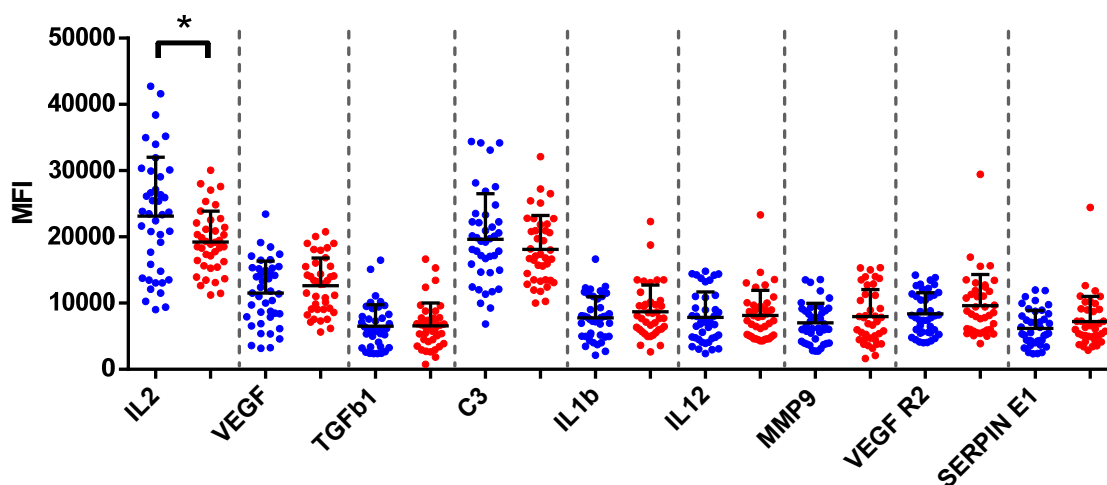

Figure 4.14 Cohort 2 raw protein levels during the treatment. Responders (blue, n=41) had higher level of IL-2 than non-responders (red, n=39). (*, $p<0.05$). Averages and standard deviations were shown.
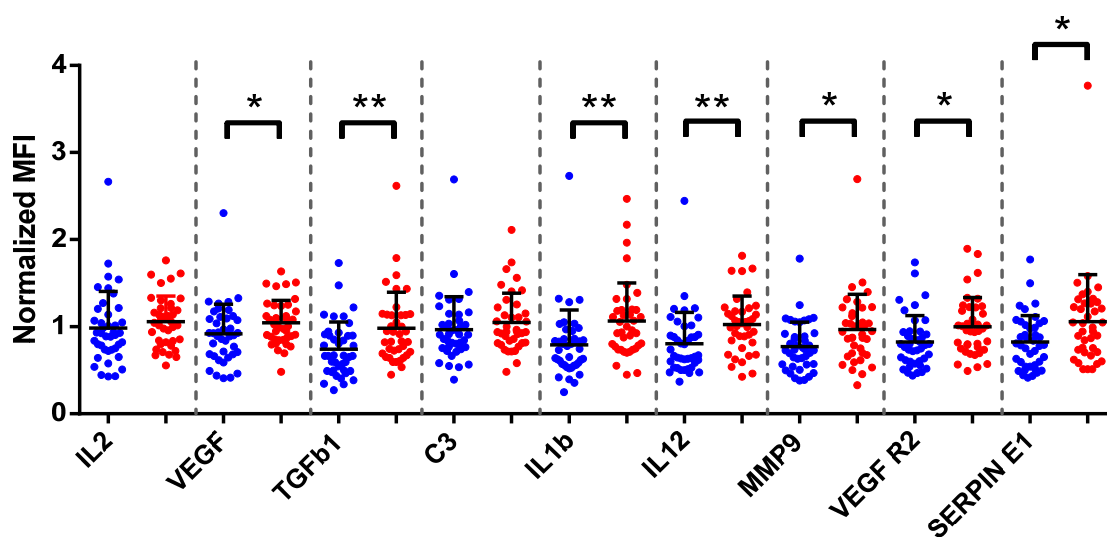
Figure 4.15 Cohort 2 normalized protein levels during the treatment. Protein levels in pre-treatment was used for the normalization. The normalized values of VEGF, TGF β1, IL-1β, IL-12, MMP9, VEGF R2, and Serpin E1 levels were higher in responders (blue, n=41) than non-responders (red, n=39). (*, p<0.05; **, p<0.005). Averages and standard deviations were shown.

Chapter 5

A barcoded rapid assay platform for the efficient evaluation of epitope-targeted binders against KRas protein

5.1 Introduction

Protein-catalyzed capture agents (PCCs) are a class of synthetic antibody surrogates that have been demonstrated, for a number of protein targets, to mimic the epitope targeting ability and high avidity of monoclonal antibodies.[1] Further, PCCs can be engineered to have combined properties that are difficult to achieve for biologics, such as combinations of physical and biological stability, *in vitro* or *in vivo* target recognition, and, in one example, cell penetration.[2] State-of-the-art PCCs are identified by carrying out an *in situ* click screen[3] of a synthetic, strategically modified polypeptide fragment (the synthetic epitope, or SynEp) of the protein target against a synthetic one-bead-one compound (OBOC) library of macrocyclic peptides. The comprehensive OBOC library typically contains the roughly two million sequences that result from using all combinations of an 18-20 amino acid basis set to construct a variable 5-mer region.

PCC leads are identified through a single generation screen that will typically yield on the order of five to ten hits. Once identified, those hit peptides are tested for binding to the full-length protein, often in various levels of serum background and under different

blocking conditions. These assays represent a limiting factor in the production of high quality PCCs. They are carried out on 96-well plates using a sandwich Enzyme-Linked Immunosorbent Assay (ELISA) format, and may involve running 50 to 100 multi-point assays in series. In addition to being laborious, the assays also consume significant amounts of the chemical and biological reagents used in the assays. Finding a more efficient solution to carrying out such assays might be useful for the production of other artificial antibody-type ligands, such as other classes of peptides or aptamers.[4–6]
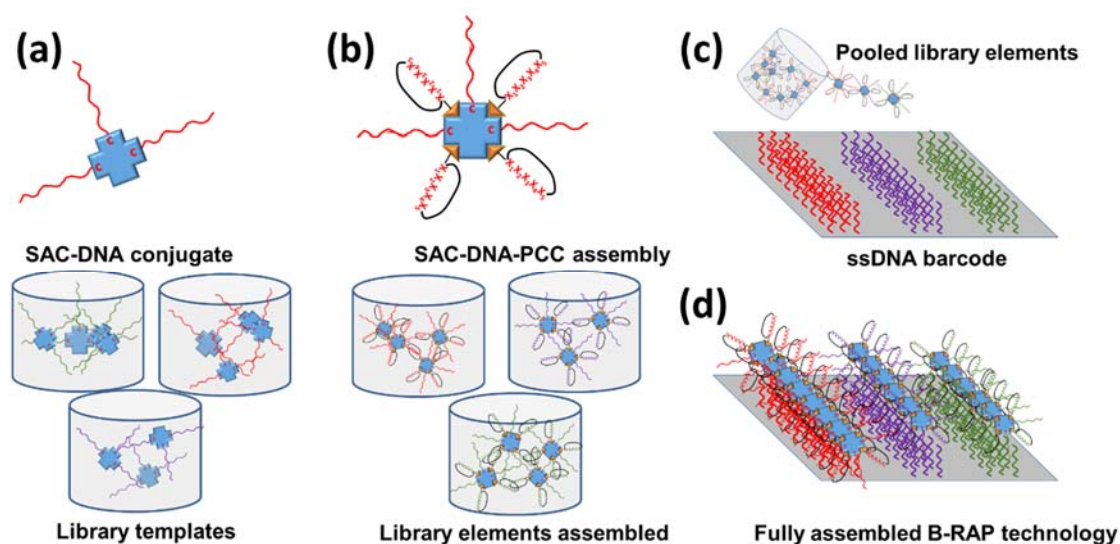

Figure 5.1 Overview of the B-RAP Technology. (a) The individual SAC-DNA conjugates (b) The biotinylated PCC ligands are added to the SAC-DNAs and allowed to complex. (c) The individual SAC-DNA-ligand solutions are pooled and the cocktail is added to individual microwells on the DNA barcode. (d) The SAC-DNA-ligand conjugates self-assemble with the DNA barcode to produce a fully assembled B-RAP assay.

To address this challenge we report here on the barcoded rapid assay platform (B-RAP), which is a microchip platform designed so that the entire set of candidate PCC ligands may be rapidly evaluated in parallel, using minimal quantities of reagents (Figure 5.1). Simultaneous testing of all PCCs under identical environments means that all assays

are subject to the same uncertainties, thus permitting a direct comparison of the EC_{50} values for the entire set of hit peptides. The B-RAP technology draws from the Nucleic Acid Cell Sorting (NACS)[7] and DNA-Encoded Antibody Libraries (DEAL) methods.[8–11] The B-RAP process starts with a microscope slide that is flow-patterned with a distinct set of ssDNA oligomers. PCC candidates are prepared with a biotin label, and then assembled onto cysteine-modified streptavidin (SAC) scaffolds that have been labeled with complementary ssDNA oligomers.[12–14] Once assembled, these reagents are combined into a cocktail, and assembled onto specific stripes of the barcode pattern using DNA hybridization.[15] The microchip surface itself is partitioned into microliter volume wells, each of which contains multiple copies of the full barcode. The B-RAP technology can be used to simultaneously assay a full panel of candidate PCCs over a range of target protein concentrations (or other conditions), so that the EC_{50} binding values for each candidate PCC are simultaneously measured.

Here we report on the use of the B-RAP technology to analyze the results from an epitope targeted *in situ* click screen against the Kirsten rat sarcoma (KRas) protein.[16] The oncoprotein variants of KRas are implicated in driving ~20-25% of all human cancers including almost all pancreatic cancers.[17] Ras proteins have largely evaded targeting by traditional therapeutic techniques,[18–21] but recent work has shown that specific mutant isoforms may be targetable.[22] We targeted conserved epitopes denoted Switch I (aa 25-40) and Switch II (aa 56-75), which are known to allosterically influence KRas activity.[23]

5.2 Materials and methods[24]

5.2.1 Preparation of the barcode rapid assay platform

We utilized DNA flow-patterned barcode chips, biotinylated peptides, and SAC-DNA to assemble a miniaturized barcode of candidate PCCs for testing in a surface Immunofluorescent assay (IFA). Microfluidic flow patterning of 50 μm wide, 100 μm pitch ssDNA barcodes starts with adhering a polydimethylsiloxane (PDMS) microchannel mold onto a poly-L-lysine (PLL) coated glass microscope slide (Figure 5.4a, Appendix A). Reagents were introduced into the microchannels using a pins and tubing-free flow system that greatly simplified the preparation of barcoded microchips relative to previous protocols (Figure 5.5, Table 5.2, Appendix A and B).[25,26] The PDMS mold was patterned with microwells at each microchannel inlet (Figure 5.4a (i,ii), Supporting Information). Reagents (3-5 μL) are micropipetted into the microwells, and then two machined acrylic plates are clamped across the top and bottom of the inlet region. The top acrylic plate contains a cavity that encompasses all inlet microwells. Thus cavity is pressurized to fill the microchannels in about 20 minutes (Figure 5.5b, Appendix A). The design tolerates higher inlet pressures, which enables the use of narrower dimension microchannels than used here. Initially 3μL of PLL (0.1% (^{w}/$_w$) in H_2O) is flow patterned and dried overnight before flow 5μL of 300 μM of each ssDNA (Table 5.3, Appendix B) with 2mM bis(sulfosuccinimidyl)suberate) (BS3) crosslinker. Some 20-25 DNA barcoded chips are readily prepared in parallel using this approach (Figure 5.4c, Appendix A). The edge of the barcode is used to validate the coverage density and uniformity of the molecular patterns

using Cy3-labeled complementary ssDNA (Figure 5.5 and 5.6, Appendix A). Once validated, the barcoded slides are vacuum-sealed for up to six months storage before use.

The second component of the B-RAP technology that is independent of the specific identities of any PCC candidates to be tested, is the library of DNA-Encoded Streptavidin (SAC-DNA) constructs used to assemble individual biotinylated PCC candidates onto specific barcode lanes. The SAC protein was conjugated with ssDNA complementary to the barcode DNA oligomers (Table 5.3, Appendix B). This was done using N-succinimidly-4-formylbenzaldehyde (S-4FB) and maleimide 6-hydrazino-nicotinamide (MHPH), followed by fast protein liquid chromatography (FPLC) purification (Figure 5.7, Appendix A).

The performance of the library of fifteen SAC-DNAs[15,27] was evaluated by hybridizing library elements onto the flow patterned ssDNA barcodes. The barcodes were then incubated with varying amounts of the fluorophore probe biotin-A_{20}-Cy3 (Biotin*, 50-400nM) (Figure 5.8a, Appendix A). The resulting surface fluorescence was measured and compared to the fluorescence signal from the bottom edge barcode validation region (Figure 5.8a, Appendix A). The fluorescent output at 532 nm (F_{532}) of the captured biotinylated probe was lower than the F_{532} of the validation region (45 to 65k). This is likely a result of the large size of the SAC protein relative to the Cy3 fluorophore. A minimum F_{532} value of 25k was set as indicative of a functionally active SAC-DNA conjugate.

5.2.2 KRas protein expression and purification

The KRas protein isoform 4B was expressed from transformed BL21(D3) *E. coli* cells as a His$_6$-tagged protein[28] and purified by FPLC using a Ni-NTA resin (Figure 5.9, Appendix A). The fractions with pure KRas were dialyzed into tris-buffered saline (TBS, pH=7.4), aliquotted, and stored at -80.0 °C until needed.

5.2.3 Preparation of Switch I and Switch II SynEps and scrambled SynEps

The synthetic epitopes (SynEps 1 and 2) were 11-12 amino acid polypeptides with sequences extracted from the allosteric switch regions of Kras (Figure 5.2a and Table 5.4, Appendix B). The SynEp1 differs from the wild-type sequence as it is missing a valine residue. An azido click handle was added via substituting residue-similar azido-amino acids, as shown in Figure 2A. Rearranged version of the SynEps were also prepared, and used in a pre-screen step to remove possible interferents. All epitopes were synthesized on biotin Novatag resin and purified using semi-preparative high performance liquid chromatography (HPLC) (Figure 5.10a, 5.11a, 5.12a, 5.13a, Appendix A). The appropriate fractions were identified using matrix-assisted laser desorption ionization time-of-flight mass spectrometry (MALDI-TOF MS) (Figure 5.10b, 5.11b, 5.12b, 5.13b, Appendix A). Each SynEp was dissolved in DMSO, quantified using a Nanodrop 2000 spectrophotometer, and stored at 4 °C.

5.2.4 Library preparation and in-situ library click screen

A comprehensive OBOC library of 5-mer variable peptide macrocycles, using an 18 amino acid basis set, was prepared as previously reported.[1] The macrocyclic peptides

are closed with a 1,4 triazole using Cu(I) catalyzed click chemistry. These macrocycles are designed to present a propargylglycine click handle (Appendix C and D). The *in situ* library click screen was a dual SynEp version of a previously reported protocol.[1] After removing the beads that bound to the scrambled SynEps during a pre-clear screen the remaining library was incubated with both SynEp1 and SynEp2 (Appendix C and D). After incubating with an anti-biotin capture and alkaline-phosphatase conjugated 2° antibody, the hit beads were identified by their deep purple color. Hit beads were stored at RT in 0.1 M hydrochloric acid until sequenced. For sequencing, hit beads were decolorized in N-methyl pyrrolidine (NMP), and sequenced by Edman degradation (Table 5.4, Appendix B). Hit compounds were then scaled up on biotin Novatag resin following previously established protocols,[1] purified, and then stored at 4 °C until ready for use.

5.2.5 Surface immunofluorescent assays on the barcoded rapid assay platform

The barcode patterned microchip surface was partitioned into 16 individual microwells using a molded PDMS template. Individual biotinylated PCC candidates were complexed to specific SAC-DNA conjugates, combined into a cocktail, and then self-assembled, via DNA hybridization, onto designated barcode stripes (Figure 5.1). Incubation with a specific concentration of the target protein preceded incubation with a 1° capture antibody (ab) and then a fluorophore-conjugated 2° detection ab. During assay execution, each well represents a different target concentration or assay condition.

5.3 Results and discussion

5.3.1 Optimizing B-RAP technology assay conditions

Bead[a]	Ligand	X1	X2	X3	X4	X5
1	L1[b]	H	G	I	V	G
2	L2	E	G	V	P	V
	L3[b]	G	E	V	V	P
3	L4[b]	V	E	V	P	Y
	L5[b]	V	E	V	Y	P
4	L6	V	T	V	P	Y
	L7[b]	V	Q	V	P	Y
5	L8	T	D	N	F	Y
	L9[b]	Q	D	N	F	Y

SynEp1: FVDEYD[P→⁴⁻ᴺ³P]TIEDSY (28-40)
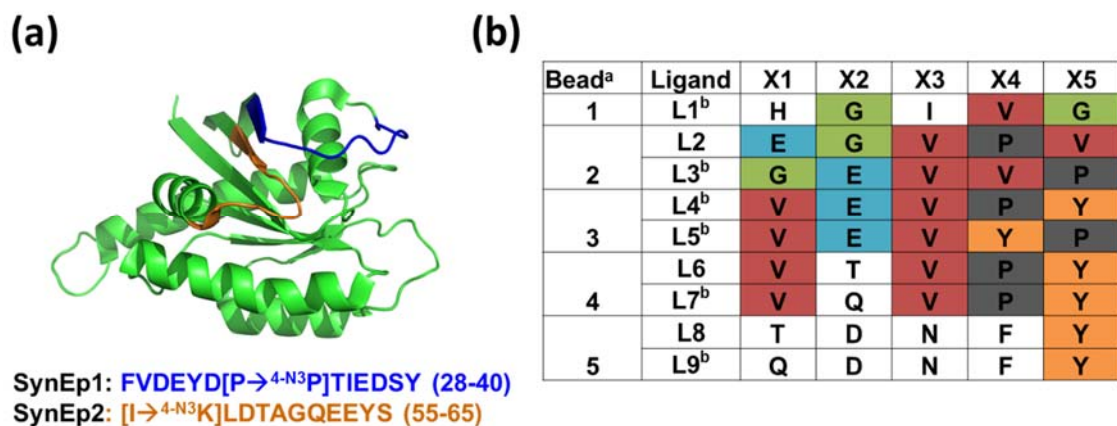SynEp2: [I→⁴⁻ᴺ³K]LDTAGQEEYS (55-65)

Figure 5.2 Identification of SynEps for the dual epitope *in-situ* click screen, and the resulting PCC ligand hits from the library screen. (a) The regions of the allosteric KRas switches that comprise the SynEps used for the dual-epitope in-situ library click screen. The crystal structure is a ray-trace from pdb file 4dst. (b) The sequences of the PCC ligands resulting from the dual-epitope screen. *[a]Similar sequences are reported for a bead due to the nature of certain amino acids co-eluting on an Edman degradation trace or the size of the peaks preventing determination of which residue came first. [b]These ligands had two fractions with the correct mass after HPLC purification and both were tested on the platform.*

The *in situ* click screen against the Switch I and II KRas SynEps yielded five beads from which nine candidate sequences were determined (Figure 5.2b). Biotinylated candidate ligands were then tested using a single-point immunofluorescence assay on the B-RAP platform (Figure 5.15, Appendix A) in order to identify appropriate blocking conditions. Modification of the protein incubation solution to include the nonionic surfactant Polysorbate 20 (Tween20) was found to minimize non-specific binding between the KRas protein and the unmodified PLL surface.

Running the laser at full power resulted in over-saturation of the scanned barcode so a test of different power settings was conducted to identify the ideal setting. The ideal power setting would avoid early saturation in order to utilize the entire dynamic range of the detector (0-65.5k) when generating binding curves. A laser power setting of 40% was settled on after testing a variety of power settings (10-80%).

5.3.2 Validation of the B-RAP technology

Following optimization of the assay conditions the B-RAP technology was subjected to statistical tests to assess the variance in assay results measured within an individual microwell, between microwells on the same chip, and between different microchips. The average percent coefficient of variation (%CV) seen along an individual barcode stripe in the wells above background (500 nM to 400 μM KRas) was ~15%. The %CV between wells on the same microchip under identical conditions was ~9%. Each microwell contains between two to three full copies of the DNA barcode. For the same barcode lane in different full barcode sets in the same microwell, the fluorescence output was measured to have an average %CV of ~14% (Figure 5.16a, Appendix A). The global average %CV for identical barcode lanes between two assays run in parallel by different users was ~18% with an average %CV of ~15% for the 1 μM to 400 μM range of KRas protein (Figure 5.16b and 5.16c, Appendix A). Additionally, the average fluorescence output (F_{635}) from a full line scan of the same area extracted using a discrete ten-block data extraction was compared to the average F_{635} resulting from the data-block extraction, and the values from the full-line scan were contained within two standard deviations of the data-block extraction's average F_{635} (Figure 5.17, Appendix A). As a result, we concluded

that the variance in assay output on the same barcode and between different barcodes was low.

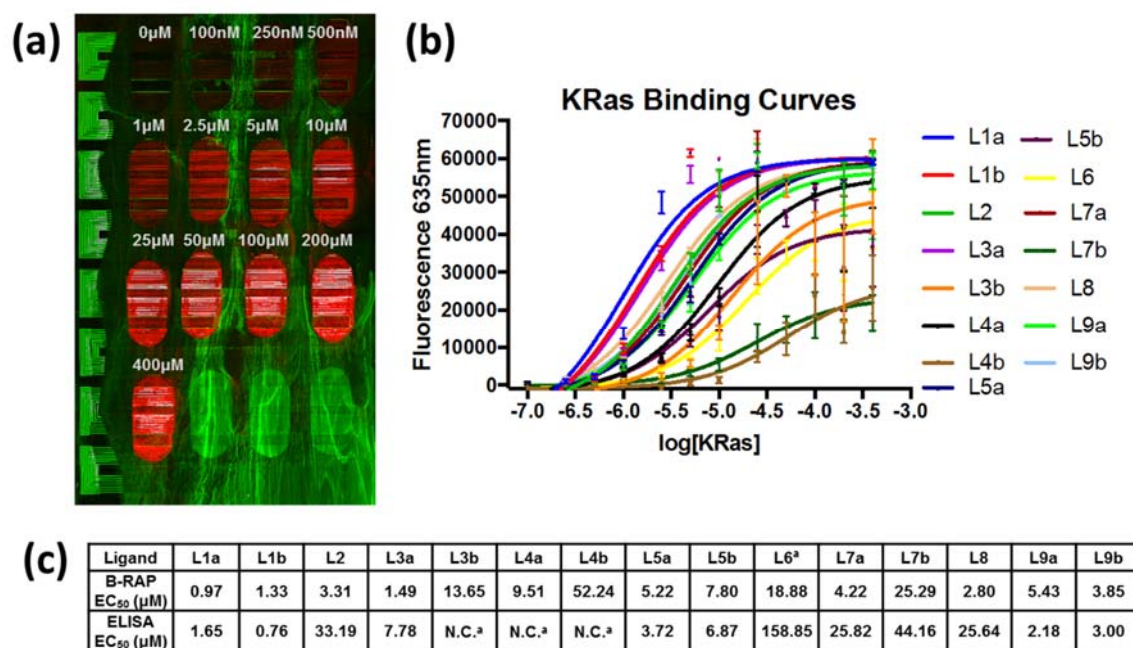### 5.3.3 Measuring the EC$_{50}$ of the allosteric binding PCC ligands

Ligand	L1a	L1b	L2	L3a	L3b	L4a	L4b	L5a	L5b	L6[a]	L7a	L7b	L8	L9a	L9b
B-RAP EC$_{50}$ (µM)	0.97	1.33	3.31	1.49	13.65	9.51	52.24	5.22	7.80	18.88	4.22	25.29	2.80	5.43	3.85
ELISA EC$_{50}$ (µM)	1.65	0.76	33.19	7.78	N.C.[a]	N.C.[a]	N.C.[a]	3.72	6.87	158.85	25.82	44.16	25.64	2.18	3.00

Figure 5.3 Full binding curves for L1-L9 and the corresponding EC$_{50}$ values. (a) The raw scan of the barcode after running the KRas protein binding curves. (b) The worked up graphs for the allosteric PCC ligands. (c) The EC50 values derived from the B-RAP technology and the multi-well ELISA technology. *[a]Not calculated due to non-saturation of graph.*

After characterizing the B-RAP technology, we used the chip to record, in parallel, full binding curves for 15 candidate KRas ligands (Figure 5.3) and determined the EC$_{50}$ values for each ligand (Figure 5.3c). These measurements were comprised of a 13-point concentration series, with each point collected in decaplicate. The EC$_{50}$ values enabled the ranking of the ligands, and the best binders were identified to be L1, L2, and L8 respectively. Some of the EC$_{50}$ values between the B-RAP technology and multi-well ELISA assays diverge significantly (Figure 3c), with the ELISA data consistently fitting to

higher EC50 values. This likely arises from two reasons. First, the ELISA assays are absorbance measurements, and thus have a significantly smaller dynamic range then the B-RAP fluorescent assays. Second, the ELISA assays use enzymatic amplification to generate a signal, while the B-RAP assays use no amplification. These two factors mean that the B-RAP assays are characterized by a higher signal to noise. This is especially true for micromolar binders, since assays of such relatively weak binders are of typically lower signal-to-noise. The true amino acid sequences for each hit peptide were distinguished from the artifact sequences that arose from uncertainties in the Edman degradation sequencing. The true hits are identified as L1, L2, L5, L7, and L8.

5.4 Conclusion

In summary we report on the development and validation of a barcode rapid assay microchip platform for the simultaneous evaluation of fifteen PCC agents in up to sixteen unique assay conditions. A miniaturized Biotin* binding assay was also developed to verify the biotin binding ability of the DESL set. The B-RAP technology was used to identify the best allosteric KRAS binders from a pool of ligands derived from a dual SynEp library click screen in a single day. The savings in terms of time and material with the significant gain in data points advances our program for rapidly developing PCC agents against proteins of therapeutic interest (Table 5.1, Appendix A). The tool permits a more than 10-fold time in savings and a more than 100-fold reduction in biological reagents relative to traditional multi-well plate assays. Current efforts involve advancing the identified best binders through a series of medicinal chemistry optimizations with the intent of linking the

best allosteric ligands to PCC agents developed against the *mutated* [G12D]KRas protein. Additionally, efforts are ongoing to develop conditions for running a two-color fluorescent assay with B-RAP. The ability to use a pair of orthogonal fluorescent-tagged antibodies would allow for a competition pull-down assay in order to assess the difference in affinity for two structurally related proteins.

5.5 References

(1)   Das, S.; Nag, A.; Liang, J.; Bunck, D. N.; Umeda, A.; Farrow, B.; Coppock, M. B.; Sarkes, D. A.; Finch, A. S.; Agnew, H. D.; Pitram, S.; Lai, B.; Yu, M. B.; Museth, A. K.; Deyle, K. M.; Lepe, B.; Rodriguez-Rivera, F. P.; McCarthy, A.; Alvarez-Villalonga, B.; Chen, A.; Heath, J.; Stratis-Cullum, D. N.; Heath, J. R. *Angew. Chemie Int. Ed.* **2015**, *54* (45), 13219.

(2)   Farrow, B.; Wong, M.; Malette, J.; Lai, B.; Deyle, K. M.; Das, S.; Nag, A.; Agnew, H. D.; Heath, J. R. *Angew. Chemie Int. Ed.* **2015**, *54* (24), 7114.

(3)   Agnew, H. D.; Rohde, R. D.; Millward, S. W.; Nag, A.; Yeo, W. S.; Hein, J. E.; Pitram, S. M.; Abdul Ahad Tariq, V.; Burns, A. M.; Krom, R. J.; Fokin, V. V.; Barry Sharpless, K.; Heath, J. R. *Angew. Chemie Int. Ed.* **2009**, *48* (27), 4944.

(4)   Yüce, M.; Ullah, N.; Budak, H. *Analyst* **2015**, *140* (16), 5379.

(5)   Jost, C.; Plückthun, A. *Current Opinion in Structural Biology*. 2014, pp 102–112.

(6)   Mascini, M.; Palchetti, I.; Tombelli, S. *Angew. Chemie - Int. Ed.* **2012**, *51* (6),

1316.

(7)   Kwong, G. A.; Radu, C. G.; Hwang, K.; Shu, C. J.; Chao, M.; Koya, R. C.; Comin-Anduix, B.; Hadrup, S. R.; Bailey, R. C.; Witte, O. N.; Schumacher, T. N.; Ribas, A.; Heath, J. R. *J. Am. Chem. Soc.* **2009**, *131* (28), 9695.

(8)   Bailey, R. C.; Kwong, G. A.; Radu, C. G.; Witte, O. N.; Heath, J. R. *J. Am. Chem. Soc.* **2007**, *129* (7), 1959.

(9)   Boozer, C.; Ladd, J.; Chen, S.; Yu, Q.; Homola, J.; Jiang, S. *Anal. Chem.* **2004**, *76* (23), 6967.

(10)   Kozlov, I. A.; Melnyk, P. C.; Stromsborg, K. E.; Chee, M. S.; Barker, D. L.; Zhao, C. *Biopolymers* **2004**, *73* (5), 621.

(11)   Adler, M.; Wacker, R.; Booltink, E.; Manz, B.; Niemeyer, C. M. *Nat. Methods* **2005**, *2* (2).

(12)   Sano, T.; Cantor, C. R. *Proc. Natl. Acad. Sci.* **1990**, *87* (1), 142.

(13)   Reznik, G. O.; Vajda, S.; Cantor, C. R.; Sano, T. *Bioconjug. Chem.* **2001**, *12* (6), 1000.

(14)   Ramachandiran, V.; Grigoriev, V.; Lan, L.; Ravkov, E.; Mertens, S. A.; Altman, J. D. *J. Immunol. Methods* **2007**, *319* (1–2), 13.

(15)   Shin, Y. S.; Ahmad, H.; Shi, Q.; Kim, H.; Pascal, T. A.; Fan, R.; Goddard, W. A.; Heath, J. R. *ChemPhysChem* **2010**, *11* (14), 3063.

(16)   Cooper, G. M. *Science* **1982**, *217* (4562), 801.

(17)   Cox, A. D.; Fesik, S. W.; Kimmelman, A. C.; Luo, J.; Der, C. J. *Nat. Publ. Gr.* **2014**, *13*.

(18)   Whitehead, R. P.; Mccoy, S.; Macdonald, J. S.; Rivkin, S. E.; Neubauer, M. A.; Dakhil, S. R.; Lenz, H.-J.; Tanaka, M. S.; Abbruzzese, J. L. *Invest. New Drugs* **2006**, *24*, 335.

(19)   Macdonald, J. S.; Mccoy, S.; Whitehead, R. P.; Iqbal, S.; Wade Iii, J. L.; Giguere, J. K.; Abbruzzese, J. L. *Invest. New Drugs* **2005**, *23*, 485.

(20)   Winquist, E.; Moore, M. J.; Chi, K. N.; Ernst, D. S.; Hirte, H.; North, S.; Powers, J.; Walsh, W.; Boucher, T.; Patton, R.; Seymour, L. *Urol. Oncol.* **2003**, *23* (3), 143.

(21)   Sharma, S.; Kemeny, N.; Kelsen, D. P.; Ilson, D.; O 'reilly, E.; Zaknoen, S.; Baum, C.; Statkevich, P.; Hollywood, E.; Zhu, Y.; Saltz, L. B. *Ann. Oncol.* **2002**, *13*, 1067.

(22)   Ostrem, J. M.; Peters, U.; Sos, M. L.; Wells, J. A.; Shokat, K. M. *Nature* **2013**, *503*.

(23)   Hall, B. E.; Yang, S. S.; Boriack-Sjodin, P. A.; Kuriyan, J.; Bar-Sagi, D. *J. Biol. Chem.* **2001**, *276* (29), 27629.

(24)   *For detailed protocols of all experiments, see Appendices.*

(25)   Yu, J.; Zhou, J.; Sutherland, A.; Wei, W.; Shin, Y. S.; Xue, M.; Heath, J. R. *Annu. Rev. Anal. Chem.* **2014**, *7* (1), 275.

(26)   Wei, W.; Shin, Y. S.; Xue, M.; Matsutani, T.; Masui, K.; Yang, H.; Ikegami, S.;

Gu, Y.; Herrmann, K.; Johnson, D.; Ding, X.; Hwang, K.; Kim, J.; Zhou, J.; Su, Y.; Li, X.; Bonetti, B.; Chopra, R.; James, C. D.; Cavenee, W. K.; Cloughesy, T. F.; Mischel, P. S.; Heath, J. R.; Gini, B. *Cancer Cell* **2016**, *29* (4), 563.

(27)   Xue, M.; Wei, W.; Su, Y.; Kim, J.; Shin, Y. S.; Mai, W. X.; Nathanson, D. A.; Heath, J. R. *J. Am. Chem. Soc.* **2015**, *137* (12), 4066.

(28)   Boriack-Sjodin, P. A.; Margarit, S. M.; Bar-Sagi, D.; Kuriyan, J. *Nature* **1998**, *394* (6691), 337.

(29)   Pappu, R.; Ramirez-Carrozzi, V.; Sambandam, A. *Immunology* **2011**, *134* (1), 8.

(30)   Lai, B. T.; Wilson, J. A.; Malette, J.; Pitram, S. M.; Heath, J. R.; Agnew, H. D. *Submitted* **2017**.

(31)   Kozlowski, L. P. *Biol. Direct* **2016**, *11* (1), 55.

(32)   Gibbs, J. *ELISA Tech. Bull. Corning Inc. Life Sci. Kennebunk, ME* **2001**, No. 3, 1.

5.6 Appendix A: Supplementary figures
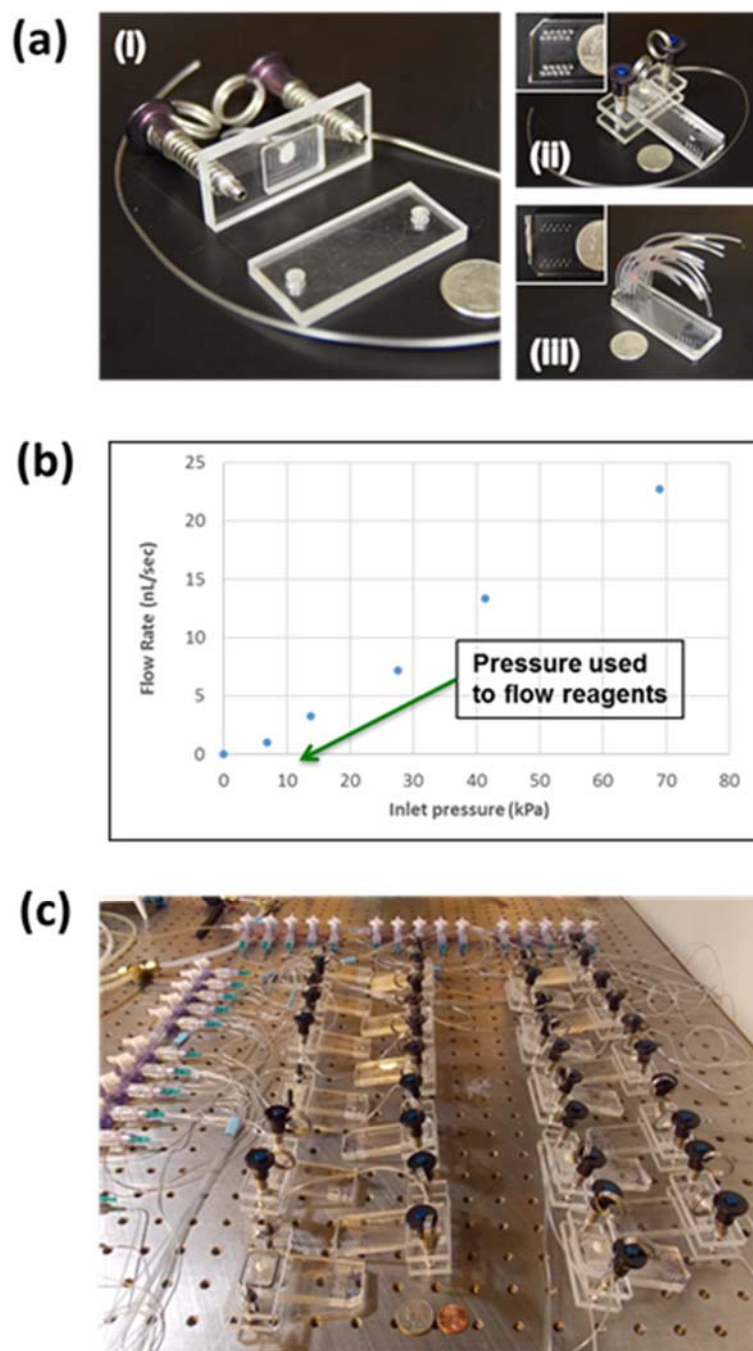
Figure 5.4 High throughput patterning of DNA barcode chips. (a) (i) Solution loading device design and flow patterning set up with (ii) the solution loading device and (iii) the pins and tubing. (b) Measured flow rates under various inlet pressures using the solution loading device. (c) Simultaneous flow patterning of 21 DNA barcode chips.

128
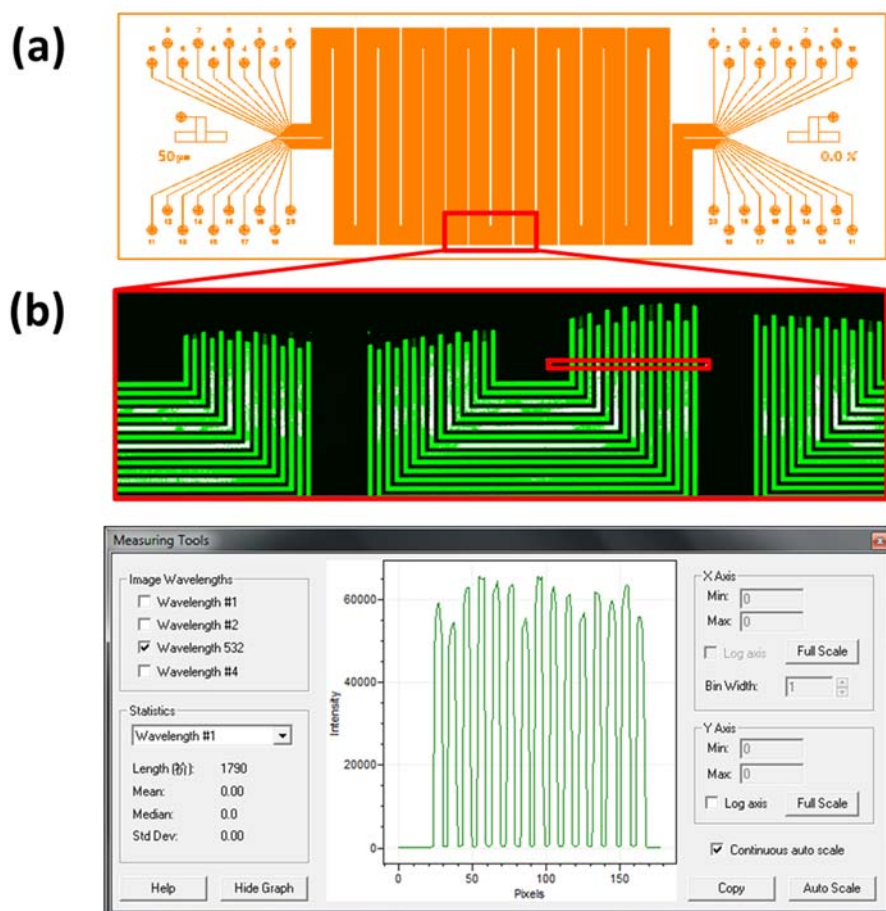
Figure 5.5 DNA barcode chip layout and validation. (a) The 50 µm barcode chip layout. (b) The Cy3-DNA validation results.
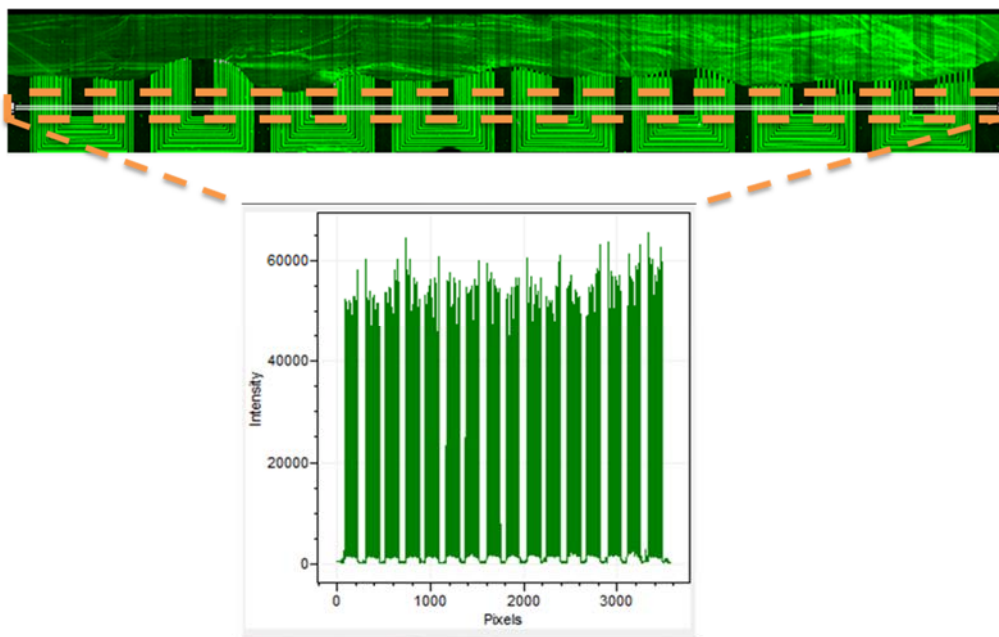
Figure 5.6 Comparison of barcode quality across an entire microchip. Measuring the barcode quality across the entire microchip reveals that all of the barcode lanes meet the minimum F635 requirement for good levels of ssDNA patterning as highlighted by the dashed line on the graph.
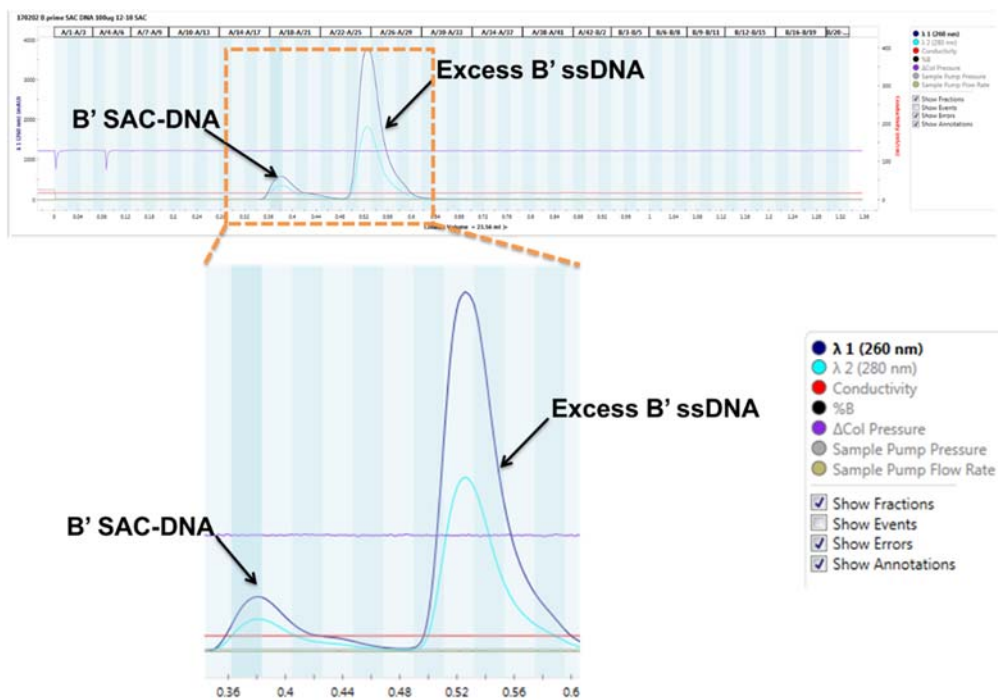
Figure 5.7 Representative SAC-DNA FPLC trace.
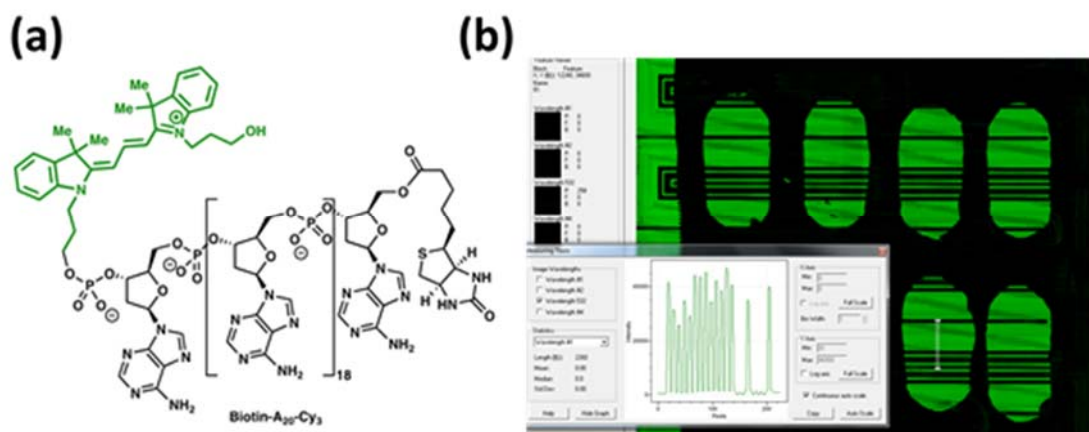
Figure 5.8 Biotin binding evaluation of the DESL set with a Biotin* probe on the barcoded rapid assay platform. (a) The biotin probe used to perform the Biotin binding affinity test for the DESL set using the B-RAP technology. (b) The output of the Biotin binding test on the DNA barcode.
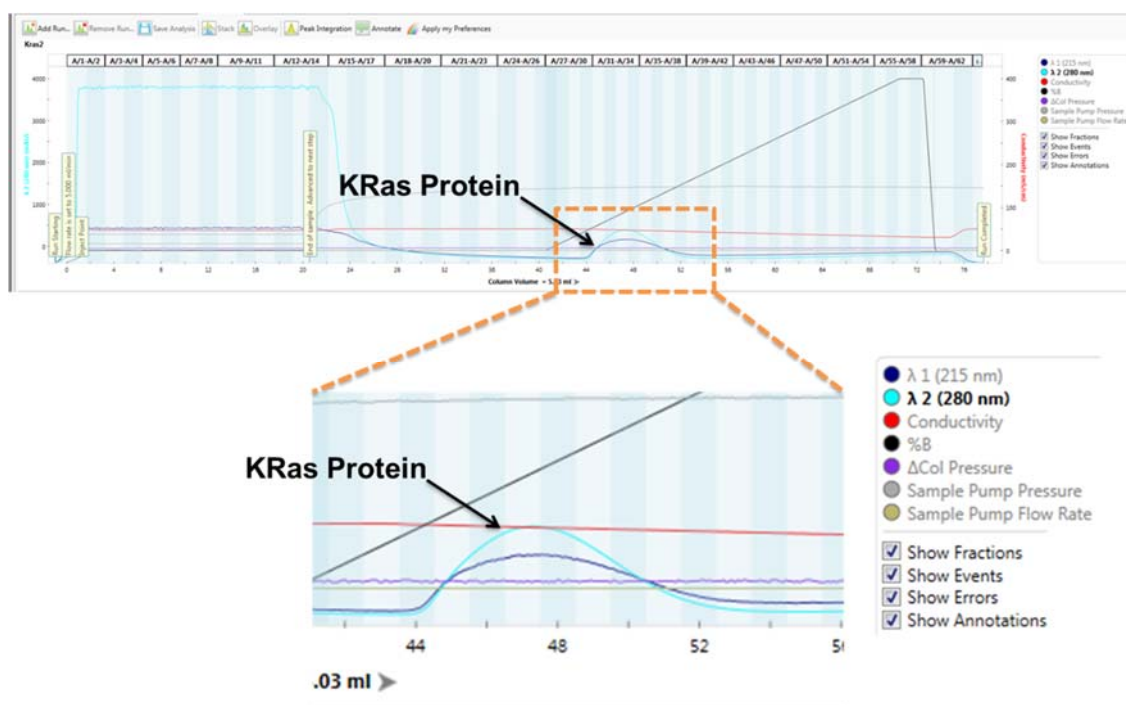
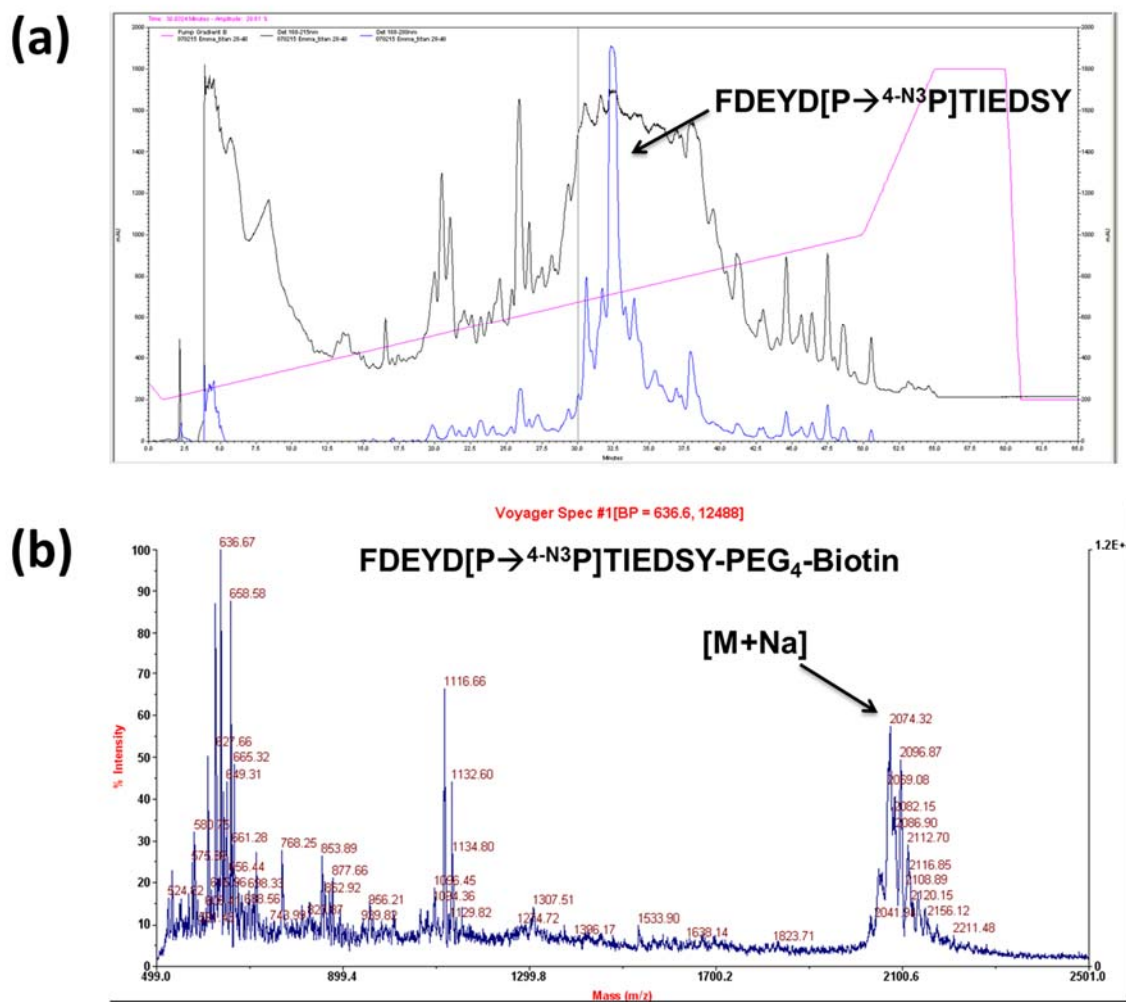**Figure 5.9** Representative KRas protein FPLC trace.
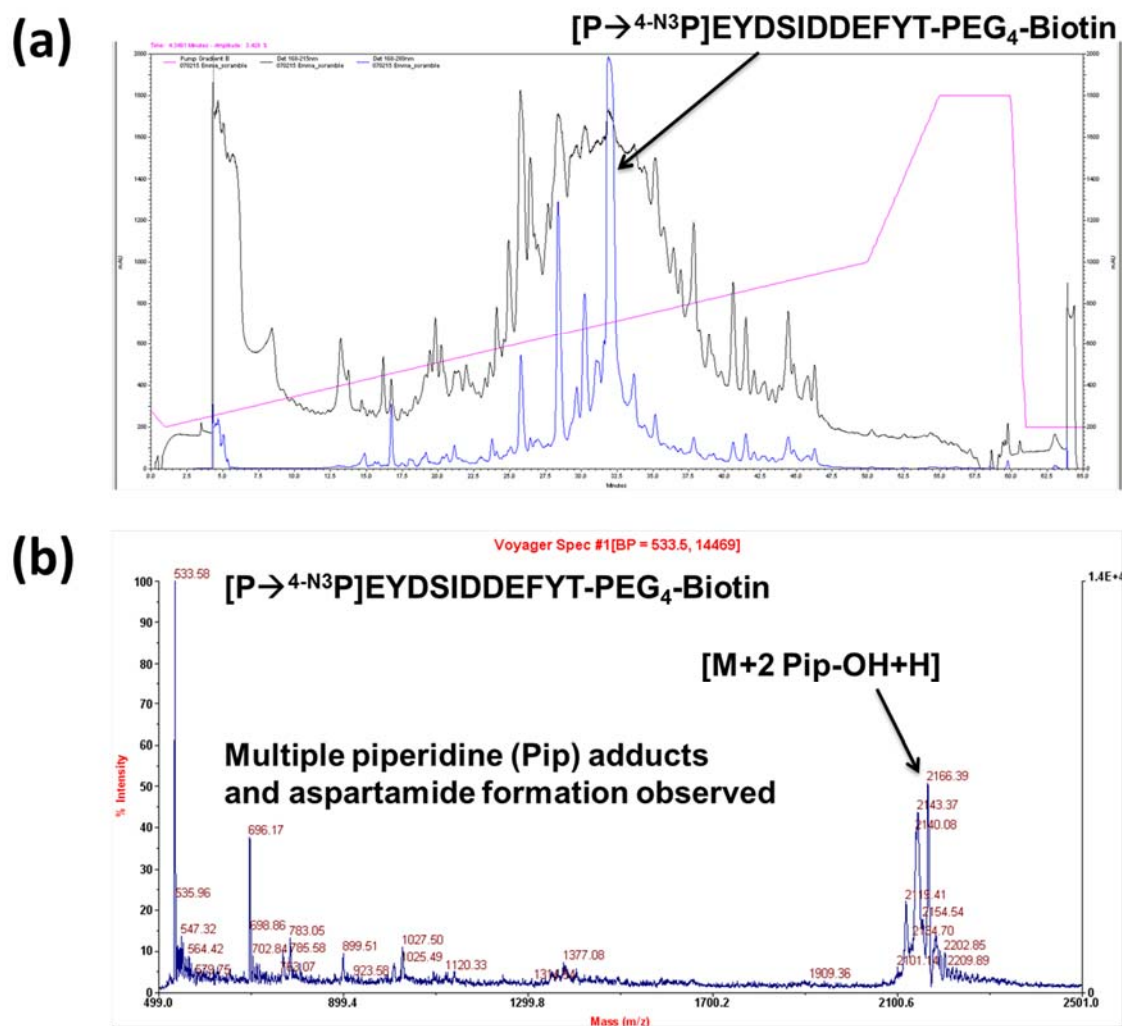
Figure 5.10 SynEp1. (a) HPLC trace (b) MALDI trace.

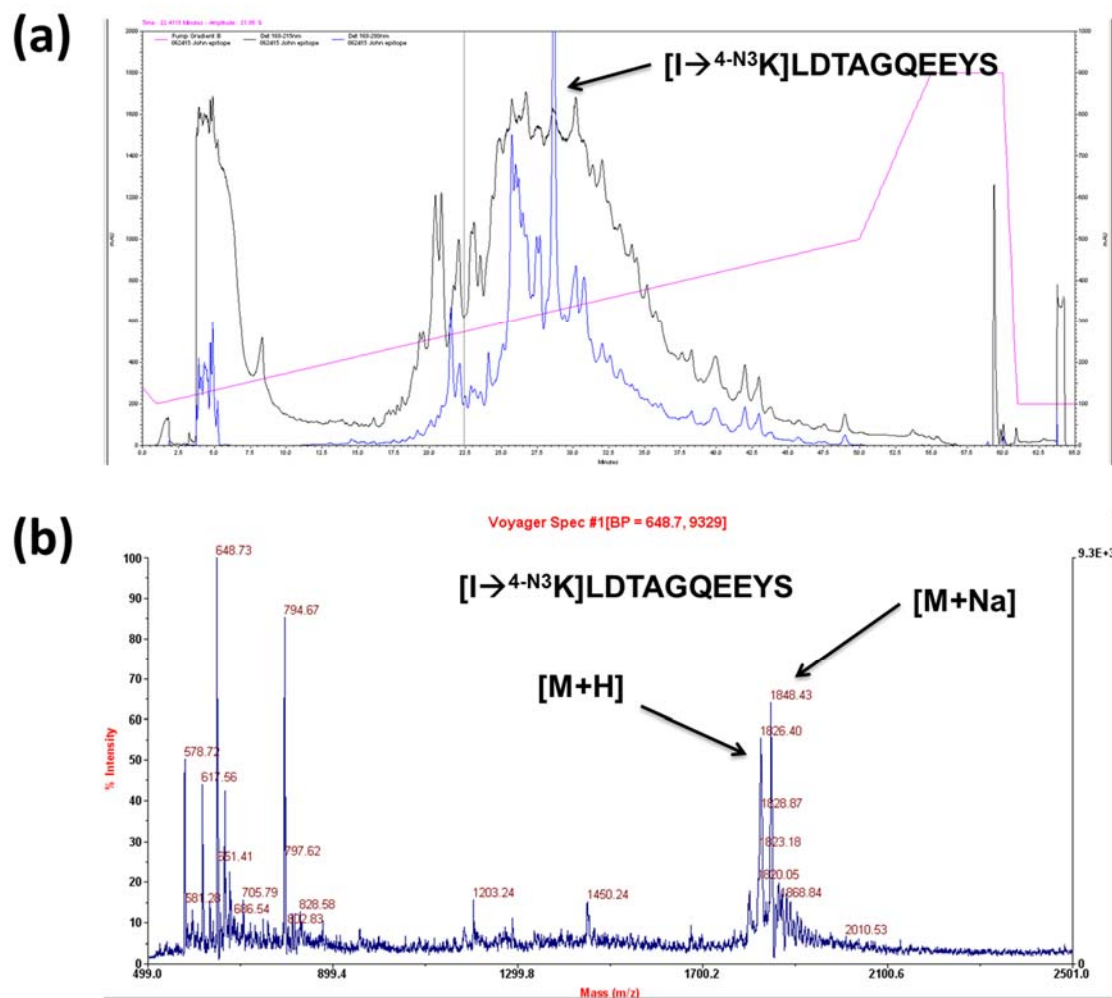**Figure 5.11** Scrambled SynEp1. (a) HPLC trace (b) MALDI trace.

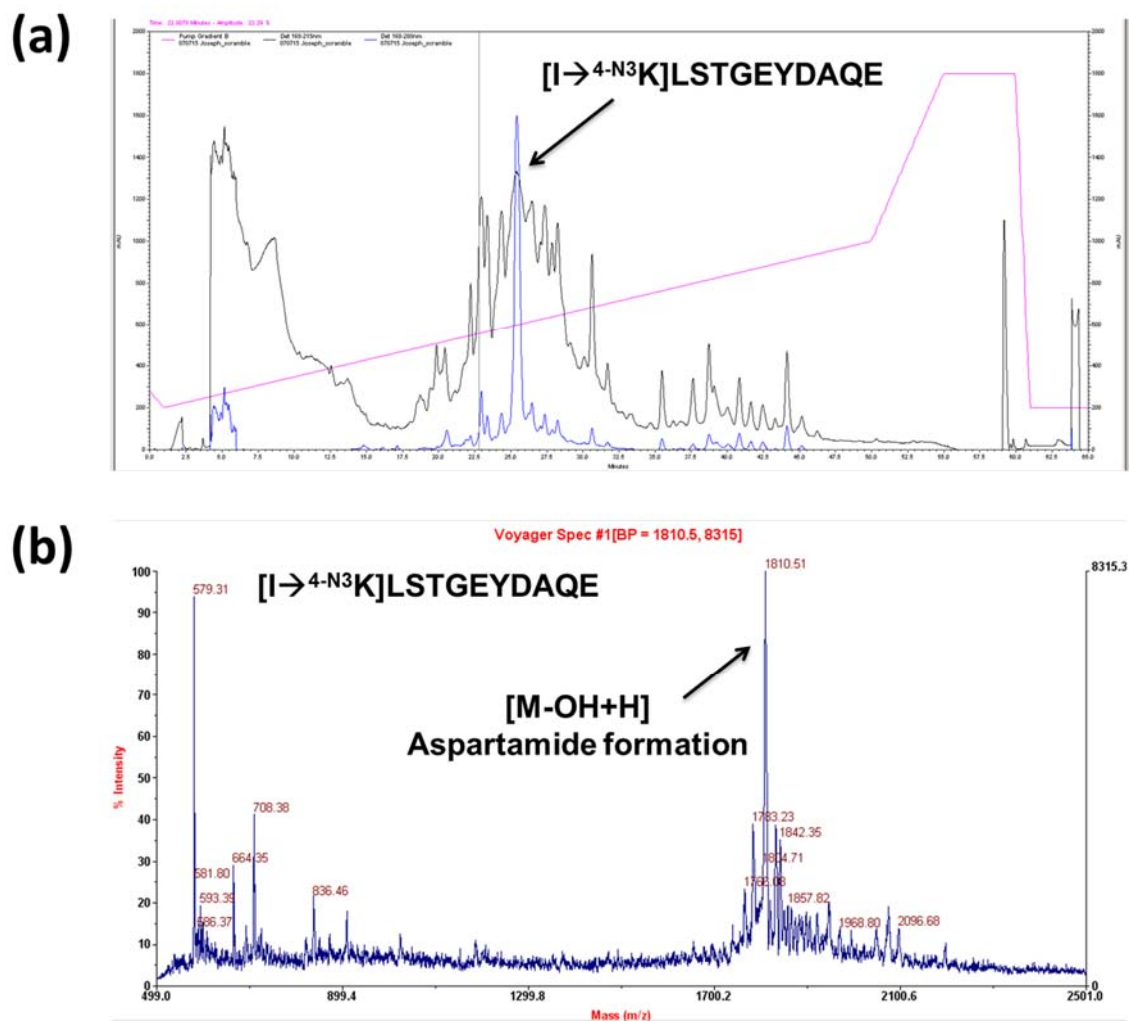**Figure 5.12** SynEp2. (a) HPLC trace (b) MALDI trace.

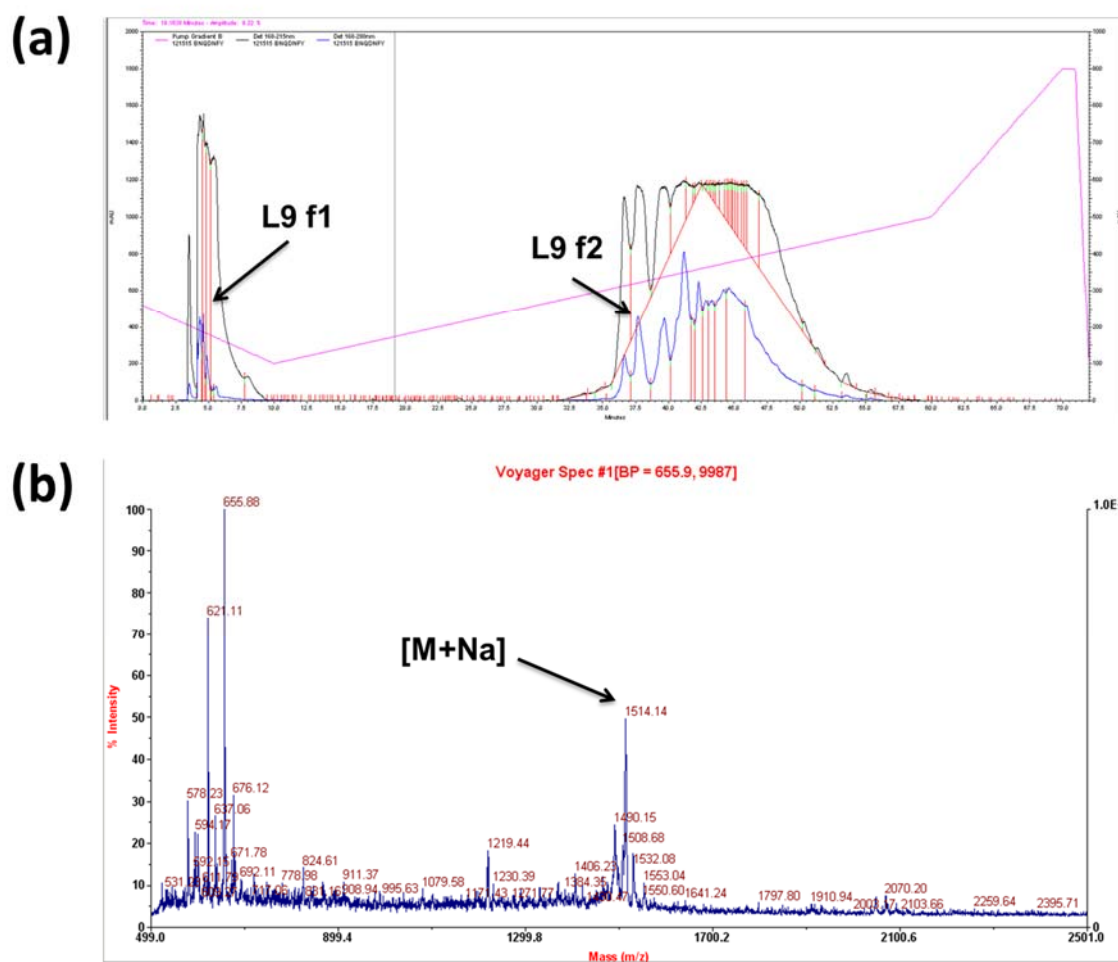**Figure 5.13** Scrambled SynEp2. (a) HPLC trace (b) MALDI trace.

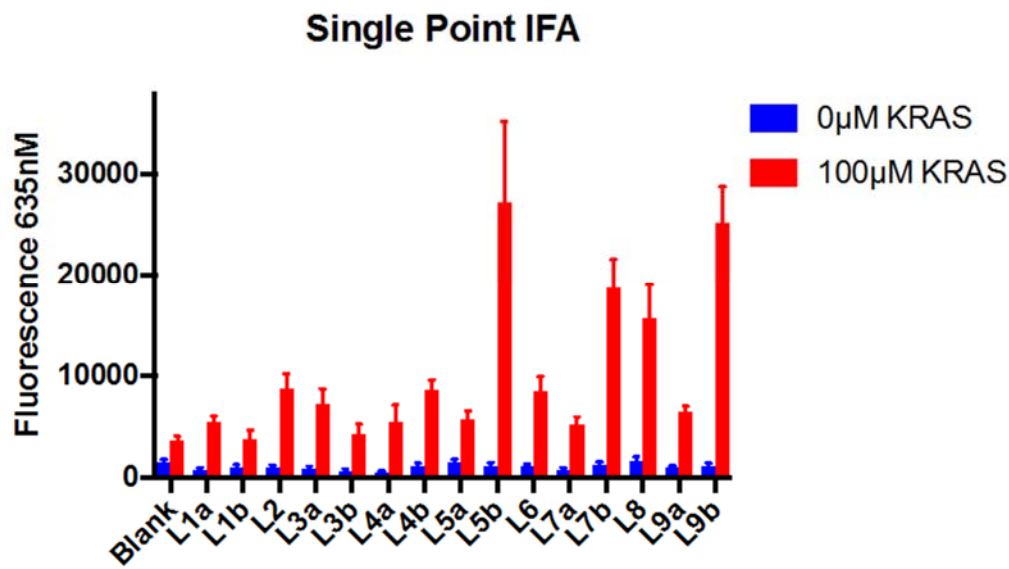**Figure 5.14** Ligand L9. (a) HPLC trace (b) MALDI trace.

Figure 5.15 Single point immunofluorescence Assay on B-RAP technology with KRas protein.
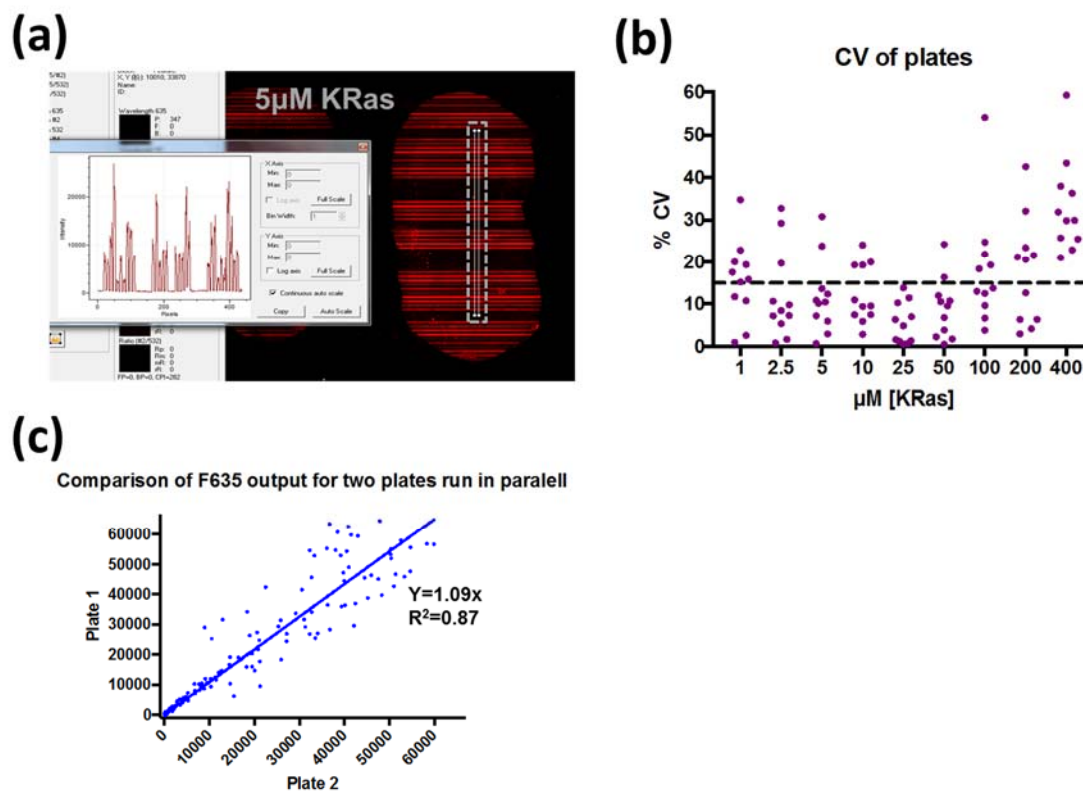

Figure 5.16 Statistical validation of the B-RAP technology. (a) Comparing the individual DNA barcode repeats in a given microwell at 5μM KRas reveals that extracting data from a single barcode repeat is sufficient. (b) The %CV for 1 μM to 400 μM KRas with the average %CV indicated by the black dashed line. c. A plot of the F635 values for both plates plotted against each other.
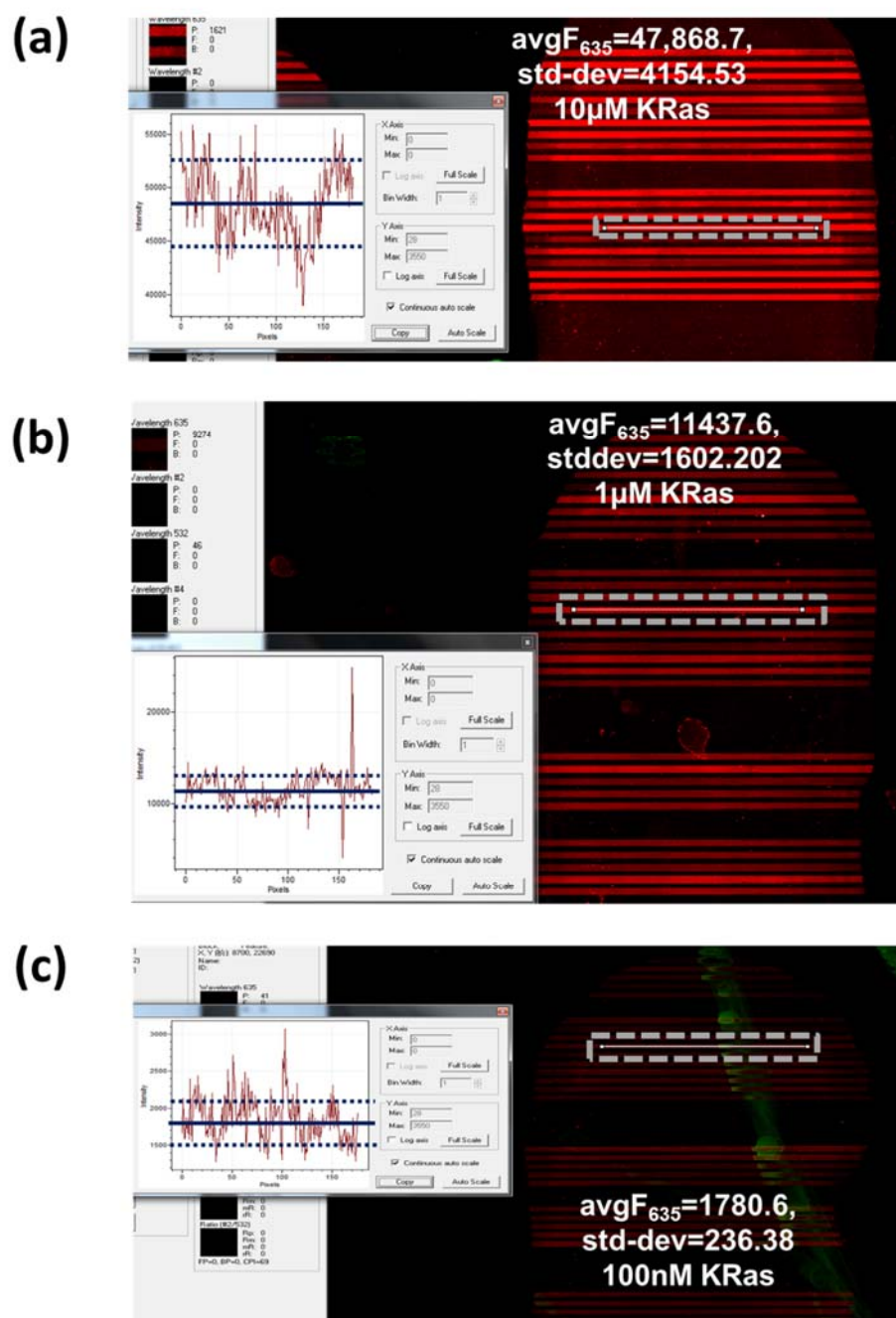
Figure 5.17 A comparison of the average line-scan with an averaged data block extraction. (a-c) A comparison of the full-line scan with the average F635 resulting from averaging ten discrete data block extractions and the corresponding standard deviations at three distinct concentrations of KRas.
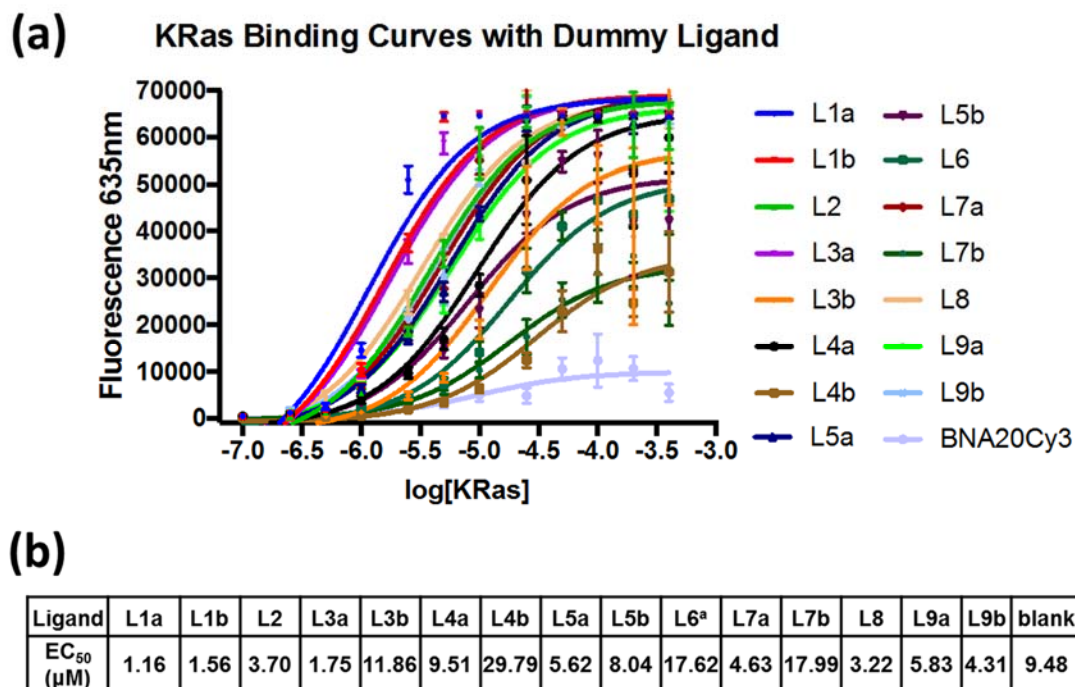
Figure 5.18 KRas binding curves without dummy ligand correction. (a) The KRas protein binding curves for the allosteric PCC ligands that were run on the B-RAP technology without dummy ligand correction. (b) The EC50 values for L1a to L9b. *[a]L6 was run separately.*

Figure 5.19 Representative binding curves using a 96-well plate ELISA. Representative binding curves of ligands run on a multi-well plate ELISA (a) A good binder on the multi-well ELISA platform and (b) A bad binder on the multi-well ELISA platform.

5.7 Appendix B: Supplementary tables

Table 5.1 A comparison of the multi-well ELISA platform and the rapid assay platform.
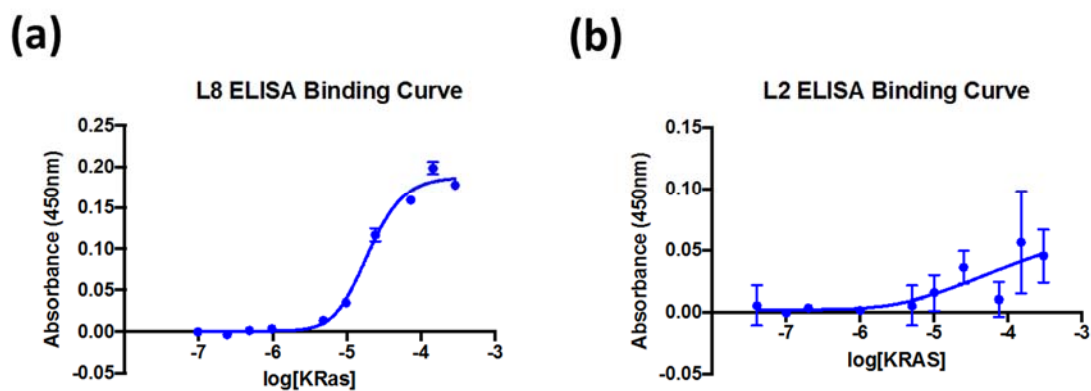
Criteria	ELISA Platform	B-RAP Platform
Curves per Assay	1	15
Relative amount PCC[a]	26.7	1
Relative amount Protein[b]	112.5	1
Unique [Protein]	12	16
Time to Run (h)	10-36	8-10
# Data Points[c]	96	2400

[a]*The relative amounts of PCC agent are the amounts required to run one binding curve on either platform.*

[b]*The relative protein amounts are the amounts needed to run one binding curve on either platform. If the total amounts required for running each platform were compared the ratio would be 7.5:1.*

[c]*The number of data points refers to the theoretical maximum of data points if the entire platform for both assay set-ups was utilized.*
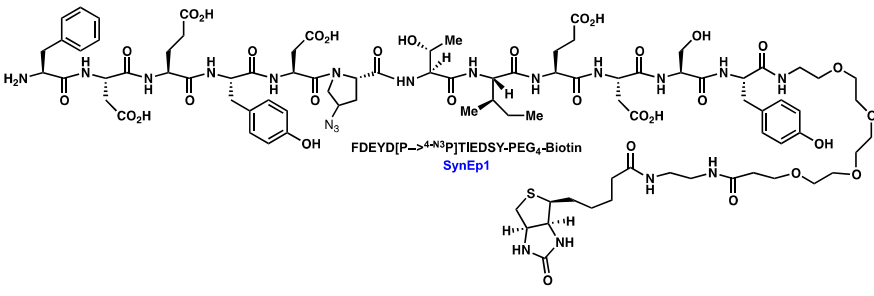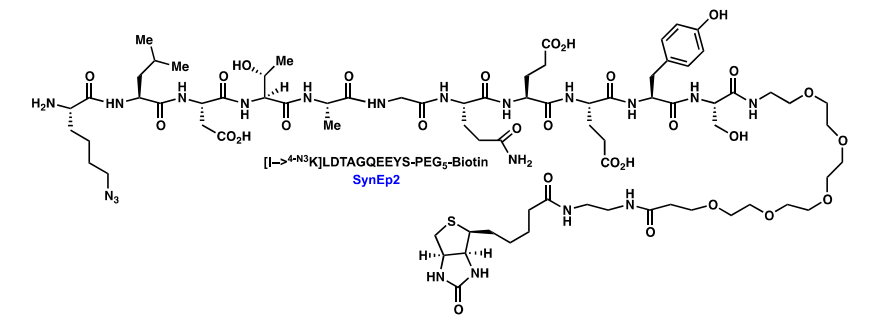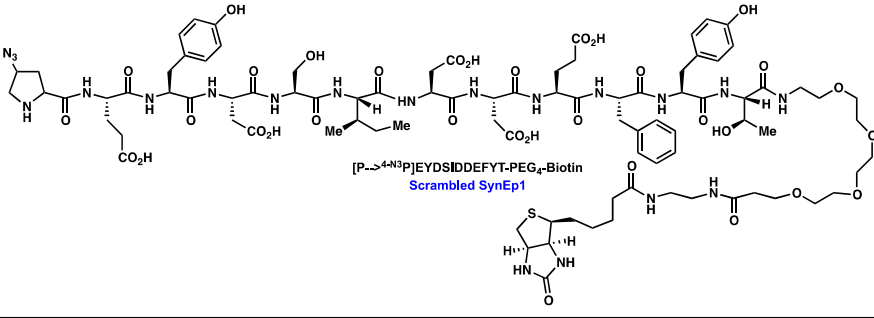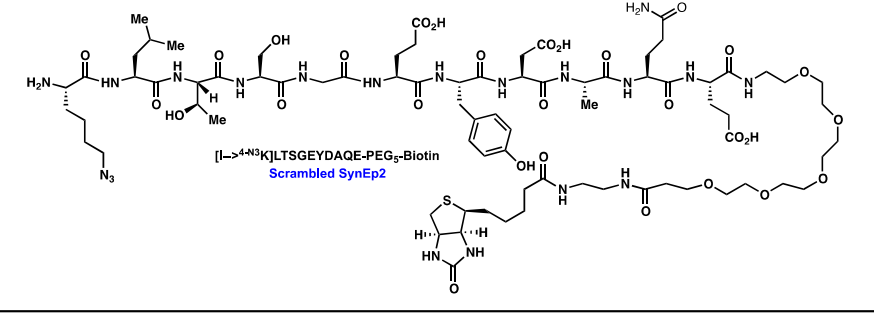
Table 5.2 Solution loading plates flow patterning versus tubing flow patterning for the fabrication of six devices.

Solution loading steps	Solution loading plates	Using tubings
Poly-L-lysine loading	12 min	> 24 min
Poly-L-lysine flow setting	10 min	20 min
DNA tubing prep	N.A.	30 min
DNA Loading	22 min	50 min

Table 5.3 ssDNA sequences for SAC-DNA conjugation and DNA barcode patterning.

Name	DNA Sequence
B	5'-NH$_2$-C6-AAA AAA AAA AAA AGC CTC ATT GAA TCA TGC CTA -3'
B'	5'-NH$_2$-C6-AAA AAA AAA ATA GGC ATG ATT CAA TGA GGC -3'
C	5'-NH$_2$-C6-AAA AAA AAA AAA AGC ACT CGT CTA CTA TCG CTA -3'
C'	5-NH$_2$-C6-AAA AAA AAA ATA GCG ATA GTA GAC GAG TGC -3'
D	5'-NH$_2$-C6-AAA AAA AAA AAA AAT GGT CGA GAT GTC AGA GTA-3'
D'	5'-NH$_2$-C6-AAA AAA AAA ATA CTC TGA CAT CTC GAC CAT-3'
E	5'-NH$_2$-C6-AAA AAA AAA AAA AAT GTG AAG TGG CAG TAT CTA -3'
E'	5'-NH$_2$-C6-AAA AAA AAA ATA GAT ACT GCC ACT TCA CAT-3'
F	5'-NH$_2$-C6-AAA AAA AAA AAA AAT CAG GTA AGG TTC ACG GTA-3'
F'	5'-NH$_2$-C6-AAA AAA AAA ATA CCG TGA ACC TTA CCT GAT-3'
G	5'-NH$_2$-C6-AAA AAA AAA AAA AGA GTA GCC TTC CCG AGC ATT-3'
G'	5'-NH$_2$-C6-AAA AAA AAA AAA TGC TCG GGA AGG CTA CTC-3'
H	5'-NH$_2$-C6-AAA AAA AAA AAA AAT TGA CCA AAC TGC GGT GCG-3'
H'	5'-NH$_2$-C6-AAA AAA AAA ACG CAC CGC AGT TTG GTC AAT-3'
K	5'-NH$_2$-C6-AAA AAA AAA AAA ATA ATC TAA TTC TGG TCG CGG-3'
K'	5'-NH$_2$-C6-AAA AAA AAA ACC GCG ACC AGA ATT AGA TTA-3'
L	5'-NH$_2$-C6-AAA AAA AAA AAA AGT GAT TAA GTC TGC TTC GGC-3'
L'	5'-NH$_2$-C6-AAA AAA AAA AGC CGA AGC AGA CTT AAT CAC-3'
M	5'-NH$_2$-C6-AAA AAA AAA AAA AGT CGA GGA TTC TGA ACC TGT-3'
M'	5'-NH$_2$-C6-AAA AAA AAA AAC AGG TTC AGA ATC CTC GAC-3'
N	5'-NH$_2$-C6-AAA AAA AAA AAA AGT CCT CGC TTC GTC TAT GAG-3'
N'	5'-NH$_2$-C6-AAA AAA AAA ACT CAT AGA CGA AGC GAG GAC-3'
O	5'-NH$_2$-C6-AAA AAA AAA AAA ACT TCG TGG CTA GTC TGT GAC-3'
O'	5'-NH$_2$-C6-AAA AAA AAA AGT CAC AGA CTA GCC ACG AAG-3'
P	5'-NH$_2$-C6-AAA AAA AAA AAA ATC GCC GTT GGT CTG TAT GCA-3'
P'	5'-NH$_2$-C6-AAA AAA AAA ATG CAT ACA GAC CAA CGG CGA-3'
Q	5'-NH$_2$-C6-AAA AAA AAA AAA ATA AGC CAG TGT GTC GTG TCT-3'
Q'	5'-NH$_2$-C6-AAA AAA AAA AGA CAC GAC ACA CTG GCT TAT-3'

Table 5.4 Synthetic epitopes and PCC ligands characterization table.

Structure	HPLC Retention Time (min)	Expected Mass (amu)	Observed Mass (amu)
FDEYD[P-->⁴⁻ᴺ³P]TIEDSY-PEG₄-Biotin **SynEp1**	32:30-33:30	[M+H]= 2049.88 [M+Na]= 2071.188	2074.32
[I-->⁴⁻ᴺ³K]LDTAGQEEYS-PEG₅-Biotin **SynEp2**	28:30-29:30	[M+H]= 1825.864	1826.22
[P-->⁴⁻ᴺ³P]EYDSIDDEFYT-PEG₄-Biotin **Scrambled SynEp1**	32:00-33:00	[M+H]= 2049.875	2166.39*
[I-->⁴⁻ᴺ³K]LTSGEYDAQE-PEG₅-Biotin **Scrambled SynEp2**	25:00-26:00	[M+H]= 1825.649, [M-OH+H] =1809.991	1810.51

*Multiple piperidine adducts and aspartamide formation observed.

Table 5.4 Synthetic epitopes and PCC ligands characterization table (continued).
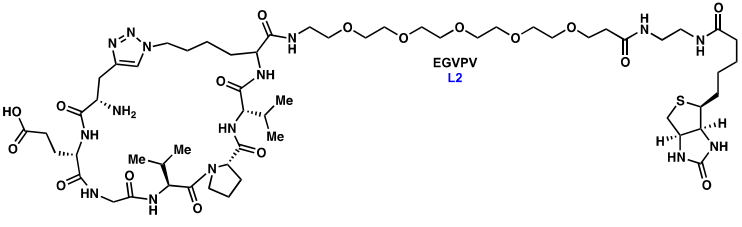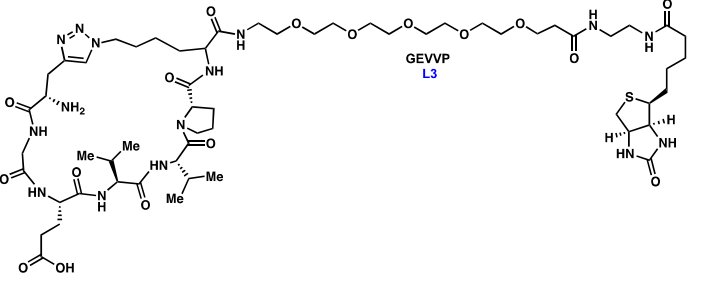
Structure	HPLC Retention Time (min)	Expected Mass (amu)	Observed Mass (amu)
HGIVG L1	3:30-4:30 (f1), 36:00-38:00 (f2)	[M+H]= 1290.699 [M+Na]= 1312.681	1310.81 (f1), 1289.31 (f2)
EGVPV L2	2:30-5:00	[M+H]= 1306.699 [M+Na]= 1330.682	1329.9
GEVVP L3	2:30-5:00 (f1), 41:30-43:00 (f2)	[M+H]= 1308.699 [M+Na]= 1330.681	1330.16 (f1), 1312.34 (f2)
VEVPY L4	36:30-39:30 (f1), 40:00-41:00 (f2)	[M+H]= 1414.740 [M+Na]= 1436.722	1414.38 (f1), 1435.89 (f2)

Table 5.4 Synthetic epitopes and PCC ligands characterization table (continued).
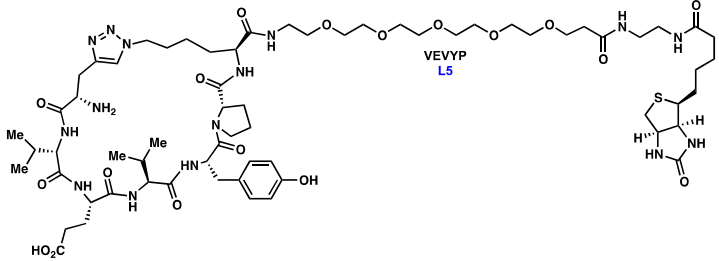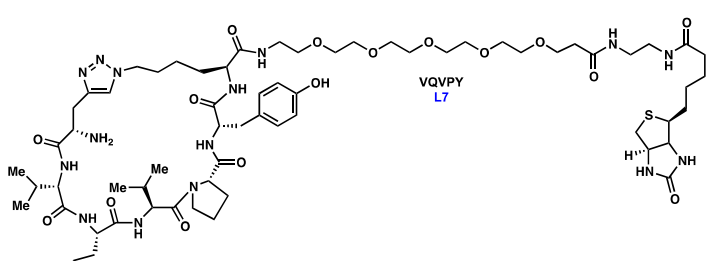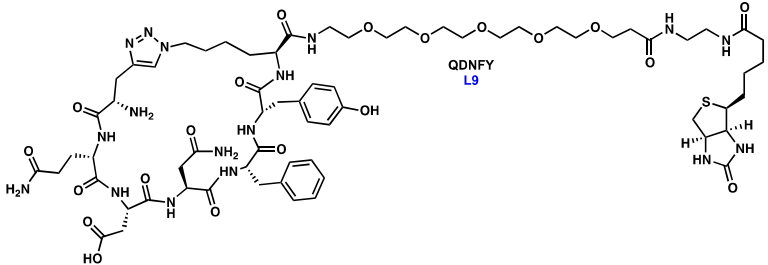
Structure	HPLC Retention Time (min)	Expected Mass (amu)	Observed Mass (amu)
VEVYP L5	37:00-39:00 (f1), 39:00-40:00 (f2)	[M+H]= 1414.740 [M+Na]= 1436.721	1413.47 (f1), 1435.88 (f2)
VTVPY L6	37:30-39:00	[M+H]= 1386.746 [M+Na]= 1408.727	1387.36
VQVPY L7	36:00-38:30 (f1), 39:00-41:30 (f2)	[M+H]= 1413.722 [M+Na]= 1435.738	1412.29 (f1), 1434.80 (f2)
TDNFY L8	36:30-38:00	[M+H]= 1467.694 [M+Na]= 1489.676	1488.37

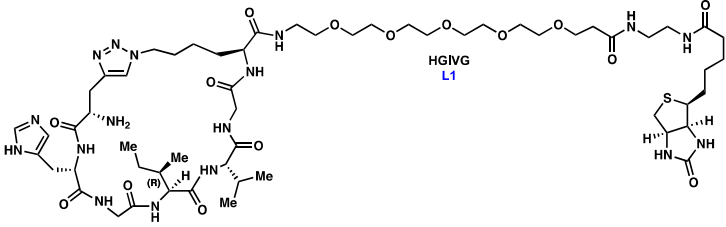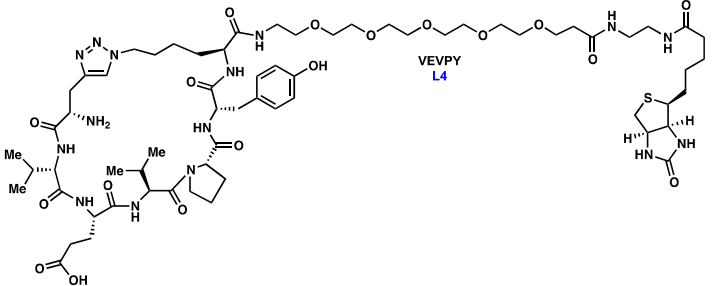**Table 5.4** Synthetic epitopes and PCC ligands characterization table (continued).

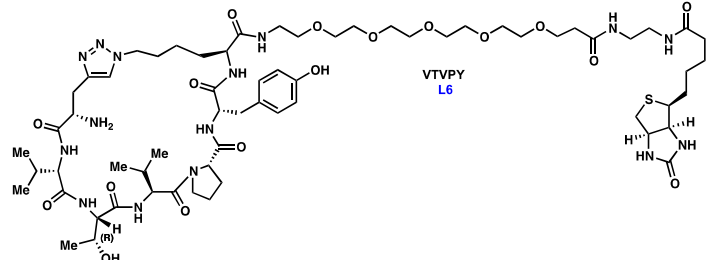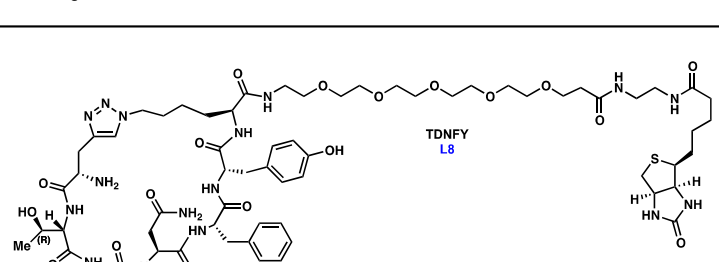| Structure	HPLC Retention Time (min)	Expected Mass (amu)	Observed Mass (amu)
	4:30-5:30 (f1), 37:00-38:30 (f2)	[M+H]= 1494.705 [M+Na]= 1516.687	1514.14 (f1), 1494.04 (f2)

5.8 Appendix C: Supplementary materials

5.8.1 Barcode microfabrication and validation

Chrome masks of the custom barcode design were purchased from University of California, Los Angeles, Nanoelectronics Research Facility, and Karl Süss MA/BA6 mask aligner (SÜSS MicroTec AG) was used for UV exposure. Silicon wafers (Wafernet Inc.), SU8-2025, and SU8 developer (Microchem Corp) were used for the barcode mold fabrication. Anhydrous dimethylsulfoxide (DMSO), sodium dodecyl sulfate (SDS), and bis(sulfosuccinimidyl)suberate) (BS3) used in barcode fabrication were purchased from American Type Culture Collection (ATCC), Sigma Aldrich, and ThermoFischer Scientific respectively. The Sylgard 184 elastomer, and poly-L-lysine coated glass slides used in DNA barcode microfabrication were purchased from Dow Corning and ThermoFischer Scientific respectively. The poly-L-lysine (PLL) solution (0.1% ($^w/_w$) used for barcode fabrication and secondary blocking in the IL-17F protein assay was purchased from Sigma Aldrich. All ssDNA used for barcode fabrication and barcode validations were purchased from either Bioneer Inc. or IDT Inc.

5.8.2 Protein expression, purification, and refolding

The Bacto Tryptone (Tryptone) and Bacto yeast (yeast) for the preparation of LB broth media were purchased from Becton, Dickinson, and Company. The ampicillin sodium salt, chloramphenicol, and isopropyl β-D-1-thiogalactopyranoside (1,6-IPTG, dioxane free) used for protein expression from *E. coli* were purchased from Sigma Aldrich. The one-shot B21(D3) *E. coli* cells and PQE80 vector (His$_6$-tagged human KRas Isoform 4B (residues 1-169)) used for expression of KRas protein were purchased from Life

Technologies and Qiagen respectively. Lysozyme (L6876), DNAse I (10104159001), and RNAse A (R6513-10MG) used for lysing cells containing cysteine-modified streptavidin (SAC) were purchased from Sigma-Aldrich. Cells containing KRas protein were lysed using a constant pressure cell disruptor (Constant Systems Ltd., Scotland, UK). Surfactants Triton X-100 and polysorbate 20 (Tween20) were purchased from Sigma Aldrich. The 20x phosphate buffered saline with 0.05% Tween 20 (PBST) and phosphate buffered saline (PBS) used for protein purification and immunofluorescent assays (IFAs) were purchased from Cell Signaling Technology and Corning respectively. The sodium bicarbonate ($NaHCO_3$), ammonium acetate (NH_4OAc), sodium acetate (NaOAc), sodium chloride (NaCl), Imidazole, tris(hydroxymethyl)aminomethane (Tris), tris(hydroxymethyl)aminomethane hydrochloride salt (Tris•HCl), Guanidinium chloride (Guan•HCl), magnesium chloride pentahydrate ($MgCl_2•5H_2O$), and beta-mercaptoethanol (βME) used in protein purification and IFA assays were purchased from Sigma Aldrich. The 2-imminobiotin agarose resin, Superdex 75 (10/300) increase column, and Ni-NTA superflow cartridge used for fast protein liquid chromatography (FPLC) purification were purchased from Sigma Aldrich, GE Healthcare Life Sciences, and Qiagen respectively. The Amicon Ultra-15 and Ultra-4 centrifugal filters used to concentrate protein samples were purchased from EMD Millipore.

5.8.3 SAC-DNA conjugation and DESL set validation

The tris-(2-carboxyethyl)phosphine hydrochloride (TCEP), anhydrous N,N-dimethylformamide (DMF), N-succimidly-4-formyl benzaldehyde (S-4FB) and maleimide 6-hydrazino-nicotinamide (MHPH) used for the conjugation of ssDNA to Cysteine-

modified Streptavidin (SAC) were purchased from Sigma Aldrich and Solulink. The biotin-A$_{20}$-Cy3 (Biotin*) probe used to test the biotin binding ability of the DESL set and used as a biotinylated blank for IFA assays was purchased from IDT Inc. The complementary ssDNA used for conjugation to SAC were purchased from Bioneer Inc.

5.8.4 In situ library screen and hit bead sequencing

The mouse anti-biotin-alkaline phosphatase conjugated antibody (ab) (#A6561), goat anti-rabbit-alkaline phosphatase conjugated ab (#A8025), rabbit anti-Ras ab (CST #3965), used for the combined anti screen/pre-clear and the subsequent product/target screens were purchased from Sigma Aldrich and Cell Signaling Technology respectively. The combined 5-bromo-4-chloro-3-indoyl phosphate (BCIP)/ nitro blue tetrazolium (NBT) (#S3771) used to develop hits during the library screens was purchased from Promega. The concentrated hydrochloric acid used to quench the BCIP/NBT development was purchased from Sigma Aldrich. Sequencing of bead hits occurred via Edman degradation sequencing on a Procise Protein Sequencer (Applied Biosystems, California).

5.8.5 Peptide synthesis and purification

Fmoc-protected amino acids were purchased from Anaspec, AAPTec, Bachem, ChemPep, and Sigma-Aldrich. Biotin NovaTag™ resin was obtained from EMD Chemicals, Inc. and used for the synthesis of biotinylated peptides and epitopes used for the screens using standard Fmoc/^{t}Bu coupling and cleavage protocols. The peptide one-bead-one compound (OBOC) library was prepared on Tentagel Resin purchased from RAPP Polymere. The Fmoc-protected propionic acid polyethylene glycol (PEG$_n$) linkers were purchased from ChemPep Inc. The L-Ascorbic Acid and copper (I) iodide (CuI) used

for click reactions were purchased from Sigma Aldrich. The N-methyl pyrrolidine (NMP), 1-[Bis(dimethylamino)methylene]-1H-1,2,3-triazolo[4,5-b]pyridinium 3-oxid hexafluorophosphate (HATU), and *N,N'*-diisopropylethylamine (DIPEA) used in peptide synthesis were bought from EMD Chemicals, Inc., ChemPep, and Sigma-Aldrich respectively. Piperidine, trifluoroacetic acid (TFA), and triethylsilane (TESH) were purchased from Sigma-Aldrich. The diethyl ether used to precipitate crude peptide was purchased from JT Baker. The Omnisolv grade acetonitrile (MeCN) used for peptide purification was purchased from EMD Millipore. Unless otherwise stated, peptide preparation was performed using a Titan 357 Automatic Peptide Synthesizer (AAPPTec, Louisville, KY) or a Liberty 1 Automated Peptide Synthesizer (CEM, North Carolina). Mass analysis was performed using a Voyager De-Pro matrix assisted laser desorption ionization time-of-flight mass spectrometer (MALDI-TOF MS) (Applied Biosystems, California). The crude peptides were dissolved in either DMSO (Sigma Aldrich) or (1:1) MeCN/doubly distilled water (MQ H_2O) w/ 0.1% TFA before purification by a gradient of 0% to 50% acetonitrile in MQ H_2O with 0.01% ($^v/_v$) TFA using a RP-HPLC (Beckman Coulter System Gold 126 Solvent Module and 168 Detector) using a C18 reversed phase semi-preparative column (Phenomenex Luna 10 µm, 250 × 10 mm). The concentration of peptides and epitopes was determined using a Nanodrop 2000 Spectrophotomer (ThermoFischer Scientific Inc., Massachusetts).

5.8.6 B-RAP immunofluorescence assays and multi-well enzyme-linked immunosorbent assays

The Bovine Serum Albumin (BSA, Biotin free A1933-25G) used in the IFAs and multi-well enzyme-linked Immunosorbent assays (ELISAs) was purchased from Sigma-Aldrich. The non-fat dry milk powder used in the enzyme-linked Immunosorbent assays (ELISAs) was purchased from Best Value. The rabbit anti-Ras (CST #3965), Goat anti-rabbit IgG HRP-linked (CST #7074), goat anti-rabbit HRP-linked (CST #7074), goat anti-mouse-Alexafluor 647 conjugated (ab150115), goat anti-mouse-Alexafluor 647 conjugated (ab150115), goat anti-rabbit-Alexafluor 647 conjugated (ab150079), and mouse monoclonal IL-17F (#TA319596) antibodies were purchased from Cell Signaling Technologies, Abcam, and Origene respectively. Recombinant human His-tagged IL-17F (ab167911) was purchased from Abcam. The ELISAs were run on either 96-well clear Pierce Neutravidin Plates (#15129) or Pierce Neutravidin Coated Plates (#15127) purchased from ThermoFischer Scientific. The TMB Microwell Peroxidase Substrate System (#50-76-00) that was used to develop ELISAs was purchased from KPL. The sulfuric acid ($H_2SO_{4(aq)}$) used to quench the enzymatic amplification reaction in the ELISAs was purchased from JT Baker. The 96-well ELISA plates were read using a Flexstation 3 plate reader (Molecular Devices LLC, Sunnyvale, CA). All barcode slides were scanned using an Axon GenePix 4400A (Molecular Devices LLC, Sunnyvale, CA).

5.9 Appendix D: Supplementary methods

5.9.1 DNA barcode chip patterning and validation

The DNA barcode chips were prepared by micro channel-guided flow patterning as described in References 24 and 25 of the main text. A PDMS slab having the micro-channels was made by soft lithography on a silicon wafer. Its mold was designed as Figure 5.5a and prepared with SU8 2025 negative photoresist. The fabricated mold contained microfluidic circuits of 20 parallel channels with 50 μm width and ~40 μm height. Sylgard® 184 PDMS pre-polymer and curing agents were mixed in a 10:1 ratio, degassed, poured ~60g of the mixture on the mold, and baked for two hours at 80 °C for curation. The cured PDMS slab peeled off from the mold, cut into individual microfluidic molds, and the inlet and outlet holes of the microfluidic circuits were punched with the sizes of two mm and 0.5 mm respectively. The number of the inlets and outlets punched out were determined by the number of single stranded DNAs (ssDNAs) used in the assay, and fifteen orthogonal ssDNAs (B-Q, Table S2) were used in this study. The slab was then aligned with a PLL glass slide, and bonding occurred with baking at 80 °C for two hours. After cooling briefly, the inlet wells were loaded with 3 μL of a 0.1% PLL solution, and the PLL solution was flowed and dried by 13.8 kPa nitrogen gas blowing through the solution-loading device overnight. The next day, C6 amine-modified DNA solutions (300 μM in (3:2 (v/v)) PBS/DMSO) were individually mixed (1:1) with a 2 mM BS3 cross-linker solution in PBS. Each freshly prepared mixture was flown through a channel under 13.8-20.6 kPa nitrogen gas using the solution-loading device for 1 hour, and then only the assembled PDMS slab and bonded PLL slide was incubated at room temperature for 2

hours in a humidified chamber. After incubation, the PDMS slab was removed, and the DNA patterned PLL slides were washed with a 0.02% aqueous SDS solution, doubly distilled water (MQ H2O) (3x), and spun dry.

To validate the DNA barcode chips, a 5'-modified Cy3-labeled complementary ssDNA cocktail was prepared in 1% BSA in PBS (50nM each ssDNA). The validation occurred over two rounds (B, D, F, H, K, N, P, M then C, E, G, I, L, O, Q) in order to check for channel leaks and crossover. A 120 μL aliquot of the validation solution was applied to a small region at the bottom edge of the DNA barcode before incubating at 37 °C for one hour. After incubation, this region was washed with 1% BSA in PBS, PBS (2x), and the slide was spun dry before being scanned by Axon GenePix 4400A (532nM, PMT 450, Power 15%) (Figure 5.5b).

5.9.2 Expression of cysteine-modified streptavidin (SAC) protein

The SAC protein was expressed using a modification of the procedures reported by Sano and Cantor.[12] A 100 mL starter culture of autoclaved LB media (10.0 g Tryptone, 5.00 g yeast, 10.0 g NaCl per L H2O) was prepared by inoculating with 50 μL of 100 $^{mg}/_{mL}$ of ampicillin (final concentration 50 $^{μg}/_{mL}$) and 100μL of 34 $^{mg}/_{mL}$ chloramphenicol (final concentration 34 $^{ug}/_{mL}$) followed by a sterile pipet scraping of a 50% ($^{v}/_{v}$) glycerol stock containing transformed *E. coli* BL21(D3) cells. The starter culture incubated overnight at 37 °C and 250 RPM before adding 10.0 mL of starter culture aliquots to six 2800mL Fernbach-Style Culture Flasks containing 1.00 L autoclaved LB media with 500 μL of 100 $^{mg}/_{mL}$ of ampicillin (final concentration 50 $^{μg}/_{mL}$), 1000 μL of 34 $^{mg}/_{mL}$ chloramphenicol (final concentration 34 $^{ug}/_{mL}$), and 1000μL of 40% ($^{w}/_{w}$) autoclaved glucose (final

concentration 0.4% (^{w}/$_w$). The flasks were left to culture at 37.0 °C, 250 RPM until A$_{680}$ = 0.500 and induction was triggered with 1000 µL of a 400 mM 1,6-IPTG solution (final concentration 400 µM). Expression continued at 37.0 °C, 250 RPM for four hours before spinning down the cells at 6000 RPM, 5 minutes @ 4 °C. Cells were resuspended in 50 mL of a 10 mM Tris, 1 mM EDTA, 130 mM NaCl buffer @ pH=8.0 and spun down (2x). The cells were flash frozen in N$_{2(l)}$ and stored at -80.0 °C until needed.

5.9.3 Isolation of SAC IB from E. coli cells

The cell pellet was thawed in ice before resuspending in two 50-mL falcon tubes with 40 mL of TEX buffer (30mM Tris, 2mM EDTA, 0.1% TritonX). Each tube was charged with 40 mg fresh lysozyme powder (Final concentration 1.0 ^{mg}/$_{mL}$), vortexed until mixed, and allowed to lyse for 30min while tumbling @ RT. The solution was very viscous after lysis. The DNA and RNA were degraded by adding 400 µL of 10 ^{mg}/$_{mL}$ DNAse and RNAse in TE Buffer (10 mM Tris, 130 mM NaCl, 1 mM EDTA) (final concentration 10 ^{µg}/$_{mL}$), 960 µL of 500 mM MgCl$_2$ (Final concentration 12 mM), and 40 µL of 1 M MnCl$_2$ (Final concentration 1 mM) to each tube of cell lysate and the solution was allowed to digest for 30 minutes while tumbling @ RT. After digestion, the solution was spun down @ 7800 RPM, RT for 10 minutes. The resulting pellets were both washed in 40 mL TEX buffer and spun down @ 7800 RPM, 5 minutes at RT. Pellets were washed with 40 mL buffer minus Triton X again before spinning down @ 7800 RPM, 5 minutes at RT once more. Each pellet was taken up in 10 mM Tris and spun down @ 7800RPM, 10 minutes @ RT, aliquotted, and stored at -80.0 °C until needed. If the final pellet is light brown, then some DNA is still present. This will be removed at the beginning of the refolding procedure.

5.9.4 Refolding and purification of SAC protein

The procedure described here is a modification of the procedure developed by Sano and Cantor.[12]

After the initial denaturing keep all solutions at 4 °C

An IB aliquot was dissolved in 1000 μL denaturing buffer (6 M Guanidine • HCl @ pH=1.5 with 10 mM βME), vortexed, spun down at 13,000 RPM, 2min @ RT, and filtered using a 0.45 μM filter. The resulting solution should be clear and nearly colorless. The A_{280} was measured on a Nanodrop2000 spectrophotometer, and the concentration of denatured SAC monomer was calculated. The extinction coefficients for the proteins, peptides, and epitopes were calculated using the peptide properties calculator (http://biotools.nubic.northwestern.edu/proteincalc.html). The denatured SAC solution was diluted to 1000 μL in denaturing buffer and added dropwise to a rapidly stirring solution of refolding buffer (50 mM NH$_4$OAc, 150 mM NaCl, 10 mM βME @pH=6.0) (Final [SAC] ~4 μM). The stir rate was then decreased, and the solution was covered in aluminum foil and allowed to refold overnight. After sterile filtration the resulting solution was concentrated to 10-15 mL using Amicon Millipore filters (10,000-30,000 MWCO) before dialyzing the refolded SAC protein in Buffer A (50 mM NaHCO$_3$, 500 mM NaCl, 10 mM βME @ pH=11.0) until the solution had a pH of ~11 (about 2 hours). The crude protein was then diluted (1:1) with buffer A, mixed with 2 mL of 2-iminobiotin agarose resin, and allowed to incubate with tumbling in the cold room for one hour. After incubation the supernatant was eluted (3x) before eluting with buffer A until A_{280} went to baseline. Pure SAC was eluted with buffer B (50 mM NaOAc, 50 mM NaCl @ pH=4.0)

until A_{280} went to baseline again. Fractions with pure SAC were pooled and dialyzed against a PBS solution (PBS, 10 mM βME, pH=7.5) overnight. The SAC was concentrated to ~1 $^{mg}/_{mL}$ final concentration, divided into 100 μL aliquots, and stored at -80 °C.

5.9.5 Preparation of the DESL SAC-DNA conjugates

For each planned SAC-DNA conjugation, two Zeba columns were prepared (3x 300 μL 5 mM TCEP in PBS, 3.9k RPM, 1 min @RT). Each 100 μL aliquot of SAC was desalted in two separate Zeba columns to remove the βME (3.9k RPM, 2 min @RT). After transferring to eppendorf tubes, 6 μL anhydrous DMF was added followed by 6 μL MHPH (100 mM in anhydrous DMF). Separate eppendorf tubes were charged with 80 μL of 500 mM DNA in PBS followed by 10 μL anhydrous DMF and 10 μL S-4FB (100 mM in anhydrous DMF). The SAC and DNA solutions were vortexed gently, briefly spun down, and left to react at RT in the dark for four hours. For each conjugation in progress, four Zeba columns were buffered exchanged with citrate buffer (150 mM NaCl, 50 mM sodium citrate, pH=6.0) (3 x citrate buffer, 3.9k RPM, 1 min @ RT). The SAC and DNA solutions were desalted separately (2 x 3.9k RPM, 2 min, @ RT) before combining each SAC aliquot with a unique ssDNA solution. The solutions were vortexed gently, briefly spun down, and left to react in the dark @ RT overnight. The reactions were quenched by placing @ 4°C. Each SAC-DNA conjugate was purified by FPLC using a Superdex75 Increase column (isocratic in PBS, 0.5 $^{mL}/_{min}$, 0.5 mL fractions, 75 minutes). Fractions containing pure SAC-DNA were pooled and concentrated using Amicon Ultra-4 Centrifugal filters (30k MWCO): 3900 RPM, 30 minutes @ 4°C. The concentrated SAC-DNA proteins were quantified using a Nanodrop2000 spectrophotometer in the ssDNA nucleic acid mode and stored at

4 °C until needed. The exctinction coefficients for the ssDNA strands were calulated using the IDT oligo analyzer (https://www.idtdna.com/calc/analyzer).

5.9.6 DESL set biotin binding capacity validation protocol

Buffers used:

Wash buffer: PBS + 0.05% Tween20 (PBST)

Blocking Buffer: PBS + 1% BSA

*Wash steps used 50 $^{\mu L}/_{well}$

*Incubation steps used 30 $^{\mu L}/_{well}$

After loading the Biotin* probe change pipette tips every time that you aspirate or add solution to a well to prevent cross contamination

A prefabricated PDMS template was aligned onto the DNA barcode and the microchip slide was taped into a 10 cm petri dish. The wells were washed with PBST before loading blocking buffer and placing the platform into a 37 °C incubator for one hour. A cocktail containing 50 nM of each SAC-DNA in PBS was prepared and added to the pre-blocked wells. The SAC-DNA conjugates were allowed to hybridize to the DNA barcode at 37 °C for one hour before washing the wells with PBST (3x). Each well was loaded with 50 nM, 100 nM, 150 nM, 200 nM, 300 nM, or 400 nM Biotin* in PBS (Figure 5.8), and the platform was left to shake covered at RT for one hour. The wells were washed with PBST (3x) before peeling off the PDMS slab and dipping the barcode into PBS, (1:1)

PBS/MQ H₂O, MQ H₂O (2x). The barcode was then spun dry and read on the Genepix (532 nM, PMT 450, Power 15%).

5.9.7 Expressing and purifying WT KRas protein

The KRas protein was expressed and purified using a modification of the procedure reported by Kuriyan.[28] A starter culture of 100 mL of autoclaved LB media was inoculated with 100 µL of 100 $^{mg}/_{mL}$ of ampicillin (final concentration 100 $^{µg}/_{mL}$) followed by a scraping of a 25% ($^v/_v$) glycerol stock containing transformed *E. coli* cells. The starter culture was left in an incubator at 37.0 °C, 250 RPM overnight before adding 10.0 mL starter culture aliquots to six 2800 mL Fernbach-Style Culture Flasks containing 1.00 L autoclaved LB media with 1000 µL of 100 $^{mg}/_{mL}$ of ampicillin (final concentration 100 $^{µg}/_{mL}$). The flasks were left to culture at 37.0 °C, 250 RPM until A_{680} = 0.500-0.600 and induction was triggered with 1000 µL of a 250 mM 1,6-IPTG solution (final concentration 250 µM). The cells were then left to express overnight at 18.0 °C, 250 RPM before being spun down, resuspended in Buffer A (20 mM Tris, 500 mM NaCl, 20 mM imidazole, 5 mM MgCl₂, pH=8.0), flash frozen in N₂₍ₗ₎, and stored at -80.0 °C until needed. After thawing and douncing, the cells were lysed using a cell disruptor, the cell wall lysate spun down at 8000 RPM, 4 °C for 20 minutes, sterile filtered, and purified using FPLC with a Ni-NTA superflow cartridge and a gradient of Buffer A to Buffer B (20 mM Tris, 300 mM NaCl, 250 mM imidazole, 5 mM MgCl₂, pH=8.0). Fractions containing pure KRas were pooled and dialyzed against Tris buffered saline (TBS) (25 mM Tris, 150 mM NaCl, 10 mM MgCl₂, pH=7.5) overnight. The resulting solution was concentrated using Amicon

Ultra-15 centrifugal filters (10k MWCO), quantified,[2] separated into aliquots, flash frozen in $N_{2(l)}$, and stored at -80.0 °C until needed.

5.9.8 In situ library click screen combined preclear/anti-screen

The *in-situ* click dual SynEp library screen followed a procedure similar to the one outlined in Reference 1 from the main text using 450 mg of Pra-capped one-bead-one-compound (OBOC) library. Blocking was performed overnight at 4 °C with blocking buffer (1% BSA and 0.1% Tween20 in TBS). After washing with blocking buffer (3 x 3 minutes) incubation with 25 μM of each scrambled SynEp in binding buffer (0.1% BSA and 0.1% Tween20 in TBS) occurred overnight at 4 °C. The library was washed with TBS (3 x 1 minute) then stripped with 7.5 M Gua•HCl (pH=2.0) at RT for one hour to remove any non-covalently bound scrambled SynEps. Ten rinses with TBS preceded another incubation with blocking buffer at RT for one hour. After five quick rinses of the library with blocking buffer the library was incubated with a cocktail of a (10,000:1) dilution of the mouse anti-biotin-alkaline phosphatase conjugated ab, (1,000:1) dilution of the rabbit anti-Ras ab, and a (10,000:1) dilution of the goat anti-rabbit-alkaline phosphatase ab in binding buffer to perform the preclear and anti-screen in one assay. Washes (5 x 3 minutes) with a high salt buffer (25 mM Tris•HCl, 10 mM $MgCl_2$, 700 mM NaCl, pH=7.4), and a low salt buffer (5 x 3 minutes) (25 mM Tris•HCl, pH=7.4). The developing buffer was prepared with 66 μL of BCIP (50 $^{mg}/_{mL}$ in 70% DMF) in 10mL of developing buffer (100 mM Tris•HCl, 150 mM NaCl, 1 mM $MgCl_2$) and incubated with the library beads in a 20cm petri dish for ten minutes before adding 66 μL of NBT (50 $^{mg}/_{mL}$ in 70% DMF) and incubating for an additional fourteen minutes. The beads were then washed 5x with TBS,

and stored in 0.1 M HCl$_{(aq)}$ in a 20 cm petri dish. Any beads that turned purple during the combined preclear/anti-clear were promiscuous binders and consequently were picked out using a 10-μL micropipette and discarded. After removing all of the sticky beads the remaining beads were washed with 7.5 M Guan•HCl (pH=2.0) for 30 minutes, rinsed with MQ H$_2$O (10x), and incubated in NMP overnight to remove any trace purple coloring. Final rinses with MQ H$_2$O (3x), TBS (7x) preceded an overnight incubation at 4 °C with blocking buffer.

5.9.9 Library click-screen product screen

The pre-blocked library was washed with blocking buffer (3 x 5 minutes) before loading 25 μM of each SynEp in binding buffer and incubating at RT overnight. After rinsing with TBS (3x) the library was incubated with 7.5 M Guan•HCl (pH=2.0) for one hour at RT before rinsing with TBS (10x). The library underwent an additional 1 hour incubation with blocking buffer at RT before rinsing with blocking buffer (5x), and incubating with a (10,000:1) dilution of the mouse anti-biotin-alkaline phosphatase conjugated ab in binding buffer for one hour at RT. Development of the library followed the same procedure as the preclear/anti-screen, and the darkest beads were set aside for Edman degradation sequencing. The remaining ~50 light purple beads from the product screen were prepped following the same procedure after the preclear/anti-screen and screened again, using appropriately scaled amounts of reagents, against 25 μM of the full-length KRas protein. After developing additional beads were picked for a total of seven dark beads from the product/target screens of which five beads yielded readable sequences by Edman degradation sequencing.

5.9.10 Peptide preparation and purification

All cyclic peptides and epitopes were prepared following the procedures outlined in Reference 1. The peptides and epitopes were isolated using the following procedure. The resin was rinsed with DCM (5x) and dried under vacuum. A 20 mL scintillation vial was charged with a stir-bar, resin, and cleavage solution (95% TFA, 2.5% TESH, 2.5% H_2O) and allowed to stir at room temperature for 2-2.5 hours. The solution was then filtered into 40mL of cold diethyl ether, vortexed for 10 seconds, and stored at 4 °C overnight. The precipitated protein was centrifuged into a pellet at 4500 RPM for 10-15 minutes prior to decantation of the supernatant. The crude peptides were dissolved in either DMSO or (1:1) MeCN/H_2O w/0.1% TFA before HPLC purification, and lyophilization of desired fractions. The resulting lyophilized powder was dissolved in DMSO, quantified, and stored at 4 °C when not in use. For characterizing PCC ligands and epitopes, expected masses were calculated using the mass calculator at the following (Figure 5.10, 5.11, 5.12, 5.13, and 5.14): http://www.lfd.uci.edu/~gohlke/molmass/?q=C152H224N32O38S2Na.

5.9.11 Measurement of PCC ligand KRas EC$_{50}$ with the barcode rapid assay platform

Buffers used:

Wash buffer: PBS + 0.05% Tween20 (PBST)

Blocking Buffer: PBS + 1% BSA

Protein Incubation Buffer: Tris-buffered saline (TBS) + 0.05% Tween20 (TBST)

1° ab buffer: PBS + 5% BSA

2° ab buffer: PBS + 1% BSA

*Wash steps used 50 $^{\mu L}/_{well}$

*Incubation steps used 30 $^{\mu L}/_{well}$

The plate must be covered during incubation steps to protect the fluorescent blank

After loading the KRas protein change tips every time that solution is aspirated or added to a well to prevent cross-contamination

A pre-fabricated PDMS template was aligned onto the DNA barcode microchip, and the microchip was taped into a 10 cm petri dish. The wells on the platform were wet with PBST before filling with blocking buffer and placing into a 37 °C incubator for 1hr. Concurrently, 40 µL 1% BSA in PBS solutions containing 750 nM of a SAC-DNA and 3.75 µM of one biotinylated PCC ligand or biotin-A_{20}-Cy3 blank were prepared for each member of the DESL library. The biotinylated ligands were allowed to complex with the SAC protein for one hour before pooling the SAC-DNA-ligand solutions (final [SAC-DNA-ligand conjugates] = 50 nM). The blocking buffer was aspirated and each well was loaded with the SAC-DNA-ligand conjugates cocktail for hybridization with the DNA barcode at 37 °C for one hour. The wells were washed with PBST (3x) before loading serially diluted solutions of KRas protein in protein buffer (0 to 400 µM). After shaking at RT for one hour, the wells were rinsed with PBST (5x), making sure to pipet up/down with the first addition of PBST. A (100:1) dilution of CST rabbit anti-Ras Ab (#39655) in 1° ab buffer was added to each well before shaking at RT for one hour. After rinsing the wells with PBST (3x), the wells were loaded with a (200:1) dilution of Abcam goat anti-rabbit-

Alexafluor 647 linked ab (ab150079) in 2° ab buffer before shaking at RT for one hour. A final rinse of the wells with PBST (3x) proceeded peeling off the PDMS slab from the barcode microchip and dipping the barcode into the following solutions: PBS, (1:1) PBS: MQ H_2O, MQ H_2O (2x). After being spun dry, the barcode was read on the Genepix (635 nM, PMT 600, PWR 40%; 532 nM, PMT 450, PWR 15%). Data was extracted using 10 data blocks/barcode lane, double background corrected using the ab only well fluorescence and dummy ligand fluorescence in each well, and graphed in Graphpad (4-parameter mode with the Hill coefficient set=1) (Figure 5.3 and 5.18). The peeled off PDMS slab was rinsed under MQ H_2O and stored in MQ H_2O until further use.

5.9.12 Measurement of PCC ligand KRas EC$_{50}$ using the multi-well ELISA technology

Buffers used:

- Blocking Buffer: TBS + 5% milk + 0.05% Tween20

- Antibody (ab) Buffer: TBS, 5% BSA, 0.05% Tween20

- Binding Buffer: TBS, 0.1% BSA, 0.05% Tween20

*All steps were completed at room temperature

*All wash steps used 200 $^{\mu L\ solution}$/$_{well}$

*All incubations used 100 $^{\mu L\ solution}$/$_{well}$ except for the 5% milk blocking step, which used 200 $^{\mu L\ solution}$/$_{well}$

A 96-well Pierce Neutravidin Plate was washed with binding buffer (3 x 5 minutes @ RT) before loading plate with a 1μM solution of either blank (biotin-PEG$_5$-NHAc) or biotinylated PCC ligand. The plate incubated for two hours before washing with binding

buffer (3 x 5 minutes). Blocking buffer was added to each well and the plate blocked for one hour before undergoing washing with binding buffer (3 x 5 minutes). Each well was loaded with either binding buffer or KRas solution ($0 \rightarrow 300\mu M$), and the plate was incubated for 30 minutes. Plate washing with binding buffer (3 x 5 minutes) preceded incubating the plate with a (1000:1) dilution of $1°$ antibody (ab) rabbit anti-Ras (CST #3965) in ab buffer for thirty minutes. The plate was washed with binding buffer (3 x 5 minutes), loaded with a (2000:1) dilution of $2°$ ab goat anti-rabbit, HRP-linked ab (CST #7074) in ab buffer, and incubated for an additional thirty minutes. The plate was rinsed with binding buffer (3 x 5 minutes), TBS (1 x 5 minutes), loaded with a (1:1) mixture of TMB Peroxidase Solution and TMB Peroxidase Solution B, and developed with occasional agitation for 8-12 minutes. After quenching the enzymatic reaction with 1M $H_2SO_{4(aq)}$ (100μL) the plate was read within ten minutes. The data was double background corrected using the ab only absorbance and dummy ligand absorbance, plotted using Prism GraphPad 7 (4-parameter mode with the Hill coefficient set=1), and an EC_{50} value was calculated (Figure 5.19).